Jordan Journal of Mechanical and Industrial Engineering (JJMIE)

JJMIE is a high-quality scientific journal devoted to fields of Mechanical and Industrial Engineering. It is published by The Hashemite University in corporation with the Jordanian Scientific Research Support Fund.

Hashemite Kingdom of Jordan

Hashemite University

Jordan Journal of

Mechanical and Industrial Engineering

JJMIE

An International Peer-Reviewed Scientific Journal
Financed by Scientific Research Support Fund

Jordan Journal of Mechanical and Industrial Engineering (JJMIE)

JJMIE is a high-quality scientific journal devoted to fields of Mechanical and Industrial Engineering. It is published by The Jordanian Ministry of Higher Education and Scientific Research in corporation with the Hashemite University.

Introduction: The Editorial Board is very committed to build the Journal as one of the leading international journals in mechanical and industrial engineering sciences in the next few years. With the support of the Ministry of Higher Education and Scientific Research and Jordanian Universities, it is expected that a heavy resource to be channeled into the Journal to establish its international reputation. The Journal's reputation will be enhanced from arrangements with several organizers of international conferences in publishing selected best papers of the conference proceedings.

Aims and Scope: *Jordan Journal of Mechanical and Industrial Engineering* (JJMIE) is a refereed international journal to be of interest and use to all those concerned with research in various fields of, or closely related to, mechanical and industrial engineering disciplines. *Jordan Journal of Mechanical and Industrial Engineering* aims to provide a highly readable and valuable addition to the literature which will serve as an indispensable reference tool for years to come. The coverage of the journal includes all new theoretical and experimental findings in the fields of mechanical and industrial engineering or any closely related fields (Materials, Manufacturing, Management, Design, Thermal and Fluid, Energy, Control, Mechatronics, and Biomedical). The journal also encourages the submission of critical review articles covering advances in recent research of such fields as well as technical notes.

Guide for Authors

Manuscript Submission:

High-quality submissions to this new journal are welcome now and manuscripts may be either submitted online or email.

Online: For online and email submission upload one copy of the full paper including graphics and all figures at the online submission site, accessed via http://jjmie.hu.edu.jo. The manuscript must be written in MS Word 2010 Format. All correspondence, including notification of the Editor's decision and requests for revision, takes place by e-mail and via the Author's homepage, removing the need for a hard-copy paper trail.

Submission address and contact:
Prof. Nabil Anagreh
Editor-in-Chief
Jordan Journal of Mechanical & Industrial Engineering,
Hashemite University,
PO Box 330127, Zarqa, 13115, Jordan
E-mail: jjmie@hu.edu.jo

Types of contributions*: Original research papers and Technical reports

Corresponding author: Clearly indicate who is responsible for correspondence at all stages of refereeing and publication, including post-publication. Ensure that telephone and fax numbers (with country and area code) are provided in addition to the e-mail address and the complete postal address. Full postal addresses must be given for all co-authors.

Original material: Submission of an article implies that the work described has not been published previously (except in the form of an abstract or as part of a published lecture or academic thesis), that it is not under consideration for publication elsewhere, that its publication is approved by all authors and that, if accepted, it will not be published elsewhere in the same form, in English or in any other language, without the written consent of the Publisher. Authors found to be deliberately contravening the submission guidelines on originality and exclusivity shall not be considered for future publication in this journal.

Withdrawing: If the author chooses to withdraw his article after it has been assessed, he shall reimburse JJMIE with the cost of reviewing the paper.

Manuscript Preparation:

General: Editors reserve the right to adjust style to certain standards of uniformity. Original manuscripts are discarded after publication unless the Publisher is asked to return original material after use. Please use MS Word 2010 for the text of your manuscript.

Structure: Follow this order when typing manuscripts: Title, Authors, Authors title, Affiliations, Abstract, Keywords, Introduction, Main text, Conclusions, Acknowledgements, Appendix, References, Figure Captions, Figures and then Tables. Please supply figures imported into the text AND also separately as original graphics files. Collate acknowledgements in a separate section at the end of the article and do not include them on the title page, as a footnote to the title or otherwise.

Text Layout: Use 1.5 line spacing and wide (3 cm) margins. Ensure that each new paragraph is clearly indicated. Present tables and figure legends on separate pages at the end of the manuscript. If possible, consult a recent issue of the journal to become familiar with layout and conventions. All footnotes (except for table and corresponding author footnotes) should be identified with superscript Arabic numbers. To conserve space, authors are requested to mark the less important parts of the paper (such as records of experimental results) for printing in smaller type. For long papers (more than 4000 words) sections which could be deleted without destroying either the sense or the continuity of the paper should be indicated as a guide for the editor. Nomenclature should conform to that most frequently used in the scientific field concerned. Number all pages consecutively; use 12 or 10 pt font size and standard fonts.

Corresponding author: Clearly indicate who is responsible for correspondence at all stages of refereeing and publication, including post-publication. The corresponding author should be identified with an asterisk and footnote. Ensure that telephone and fax numbers (with country and area code) are provided in addition to the e-mail address and the complete postal address. Full postal addresses must be given for all co-authors. Please consult a recent journal paper for style if possible.

Abstract: A self-contained abstract outlining in a single paragraph the aims, scope and conclusions of the paper must be supplied.

Keywords: Immediately after the abstract, provide a maximum of six keywords (avoid, for example, 'and', 'of'). Be sparing with abbreviations: only abbreviations firmly established in the field may be eligible.

Symbols: All Greek letters and unusual symbols should be identified by name in the margin, the first time they are used.

Units: Follow internationally accepted rules and conventions: use the international system of units (SI). If other quantities are mentioned, give their equivalent in SI.

Maths: Number consecutively any equations that have to be displayed separately from the text (if referred to explicitly in the text).

References: All publications cited in the text should be presented in a list of references following the text of the manuscript.

Text: Indicate references by number(s) in square brackets in line with the text. The actual authors can be referred to, but the reference number(s) must always be given.

List: Number the references (numbers in square brackets) in the list in the order in which they appear in the text.

Examples:
Reference to a journal publication:
[1] M.S. Mohsen, B.A. Akash, "Evaluation of domestic solar water heating system in Jordan using analytic hierarchy process". Energy Conversion & Management, Vol. 38 (1997) No. 9, 1815-1822.

Reference to a book:
[2] Strunk Jr W, White EB. The elements of style. 3rd ed. New York: Macmillan; 1979.

Reference to a conference proceeding:
[3] B. Akash, S. Odeh, S. Nijmeh, "Modeling of solar-assisted double-tube evaporator heat pump system under local climate conditions". 5th Jordanian International Mechanical Engineering Conference, Amman, Jordan, 2004.

Reference to a chapter in an edited book:
[4] Mettam GR, Adams LB. How to prepare an electronic version of your article. In: Jones BS, Smith RZ, editors. Introduction to the electronic age, New York: E-Publishing Inc; 1999, p. 281-304

Free Online Color : If, together with your accepted article, you submit usable color and black/white figures then the journal will ensure that these figures will appear in color on the journal website electronic version.

Tables: Tables should be numbered consecutively and given suitable captions and each table should begin on a new page. No vertical rules should be used. Tables should not unnecessarily duplicate results presented elsewhere in the manuscript (for example, in graphs). Footnotes to tables should be typed below the table and should be referred to by superscript lowercase letters.

Notification: Authors will be notified of the acceptance of their paper by the editor. The Publisher will also send a notification of receipt of the paper in production.

Copyright: All authors must sign the Transfer of Copyright agreement before the article can be published. This transfer agreement enables Jordan Journal of Mechanical and Industrial Engineering to protect the copyrighted material for the authors, but does not relinquish the authors' proprietary rights. The copyright transfer covers the exclusive rights to reproduce and distribute the article, including reprints, photographic reproductions, microfilm or any other reproductions of similar nature and translations.

Proof Reading: One set of page proofs in MS Word 2010 format will be sent by e-mail to the corresponding author, to be checked for typesetting/editing. The corrections should be returned within **48 hours**. No changes in, or additions to, the accepted (and subsequently edited) manuscript will be allowed at this stage. Proofreading is solely the author's responsibility. Any queries should be answered in full. Please correct factual errors only, or errors introduced by typesetting. Please note that once your paper has been proofed we publish the identical paper online as in print.

Author Benefits:

No page charges: Publication in this journal is free of charge.

Free offprints: One journal issues of which the article appears will be supplied free of charge to the corresponding author and additional offprint for each co-author. Corresponding authors will be given the choice to buy extra offprints before printing of the article.

Evaluation of Loading Pattern Characteristics Influence on VVER 1000 Nuclear Reactor Pressure Vessel Neutron Fluence

Hasan Abou Faoor[a], Baida Achkar[a], Saed Dababneh[*b], Saadou Aldawahra[c]

[a] *Physics Department, Faculty of Science, Damascus University, Damascus, Syria*
[b] *Physics Department, Faculty of Science, Al-Balqa Applied University, Salt 19117, Jordan*
[c] *Department of Nuclear Engineering, AECS, Damascus, Syria*

Abstract

The present study deals with computational and analytical evaluation for the first approach of fuel loading, and presents the changes in neutron flux distribution of VVER-1000 reactor with each fuel loading type. The first approach proposed is based on dividing the core into axial cylindrical areas (equal number of batches), with each area having similar fuel (burn-up history). This paper includes a description of the core and fuel assembly lattice. The results allow us to determine the optimal first approach loading pattern, taking into account the maximum burn-up value, best power distribution and minimum vessel neutron fluence. The pressure vessel integrity analysis is carried out by comparing the vessel neutron fluence for each fuel loading scheme. Deterministic and probabilistic methods are employed in this study in order to achieve our goals.

1. Introduction

The life-time and integrity of a pressurized water reactor directly depends on the neutron irradiation of the reactor pressure vessel [1,2]. The pressure vessel is a fundamental component of light water reactors, since it contains the core and control mechanisms at high temperature and under high pressure. Therefore, pressure vessel integrity is important from the safety point of view, since increasing neutron fluence may significantly alter the behavior of vessel steel [3,4].

The embitterment of the material of the reactor vessel is primarily due to the fast neutron flux. The possible extension of the reactor life time needs neutron physical investigation of how new types of fuel elements, and new loading patterns, influence the neutron flux attaining the reactor vessel and detectors [5,6].

As indicated in the literature [7,8], core management plays an important role in the assessment of nuclear safety, as well as in the associated economics. In LWRs, the reactor is operated for normally one year long after the fuel is loaded into the core. After a period of operation, part of the fuel is replaced. Fuel loading and operation are repeated within a cycle. In-core fuel management implies designing fuel loading schemes over several cycles, such that the core produces the required energy output in an economical way, without violating safety constraints.

There are various strategies used to design the reload pattern. The out-in pattern is one wherein fresh fuel is loaded in the periphery of the core, then moved inward in subsequent cycles. The in-out pattern is the reverse. In the first few decades of PWR operation, the out-in patterns were employed [9]. More recently, the in-out procedure has replaced the out-in method to obtain low leakage cores and conserve ^{235}U. However, low leakage cores require the use of burnable poisons.

Economics and safety are the two primary concerns competing with each other in the in-core fuel management. In order to design all optimal fuel loading schemes, the constraints that the scheme must satisfy should be first identified.

In this study, pressure vessel integrity analysis is carried out for VVER-1000. This is achieved by studying the actual types of fuel loading strategies, and determining suitable schemes such as low leakage fuel-loading.

2. Fuel Management Objectives and Constraints

Most of the constraints are safety-related, except for the fundamental energy production requirements [7,8,9]. Therefore, reactivity and power distribution, in addition to the associated fuel enrichment and burnable absorbers, are described. The objective of fuel management is to design a fuel-loading scheme that is capable of producing the required energy at the minimum cost, while satisfying the safety constraints. More specifically, the objectives are:

---

[*] Corresponding author. e-mail: dababneh@bau.edu.jo.

(a) to meet the energy production requirements;

(b) to satisfy all safety-related design limits;

(c) to provide sufficient operating margins; and finally

(d) to minimize the power generation cost.

In order to produce the required energy, the reactor must sustain the rated power level for the specified cycle length, and should be able to be properly started and shutdown at any time in the cycle. The required energy generation becomes possible only when the loaded fuel has sufficient reactivity that covers reactivity defects associated with startup, as well as reactivity loss due to fuel depletion [10,11]. The startup defects consist of temperature, power, xenon and neutron leakage.

3. VVER-1000 Nuclear Reactor

VVER or WWER [12-16] is an abbreviation for "water water energy reactor." It is a pressure vessel type nuclear reactor with water used both as moderator and coolant, resulting in a thermal neutron spectrum. WWER-1000 designates a unit of 1000 MWe (electrical power) as output.

A VVER-1000 nuclear reactor core contains 163 fuel assemblies, arranged in hexagonal geometry (Figure 1). Each fuel assembly consists of 311 fuel pins, 18 guide tubes for placing burnable absorber cluster (BAR) or for movement of absorber rods of control and protection system (CPSAR), one guide tube for keeping in core instrumentation detectors (ICID), and a slotted central tube for structural support [10,13]. All these fuel pins/tubes are held by a framework of 15 hexahedral spacer grids, and a supporting tail grid (Figure 2). In order to reduce parasitic capture of neutrons in the core, several components, like the fuel clad, guiding tubes, BAR clad and spacing grids, are made of zirconium alloy. There are 54 locations in the core where Rhodium type SPND detectors shall be installed in ICID tubes [13]. In the first cycle, 42 BAR clusters are used for the purpose of flux flattening and for ensuring negative moderator coefficient of reactivity. In further cycles, 18 BAR clusters are used. The number of CPSAR used in first cycle is 85, which is increased to 103 in subsequent cycles [13]. The main physical characteristics of the reactor core are given in Table 1 [12-16].

The core, as well as the peripheral components, including reflector and water channels, were carefully and comprehensively modeled in this work (Figure 1). This is necessary in order to obtain realistic neutron flux calculated not only in the core, but also in that leaking to the vessel.
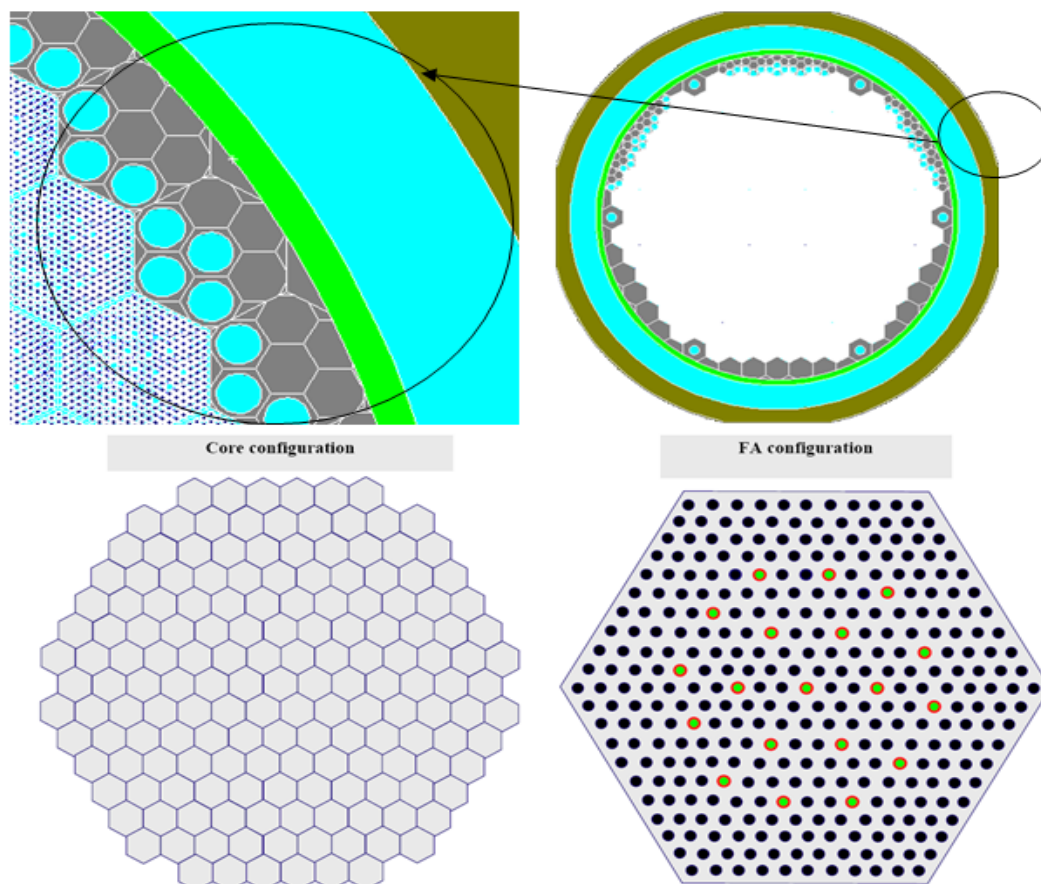

Figure 1. Upper panel: The reactor core and peripheral components were carefully modelled in this work (see text). Lower panel: Schematic view of the reactor core plan and fuel assembly [12]. Non-fuel element positions are identified.
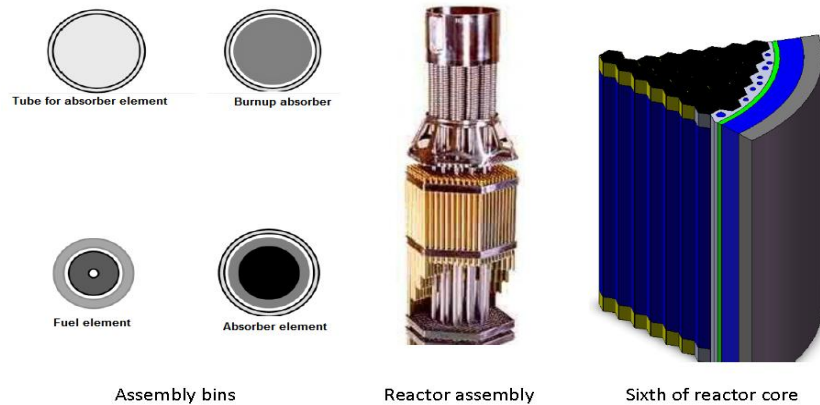
Figure 2. The design of FAs in the core (fuel and control rods).

Table 1. The main physical characteristics of the reactor core [12-16].

Characteristics	Value
Reactor nominal thermal power, MW	3000
Coolant pressure at the core outlet, MPa	15.7
Coolant temperature at the reactor outlet, C	321
Flow area of the core, m^2	4.14
Nominal duration of FA stay in the core, fuel cycle	3–4
Fuel height in the core in cold state, m	3.53
Equivalent diameter of the core, m	3.16
Pitch between FAs, m	0.236
Number of fuel assemblies inside the core	163
Mass of fuel in fuel assembly, kg	484.8
Nominal loading of reactor on UO_2, kg	79,840
Diameter of the vessel cylindrical part in the core, m	4.535

4. The Strategy for Development of VVER-1000 Fuel Cycle

The most important objective of this work is to choose a fuel loading scheme which provides:
1. A homogenized power production over the core which implies "flatness of power or low Peak Power Factor."
2. A low reactor vessel neutron fluence (basic requirement) [2,5].
3. The best value of fuel burn-up, which reflects good fuel utilization.
4. A low NPP generation cost indicated by:
   a) The ability to increase reactor cycle time. This helps to raise the value of plant Availability Factor, which is achieved by rising the initial reactivity of the core by raising fuel enrichment up to 5.2%.
   b) Increasing the number of batches, implying small batch size. This helps to achieve high burn-up fuel value and low plant fuel fabrication cost. The latter is implied by the smaller number of assembles (small batch size).

Very high average discharge burn-ups require high average ^{235}U enrichment in the initial core, and this, in turn, requires more ability of adjustment for the initial reactivity of the core by using additional amount of absorbers [11,17,18].

The Moderator Temperature Coefficient MTC requirement could be the most limiting constraint. It must be maintained negative in any Hot Full Power HFP condition in such longer cycle fuel management schemes. This is a consequence of high boron concentration required in long fuel cycles, and thus MTC becomes less negative with increasing boron. Therefore, in order to assure inherent safety, other types of Burnable Absorber BA, such as gadolinia, must be used to control the initial reactivity and the differential in reactivity between the fresh fuel and the partly burnt fuel in the core, leading to radial power peaking factors.

In order to achieve these goals by comparing various loading schemes, we developed a simulator for WWER 1000 reactor which performs the required calculations.

5. Choice of Burnable Absorber

The choice of burnable absorber bin characteristics has an important consideration for very high burn-ups [10,17,18]. Gadolinia was chosen for controlling radial power peaking. It is very important to carefully optimize the fuel and burnable poison loading patterns to minimize the initial enrichment. Therefore, the first simulation results obtained in this work are described in what follows.

Figure 3 depicts the result of studying the behavior of traditional fuel (e=4.4%) with different number of BA rods and different weight percent (w). As a result, we find that the following construction of the initial fuel is most suitable to start with:
1. The first (traditional) case (see Figure 3):
   a) The fuel bins: e =4.4%.
   b) The BA bins (Gd_2O_3):
      1. e =3.7%, w =4.0%.
      2. 18 fuel rod with BA.
   c) The Reactivity Equation which describes the average fuel burn up behavior in this case is:

$$\rho \approx \begin{cases} 0.165 & B \leq 12.5 \\ 0.2451 - 0.0054B & B > 12.5 \end{cases}$$
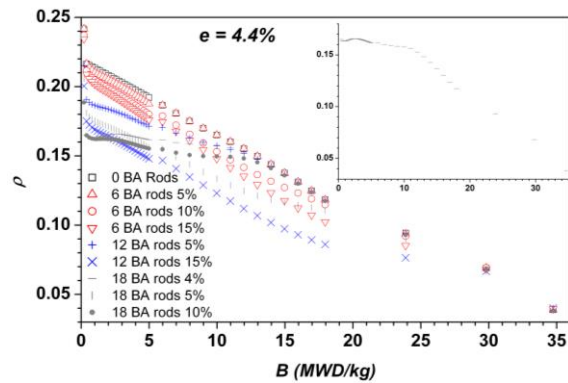
Figure 3. The behavior of variant traditional fuel constriction burn-up (e=4.4%). The inset illustrates the selected case for BA (see text).

While for fuel with enrichment e=5.2% suggested based on a study [17] presenting the relationship between the average discharge burn-up and the cycle length for different values of fresh fuel enrichment and different values of batch numbers, our study of fuel burn-up behavior with different number of BA rods and different weight percents implies the most suitable fuel construction as (see Figure 4):

2. The second (suggested) case:
   a)   For the fuel rods: e =5.2%.
   b)   For BA rods (Gd2O3)
      1.   e =3.7%, w =4.0%.
      2.   30 fuel rods with BA.
   c)   The Reactivity Equation which describes the average fuel burn up behavior in this case is:

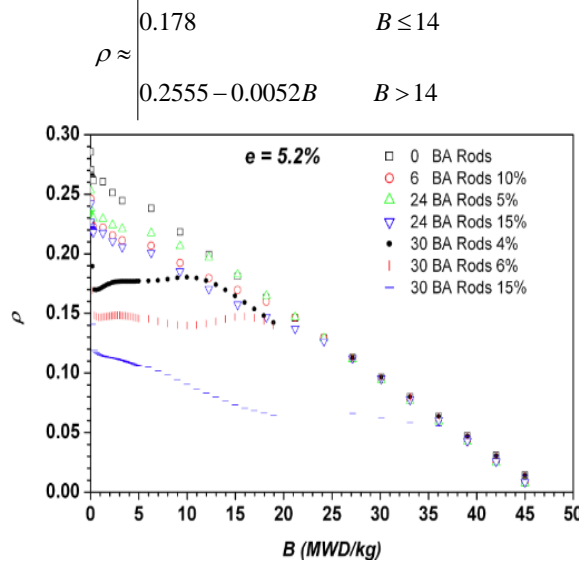$$\rho \approx \begin{cases} 0.178 & B \leq 14 \\ 0.2555 - 0.0052B & B > 14 \end{cases}$$

Figure 4: The behavior of variant fuel construction burn-up (e=5.2%).

It is worth noticing here that the load-up type symbol we adopt, like (1342), means the following: We divided the core into areas (Figure 5) of equal number of batches, and numbered areas from periphery toward center. The symbol is the numbers of areas from which fuel shaft on (fresh state until used state).

6. VVER -1000 Simulator and Simulation Results

In order to accomplish our objectives, the whole reactor core and peripheral component elements are modeled, in this work, using the MCNP4C2 and GETERA codes. Consequently, the neutronic parameters of the reactor core are calculated.

The simulator flowchart is depicted in Figure 6. The simulation procedures are based on:

1. The GETERA 90 code was used to perform the core burn-up calculations and the change in isotopic fuel components [19].
2. The Linear Reactivity model equations were programmed in this work in order to calculate burn-up characteristics for each FA according to its position in the reactor core [6,8,9].
3. The MCNP4C2 code was used to perform neutron flux and criticality calculation, in addition to peak power evaluation for each loading pattern [20,21].

As a conclusion from Section 5 above, the study considers two types of core fuel:

1. e = 4.4% + BA (Gd2O3, 18 rod, w = 4.0%);
2. e = 5.2% + BA (Gd2O3, 30 rod, w = 4.0%).

In order to validate our simulator, we compare the basic results for the traditional case (e=4.4) with referenced values before adopting results for the suggested case (e=5.2%). The comparative analysis presented in Table 2 provides confidence in our simulator and enables us to pursue the calculations.

For each loading scheme of the two cases, the simulator provides values of the peak power, burn-up, vessel neutron flux, K_{eff} and cycle time. The numerical values for these parameters are listed in Table 3 for the first case, and in Table 4 for the second.

The details as illustrated in the flowchart (Figure 6) are enormous, and in our assessment can't be contained in the text. Therefore, the detailed computational stages and analyses involved can be obtained directly from the authors.

Table 2. Comparative study for the traditional case (e = 4.4%).

Parameter	Simulator value		Referenced value		Relative Error (%)[a]
K_{eff} BOC	1.0529		1.05352	[14]	0.06
K_{eff} EOC	0.9828		0.969	[15]	1.42
Cycle Time [Month]	9.98		9.72	[22]	2.67
Peak Power	BOC=1.46 EOC=1.38	Ave=1.42	1.41	[16]	0.71
Peri. FA power decrease	0.26		0.25	[18]	4.00
NRV neutron flux decrease	0.37		0.31	[10,23]	19.4

[a] Calculated as

$$\left| \frac{Simulator\ value - Reference\ value}{Reference\ value} \right| \times 100$$
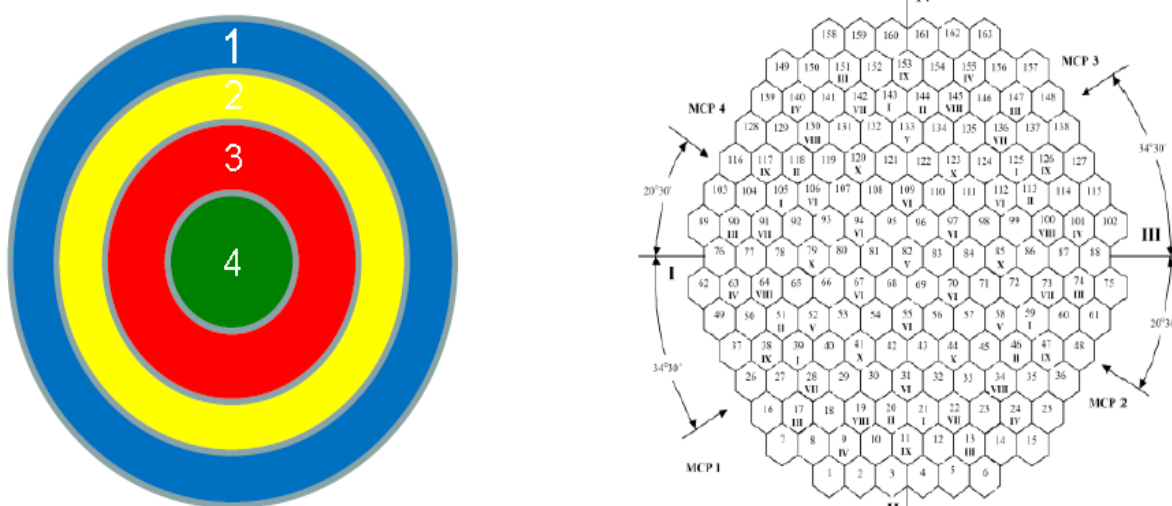
Figure 5. The first approach of reactor core loading pattern.

Table 3: Simulator results for the first case "e = 4.4% + 18 fuel rods with BA (Gd$_2$O$_3$)".

Pq fuel rod	Pq fuel AS	Vessel Neutron flux X 10^{11}	Burn-up Value				Cycle Time		K$_{eff}$		Load-up type →			NO. of batches
			1	2	3	4	day	month	K$_{eff}$	D K$_{eff}$				
1.82	1.18	1.9052	11.43	22.81	33.64	44.39	277.45	9.25	1.02	0.00			1234	
1.29	1.25	1.2530	11.49	22.93	34.83	44.67	279.194	9.31	1.01168	3E-04			1243	
1.67	1.28	1.5802	11.48	23.53	33.81	44.57	278.573	9.29	1.01902	2E-04			1324	
1.30	1.29	0.75523	11.57	23.71	35.59	45.03	281.424	9.38	1.02246	2E-04	BOC	OUT-IN	1342	
1.29		1.0926							0.96679	2E-04	EOC			
2.12	1.48	0.22402	11.60	25.02	35.29	45.22	282.648	9.42	1.02656	2E-04			1423	4
1.78	1.47	0.29544	11.63	25.07	35.90	45.36	283.499	9.45	1.04035	2E-04			1432	
1.48	1.46	0.61477	12.33	25.86	36.74	45.91	286.943	9.56	1.04497	2E-04			2431	
1.42	1.28	0.55916	12.27	24.49	36.43	45.59	284.94	9.60	1.04149	2E-04	BOC	LLLP	2341	
1.38		0.79066							0.9828	2E-04	EOC			
1.96	1.57	0.095717	14.69	27.08	37.64	47.02	293.88	9.80	1.08265	2E-04			4321	

Fuel Enrichment x%
Unit Cell Geometry
BP
Reactor environment

Load up
Type

GETERA
Code

$K_\infty = f(B)$

Excel

$\rho(B) = a_0 + a_1 B + a_2 B^2 + \ldots\ldots + a_n B^n$

Assembly Placement in Core
Number of Batches

Burnable Poisons Case

Soluble Poisons Only

Constant RHO
Slop RHO

Reactor Operating Calc
$B_{BOC,i}$, $B_{BOL,1} = 1$

ρ_i , F_i

$i = 1,..n$

ρ_{sys}

$B_{BOC}^i + step$

NO

ADD Boron

NO

if $\rho_{sys} = 0$

YES

$|B^{i+1} - B^i|$

$< \xi$

YES

$B(i), F(i)$
$FPAVGS$

Excel

Peck power , B final
Vessel Neutron flounce
Cycle Time

END

Figure 6. VVER-1000 simulator flow chart.

Table 4: The simulator results for the second case "e = 5.2% + 30 fuel rods with BA (Gd$_2$O$_3$)".

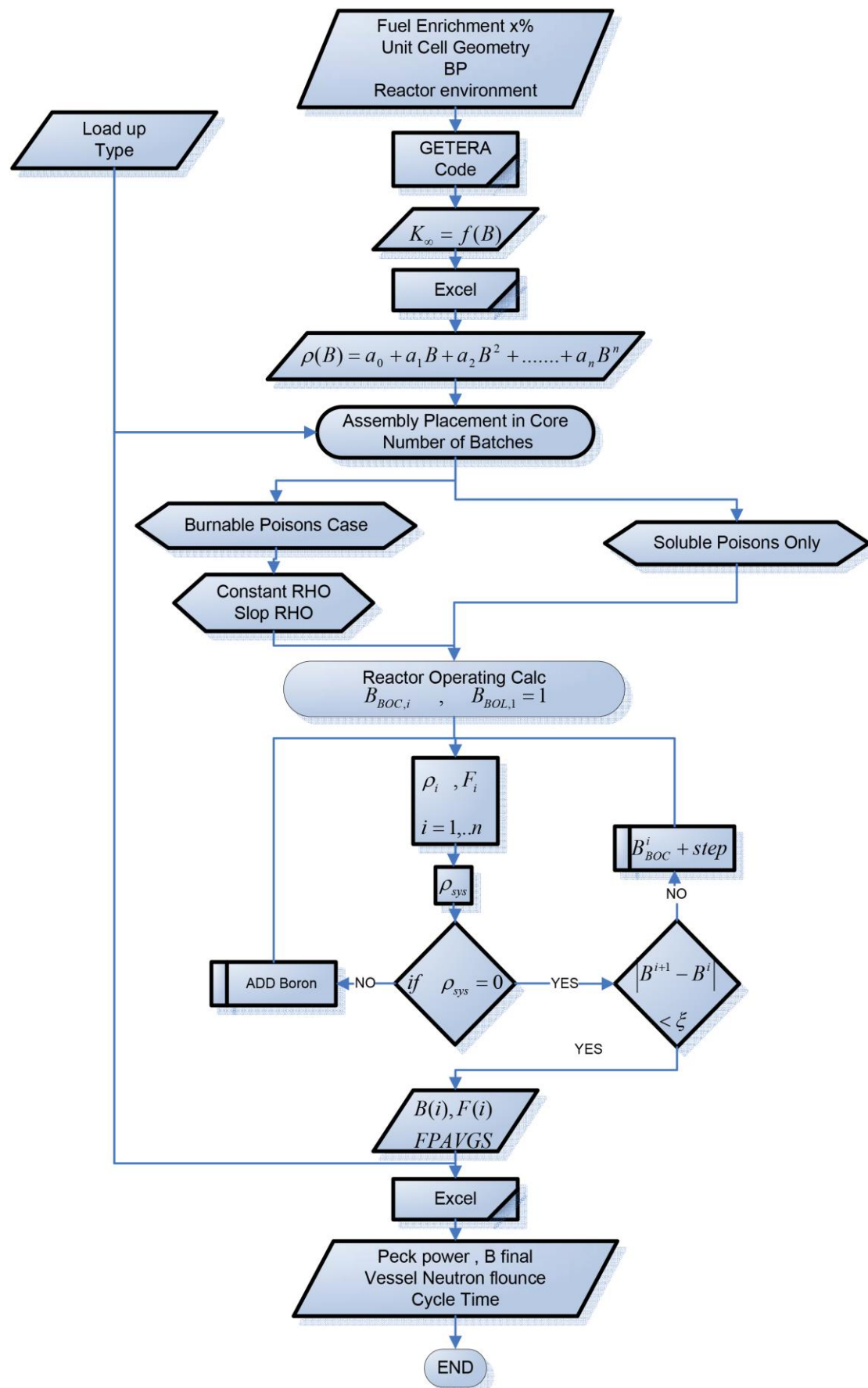| Pq fuel rod	Pq fuel AS	Vessel Neutron flux X 10^{11}	Burn-up Value					Cycle Time		K$_{eff}$		Load-up type →		NO. of batches
			1	2	3	4	5	day	month	K$_{eff}$	D K$_{eff}$			
2.19	1.31	1.3441	13.88	27.38	39.75	51.58	63.06	373.71	12.46	1.02194	3E-04		12345	
1.95	1.31	1.7799	13.90	27.41	40.37	51.69	63.18	374.42	12.48	1.01479	2E-04		12435	
1.43	1.31	1.4336	13.93	27.49	40.49	52.97	63.41	375.75	12.52	1.0057	2E-04		12453	
1.88	1.31	1.0755	13.95	27.51	41.31	52.62	63.52	376.43	12.55	1.01767	2E-04		12534	
1.94	1.31	0.39094	13.97	27.54	41.36	53.14	63.61	376.92	12.56	1.02089	3E-04		12543	
2.62	1.33	1.2598	13.98	27.39	39.68	52.29	63.24	374.73	12.49	1.07186	3E-04		13254	
1.63	1.33	1.1751	13.99	27.85	40.87	53.36	63.69	377.40	12.58	1.01582	2E-04		13452	
1.45	1.32	0.68538	13.98	27.84	41.65	52.78	63.72	377.60	12.59	1.04211	2E-04	LLLP	13524	
1.36	1.39	1.2522	13.99	28.51	40.68	53.18	63.66	377.24	12.57	1.00683	3E-04	OUT-IN	14253	5
1.54	1.40	0.90246	14.00	28.55	40.95	53.46	63.81	378.14	12.60	1.01814	2E-04		14352	
1.72	1.39	0.47518	14.03	28.61	42.39	53.52	64.03	379.45	12.65	1.03427	3E-04		14523	
2.12	1.50	0.42833	14.05	29.61	41.76	53.56	64.06	379.63	12.65	1.04402	2E-04		15243	
2.13	1.51	0.28722	14.05	29.59	41.94	53.12	64.09	379.77	12.66	1.04019	2E-04		15324	
1.97	1.50	0.18540	14.08	29.66	42.57	53.72	64.24	380.67	12.69	1.05111	2E-04		15423	
2.75	1.39	3.4074	14.54	29.17	42.99	54.32	64.53	382.38	12.75	1.08228	3E-04		24531	
3.43	1.50	3.5376	14.57	30.18	42.58	54.42	64.63	382.99	12.77	1.10407	3E-04		25341	
3.21	1.50	3.5743	14.59	30.22	43.18	54.52	64.74	383.63	12.79	1.09816	3E-04		25431	
2.75	1.61	2.8616	16.91	31.61	44.19	55.55	65.93	390.67	13.02	1.18591	3E-04		54321	

7. The Load-Up Schemes

First case e=4.4 %

By comparing the different fuel load-up schemes in terms of the radial power peaking factor Pq and reactor vessel RV neutron flux, we distinguish the "1342" OUT-IN fuel loading type, and the "2341" Low Leakage Loading Pattern LLLP scheme, as illustrated in Figure 7. This choice satisfies the lowest reactor vessel neutron fluence for the LLLP while keeping acceptable increase of Pq value.

The numerical characteristics of the "1342" OUT-IN and the "2341" LLLP schemes are listed in Table 5. We presumed a decrease of the NRV fluence by about 30% using LLLP instead of OUT-IN scheme, which could comprise a positive consequence on NRV life time. The simulator results provided a good uniformity with referenced values as shown in Table 5. This positive outcome furnishes the ground for exploring new cases using the simulator.

The thermal, the up thermal and the fast neutron flux distributions for the LLLP scheme extracted via the simulator over the reactor components are illustrated in Figure 8.
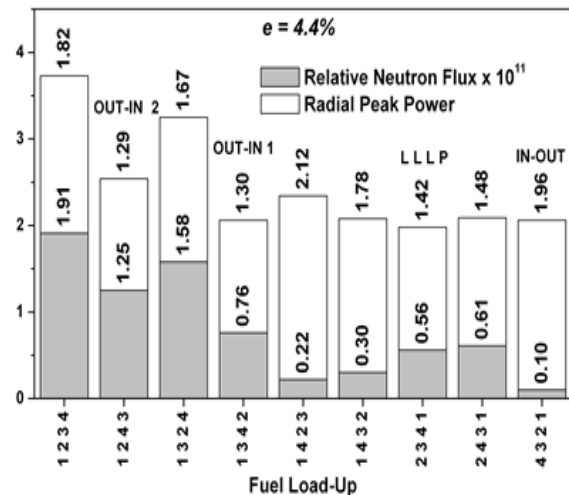

Figure 7. Comparison of different fuel load-up schemes according to Pq and RV neutron flux (e=4.4 %).

Figure 8 depicts the thermal, up thermal and fast neutron flux distributions over the core for LLLP "2341".

Table 5. The "1342" OUT-IN scheme & the "2341" LLLP scheme characteristics for the first case (e=4.4 %).

| NRV neutron flux decrease	FA power decrease	Fluence decrease	Fluence	Peak Power	Cycle Time MONTH	K_{eff}	Load-up Type →		
0.37	0.26	0.31	3.6E+18	1.24	9.80	1.04948	BOC	OUT-IN	1342
				1.29		0.96679	EOC		
			2.4E+18	1.46	9.98	1.0529	BOC	LLLP	2341
				1.38		0.9828	EOC		
0.31	0.25	0.3	7.27E+19	1.41	9.72	1.05352 [14]	Referenced value		
[10] [23]	[1]	[10] [23]	[24]	[16]	[22]	0.969 [15]			
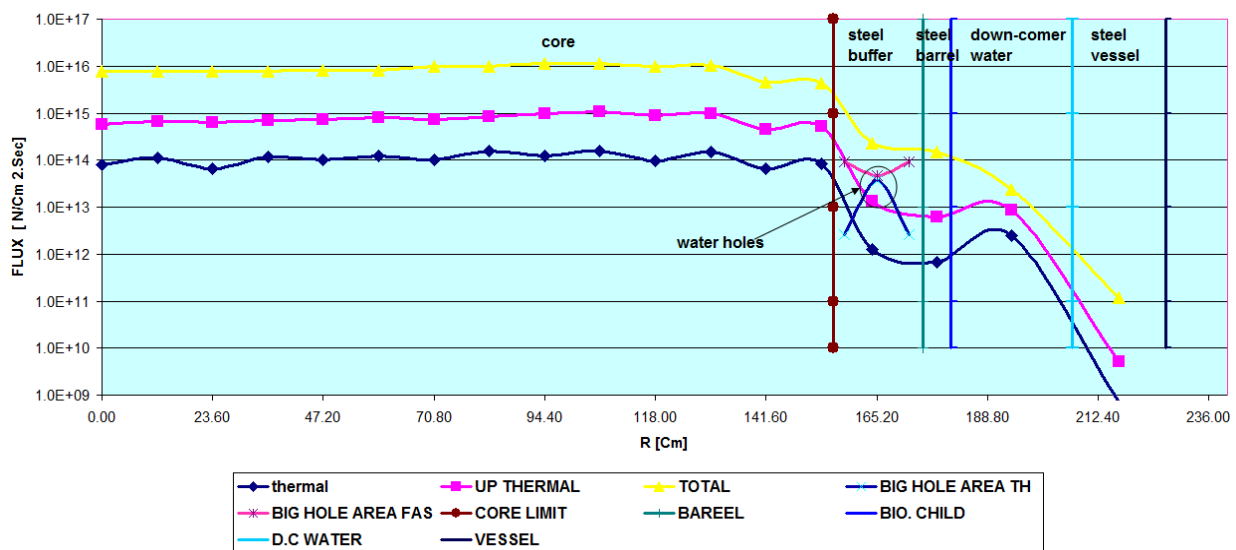
Figure 8. The thermal, up thermal and fast neutron flux distributions over the core for e=4.4% and LLLP "2341".

Second case e=5.2%

Following the same argument for the proposed case (e=5.2%), we distinguish the "13524" LLLP scheme, with the best (0.69×10^{11} n/cm^2.s) flux and a corresponding Pq value of 1.45 (Figure 9).

Figure 10 depicts the thermal, up thermal and fast neutron flux distributions over the reactor for the selected scheme; namely LLLP "13524".

Finally, it is worth mentioning that Tallies F4, *F4, F7 and *F7 were used to calculate neutron flux densities in different core cells and power in fuel cells. The obtained power distributions were used to obtain radial peak power (Pq). The RV neutron flux was obtained using F2 tally for internal reactor vessel surface for fast neutrons (> 0.5 MeV). The results were used to get a sectional distribution of neutron flux through the core and the surrounding components as shown in Figures 8 and 10.
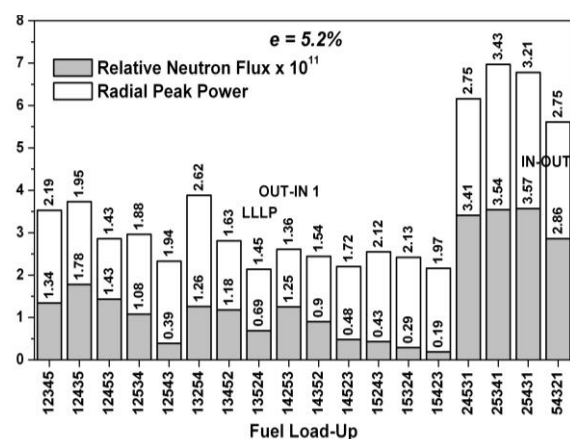
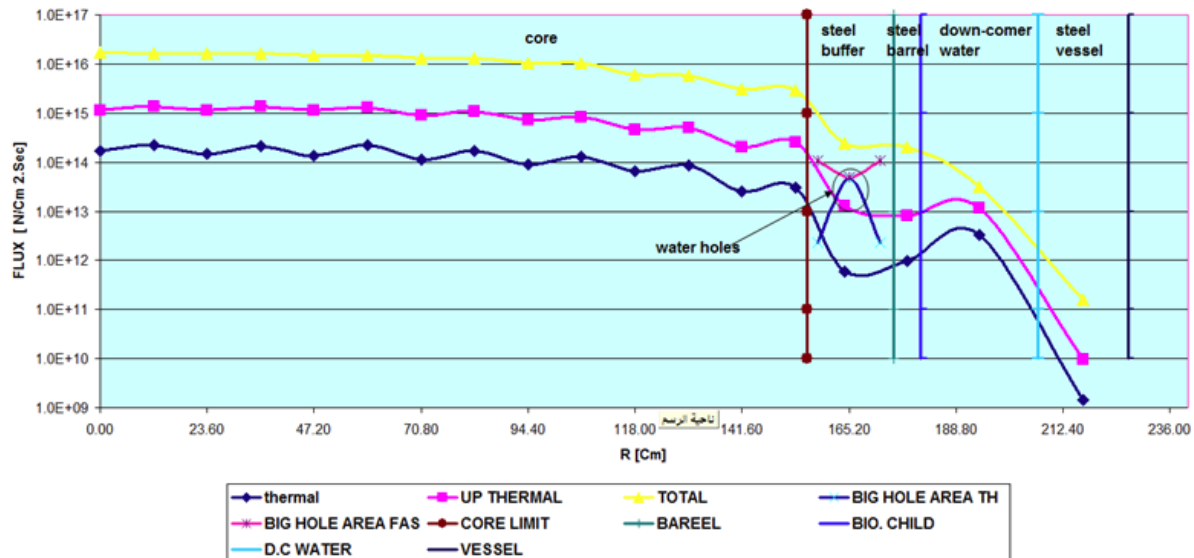**Figure 9**: Comparison of different fuel load-up schemes according to Pq and RV neutron flux (e=5.2 %).

Figure10: The thermal, up thermal and fast neutron flux distributions over the core for e=5.2% and LLLP "13524".

8. Conclusion

In this study, a method for the first approach of optimizing the VVER-1000 nuclear reactor loading pattern was introduced. Using this method, we evaluated the pressure vessel integrity by comparing the vessel neutron fluence for each fuel loading scheme. A simulator was developed to calculate the basic characteristics (peak power, vessel fluence and average burn-up value). The most significant results were:

• For the first standard case e =4.4%:

The use of LLLP scheme instead of OUT-IN load pattern permitted to reduce the reactor vessel neutron fluence by 31%, and the reactor vessel neutron flux by 26%. On the other hand, the LLLP scheme increased the batch time by 2.3% comparing to the OUT-IN load pattern. One inconvenience of the LLLP scheme involved the increase of Pq by about 9.23% (from 1.3 to 1.42) compared to literature values of Pq=1.41 and Pq critical=1.55 [4,8,14].

• For the second proposed case e =5.2%:

The LLLP (5 batches + e=5.2%) allowed to lower the reactor vessel neutron flux by 9.3%, to increase the batch time by 19.3%, and to raise the average burn-up value by 41.5% (up to 63.73). In addition, the reactor spent fuel production rate is reduced from 41 assemblies by 9.4 months, to 33 assemblies by 11.2 months.

Furthermore, the Pq value for the selected LLLP scheme increased by about 11.5% (from 1.3 to 1.45) which is still beneath the critical value of 1.55.

References

[1] B. Boehmer, J. Konheiser, K. Noack, A. Rogov, G. Borodkin, E. Polke, P. Vladimirov, "Neutron and gamma fluence and radiation damage parameters of ex-core components of Russian and German light water reactors". Proceedings of the 11th International Symposium on Reactor Dosimetry, 18-23 August 2002 in Brussels, Belgium. World Scientific Publishing Co. ISBN #9789812705563; 2003, 286-294.

[2] O.Ö. Gülol, Ü. Çolak, "Comparison of pressure vessel integrity analyses and approaches for VVER 1000 and PWR vessels for PTS conditions". Nuclear Engineering and Design, Vol. 226 (2003) 231–241.

[3] A. Kryukov, D. Erak, L. Debarberis, F. Sevini, B. Acosta, "Extended analysis of VVER-1000 surveillance data". International Journal of Pressure Vessels and Piping, Vol. 79 (2002) 661–664.

[4] J.J. Duderstadt, L.J. Hamilton. Nuclear Reactor Analysis. 1st edition. Wiley; 1976.

[5] G.L. Guthrie, "Preliminary study of the use of fuel management techniques for slowing pressure vessel embrittlement". 4th International ASTM-EURATOM Symposium on Reactor Dosimetry, Gaithersburg, MD, USA, 22 Mar 1982, 111–120.

[6] C.W. Bagnal, G.P. Cavanaugh, L.B. Tarko. Survey of vessel fluence reduction techniques. Palo Alto, California, Electric Power Research Institute EPRI; 1984.

[7] A.H. Fadaei, N.M. Moghaddam, E. Zahedinejad, M.M. Fadaei, S. Kia, "Fuel management optimization based on power profile by Cellular Automata". Annals of Nuclear Energy, Vol. 37 (2010) 1712–1722.

[8] Sh. Jiang. Nuclear fuel management optimization using estimation of distribution algorithms. Ph.D. Thesis, Imperial College, University of London, UK; 2009.

[9] E. de Klerk, C. Roos, T. Terlaky, T. Illés, A.J. de Jong, J. Valkó, J.E. Hoogenboom, "Optimization of nuclear reactor reloading patterns". Annals of Operations Research, Vol. 69 (1997) 65–84.

[10] B.D. Murphy, J. Kravchenko, A. Lazarenko, A. Pavlovitchev, V. Sidorenko, A. Chetverikov. Simulation of Low-Enriched Uranium (LEU) Burnup in Russian VVER reactors with the HELIOS code package. Oak Ridge National Laboratory, Oak Ridge, Tennessee. Report ORNL/TM-1999/168; 2000.

[11] I. Panayotov, N. Mihaylov, K. Ilieva, D. Kirilova, M. Manolova, "Burnup influence on the VVER 1000 reactor vessel neutron fluence evaluation". 19th Symposium on AER for VVER Reactor Physics and Reactor Safety, St. Constantine, International House of Scientists, Bulgaria, 2009.

[12] IAEA. WWER-1000 Reactor Simulator. Training Course Series No. 21, Second Edition, IAEA Vienna, ISSN 1018–5518; 2003.

[13] S. Kaichao. MCNP modeling of hexagon VVER fuel. M.Sc. Thesis, Department of Reactor Physics, Royal Institute of Technology, Stockholm, Sweden; 2008.

[14] G. Todorova, N. Petrov, N.P. Kolev, P. Bellier, "2D Core calculations for VVER 1000 with APOLLO2". International Conference on the Physics of Reactors, Nuclear Power: A Sustainable Resource, Interlaken, Switzerland, September 14-19, 2008.

[15] G. Todorova, N. Petrov, N.P. Kolev, F-X. Hugot, "2D Core Solutions for VVER 1000 with APOLLO2 and TRIPOLI4". 19th Symposium on AER for VVER Reactor Physics and Reactor Safety, St. Constantine, International House of Scientists, Bulgaria, 2009.

[16] J. Lee, N.Z. Cho, "AFEN method and its solutions of hexagonal three-dimensional VVER-1000 benchmark problem". Progress in Nuclear Energy, Vol. 48 (2006) 880-890.

[17] Nuclear Energy Agency. Very high burn-ups in light water reactors. NEA No. 6224, ISBN 92-64-02303-8, Paris, France; 2006. <http://www.oecd-nea.org/science/pubs/2006/nea6224-burn-up.pdf>

[18] P.N. Alekseev, A.V. D'yakov, A.S. Kolokol, A.A. Proshkin, A.L. Shimkevich, "Improvement of the operating characteristics of VVER oxide fuel". Atomic Energy, Vol. 102 (2007) No. 2, 129-134.

[19] N. Belousov, S. Bychkov, Yu. Marchuk *et al.*, "The Code GETERA for cell and polycell calculations: Models and Capabilities". Proceedings of the 1992 Topical Meeting on Advances in Reactor Physics, Charleston, SC, USA, 8–11 March, 1992, Vol. 2 (1992) 516–523.

[20] J.F. Briesmeister (Ed.). MCNP – A general Monte Carlo N-Particle transport code (Version 4C2). RSICC# CCC-700, Oak Ridge National Laboratory; 2000.

[21] J.S. Hendricks. MCNP-4C manual. University of California, Los Alamos National Laboratory, U.S. Department of Energy; 2000.

[22] P.V. Petkov, D.V. Hristov, "VVER-1000/V320 decay heat analysis involving TVS-M and TVSA fuel assemblies". Nuclear Engineering and Design, Vol. 238 (2008) 3227-3239.

[23] D. Fraklin, T. Marston. Investigation the flux reduction option in reactor pressure vessel integrity. Palo Alto, California, Electric Power Research Institute EPRI; 1983.

[24] J. Böhmert , H-W. Viehrig, H. Richter. Irradiation response of VVER pressure vessel steels: First results of the Rheinsberg irradiation programme. Wissenschaftlich-Technische Berichte, Forschungszentrum Rossendorf, FZR-284 (2000) 71-76.

A New Model for Predicting Crack Initiation Life in Thin Walled Tubes under Multiaxial Proportional Loading

Liu Jianhui[a], Wang Shengnan[*a], Wei Yong[b], Chen Jiazhao[b], QU Xiaowu[c]

[a] School of aeronautics, Northwestern Polytechnical University, xi'an, 710072, china

[b] Luoyang Lyc Bearing CO..LTD, luoyang, 471000, china

[c] Unit 68306 of PLA, lintong, 710608, china

Abstract

The theory of fracture mechanics is unable to estimate crack initiation life, but the theory of damage mechanics can do it well. The application of critical plane method in multiaxial fatigue has made certain progress. According to the law of thermodynamics, a new damage model is proposed in this paper to predict the crack initiation life under multiaxial proportional loading condition based on damage mechanics and critical plane method. The maximum shear strain amplitude and the normal strain on the maximum shear strain plane are the components of this model. Finally, the crack initiation life is predicted with the proposed model, which is damage mechanics-critical plane method. The predicted results of using the new model comply with the experimental results.

1. Introduction

The mechanical structures in practical application mostly work under cyclic loading. The loading mode may be uniaxial cyclic loading, or likely to be multiaxial cyclic loading. One of the main forms of failure is the fatigue fracture. The loading procedure will continuously produce damage, which often results in micro crack formation and propagation of damage accompanied by a large amount of plastic deformation. The mathematical description of the damage variable is introduced in damage mechanics, and it is applied to structural analysis. The fatigue life predicted model is put forward with the help of the concept of effective stress [1-3]. The critical plane method considers the physical meaning of fatigue fracture, which is widely used currently in the predicted of multiaxial fatigue life. Brown and Miller [4-7] believed that the maximum shear strain helps crack nucleation and normal strain helps crack extension. So a new multiaxial nonlinear damage model based on damage mechanics and critical plane method is proposed in this article. The essence of this model is to replace the control parameters of the uniaxial nonlinear damage model with the largest equivalent strain [8-9]. It was proved that the multiaxial nonlinear damage model is available and practicable by the comparative analysis of the predicted results with the experimental data.

2. Damage Variable and Effective Stress

The premise of analysis of materials and components mechanical property by damage theory is to choose the proper damage variables to describe the damage state [10-11]. The concept of continuum damage mechanics is proposed by Kachanov when he studied metal creep problems, he considered that the main mechanism of material degradation is caused by the decrease of effective bearing area [12-13], then the concept of continuous degree is proposed to describe the damage of materials and it can be defined as follows: a representative hexahedron element is selected and the total sectional area, which is perpendicular to the direction of n, is assumed A (Figure 1).
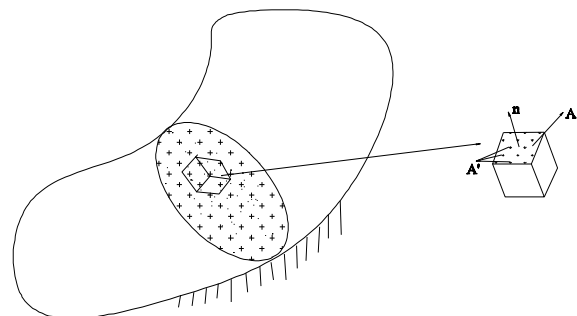

Figure 1. Damaged element

* Corresponding author. e-mail:liujianhui2010@163.com.

The continuous degree is defined as:

$$\varphi = \frac{A'}{A} \tag{1}$$

where A' is the actual effective section area and A is the cross section area which doesn't have damage.

The damage degree D, the supplement parameter of continuous degrees, is introduced to describe the damage by Rabotnov [14].

$$D = 1 - \varphi \tag{2}$$

Combining Eq. (1) with Eq. (2), the following equation can be given as:

$$A' = (1 - D) A \tag{3}$$

The effective stress can be defined as the ratio of the load F to the effective bearing area:

$$\sigma' = \frac{F}{A'} = \frac{F}{(1-D)A} \tag{4}$$

Eq. (4) is a classical expression of damage variable, which has been widely accepted. The principle of equivalent strain can be described as: the strain in the case of the effective stress equal to that in the case of no damage. According to this principle, the constitutive relation of damaged material can be obtained by replacing the nominal stress with the effective stress of damaged material. In the case of one dimensional elastic [15-16]:

$$\sigma = (1 - D) E \varepsilon \tag{5}$$

It is widely accepted that fatigue crack initiation involves a localized plastic deformation in persistent slip bands in the low cycle fatigue region. It has been experimentally observed that the direction of these persistent slip bands is very closely aligned with that of the maximum shear strain direction and fatigue cracks have always been found to initiate on the maximum shear strain planes under different loading situations. This justifies the belief that the fatigue initiation process is predominantly controlled by the maximum shear strain. Comparing the torsion data with the uniaxial data based on the maximum shear strain, most investigators have found the torsion data to lie above the uniaxial data as was also the case in this investigation [17-19]. This suggests that a second parameter is involved in the fatigue damage process. As mentioned previously, Brown and Miller take this parameter to be the normal strain on the maximum shear plane. They argue that his normal strain influences fatigue ductility which in turn is related to the fatigue strength and then conclude that the normal strain across the maximum shear strain plane assists in crack propagation. One advantage of these theories is their physical interpretation of the fatigue damage accumulation. The equivalent strain amplitudes can be obtained based on von Mises rule.

3. Uniaxial Fatigue Damage Model

In the fatigue damage theory, the damage is often expressed as a function of load cycles. Under normal circumstances, the fatigue damage evolution equation can be represented as the following form:

$$dD = f(...) dN \tag{6}$$

The variables of function $f(...)$ can be stress, strain and damage variable. At the same time, in order to describe the nonlinear damage accumulation and the loading sequence effect, loading parameters and damage variable are inseparability. The damage evolution of materials or components is a kind of irreversible thermodynamics process. Lemaitre *et al*, describe the fatigue damage evolution equation as the following equation [6]:

$$dD = (1-D)^{-p} \left[\frac{\sigma_{max} - \sigma_m}{M(\sigma_m)(1-D)} \right]^{\beta} dN \tag{7}$$

where σ_{max} is the largest stress amplitude, σ_m is the average stress, p and β are the parameters associated with the loading form and material constant.

When $D = 0$, $N = 0$; and when $D = 1$, $N = N_f$. The following equations can be obtained by definite integration of Eq. (7):

$$\int_0^1 (1-D)^{p+\beta} dD = \left[\frac{\sigma_{max} - \sigma_m}{M(\sigma_m)} \right]^{\beta} \int_0^{N_f} dN \tag{8}$$

$$N_f = \frac{1}{1+p+\beta} \left[\frac{\sigma_{max} - \sigma_m}{M(\sigma_m)} \right]^{-\beta} \tag{9}$$

$$D = 1 - \left(1 - \frac{N_R}{N_f} \right)^{\frac{1}{1+p+\beta}} \tag{10}$$

Where, p, β and M are constant, which are concerned with material and the way of loading, $\sigma_{max} - \sigma_m = \frac{\Delta\sigma}{2}$, $M(\sigma_m) = M_0 (1 - b\sigma_m)$, N_R is actual life.

This paper mainly studies the fatigue damage problem under a symmetric constant amplitude loading, so Eq.(9) can be represented as:

$$N_f = \frac{M_0}{1+p+\beta} \left(\frac{\Delta\sigma}{2} \right)^{-\beta} \tag{11}$$

It can be seen that the main parameter for uniaxial fatigue model is $\frac{\Delta\sigma}{2}$, which can be obtained from the existing test and theory analysis. The fatigue property of material under proportional loading is consistent with that under uniaxial fatigue condition, thus $\frac{\Delta\sigma}{2}$ can be replaced by the equivalent stress amplitude under the condition of proportional multiaxial loading, namely the multiaxial nonlinear fatigue cumulative damage model can be got by the above method.

According to the strain hardening laws:

$$\frac{\Delta\sigma}{2} = K (\Delta\varepsilon_p / 2)^n \tag{12}$$

where K and n are the material constants.
So Eq. (11) can be rewritten as:

$$N_f = \frac{M_0^{\beta}}{1+p+\beta} \left(K (\Delta\varepsilon_p / 2)^n \right)^{-\beta} \tag{13}$$

4. Multiaxial Fatigue Damage Model

A thin wall pipe is generally selected in the multiaxial fatigue test. The most serious damage plane is vertical to the free surface [20-23], which is the plane we care about. The stress and strain state under pull-torsion loading can be expressed as:

$$\sigma = \begin{bmatrix} \sigma_{xx} & \sigma_{xy} & 0 \\ \sigma_{xy} & 0 & 0 \\ 0 & 0 & 0 \end{bmatrix}, \; \varepsilon = \begin{bmatrix} \varepsilon_{xx} & \varepsilon_{xy} & 0 \\ \varepsilon_{xy} & \varepsilon_{yy} & 0 \\ 0 & 0 & \varepsilon_{zz} \end{bmatrix} \quad (14)$$

In this paper, the loading form can be expressed as:

$$\varepsilon_{xx} = \varepsilon_a \sin \omega t \quad (15)$$

$$\gamma_{xy} = \lambda \varepsilon_a \sin(\omega t - \varphi) \quad (16)$$

Where λ is the ratio of shear strain to axial strain, φ is phase difference.

The strain state of the plane which is canted by θ to the axis of the specimens can be expressed as:

$$\varepsilon_\theta = \frac{\varepsilon_x + \varepsilon_y}{2} + \frac{\varepsilon_x - \varepsilon_y}{2} \cos 2\theta + \frac{1}{2} \gamma_{xy} \sin 2\theta \quad (17)$$

$$\frac{\gamma_{xy}}{2} = \frac{\varepsilon_x - \varepsilon_y}{2} \sin 2\theta - \frac{1}{2} \gamma_{xy} \cos 2\theta \quad (18)$$

where $\varepsilon_y = -\nu \varepsilon_x$.

So Eq.(17) and Eq.(18) can be represented as:

$$\varepsilon_\theta = \frac{1-\nu}{2} \varepsilon_x + \frac{1+\nu}{2} \varepsilon_x \cos 2\theta + \frac{1}{2} \gamma_{xy} \sin 2\theta \quad (19)$$

$$\frac{\gamma_{xy}}{2} = \frac{1+\nu}{2} \varepsilon_x \sin 2\theta - \frac{1}{2} \gamma_{xy} \cos 2\theta \quad (20)$$

At the time, when $\varphi = 0$

$$\varepsilon_\theta = \frac{1-\nu}{2} \varepsilon_a \sin \omega t + \frac{1+\nu}{2} \varepsilon_a \sin \omega t \cos 2\theta$$
$$+ \frac{1}{2} \lambda \varepsilon_a \sin \omega t \, \mathrm{s} \quad (21)$$

$$\frac{\gamma_{xy}}{2} = \frac{1+\nu}{2} \varepsilon_a \sin \omega t \sin 2\theta - \frac{1}{2} \lambda \varepsilon_a \sin \omega t \cos 2\theta \quad (22)$$

Because the critical plane is defined as the plane of the maximum shear strain, thus,

$$\frac{\partial \gamma_{xy}}{\partial \theta} = 0 \quad (23)$$

Though Eq.(23), the θ range can be obtained:

$$\theta = \frac{1}{2} \tan^{-1} \frac{-(1+\nu)}{\lambda} \quad (24)$$

In the range between $-\pi/2$ and $\pi/2$, there are two θ ($\theta_{max}, \theta_{min}$) range which makes ε_θ reach to extreme value, but only θ_{max} makes ε_θ reach to maximal value. So normal strain and shear strain of the critical plane can be represented as:

$$\overline{\varepsilon_\theta} = \frac{1-\nu}{2} \varepsilon_a \sin \omega t + \frac{1+\nu}{2} \varepsilon_a \sin \omega t \cos 2\overline{\theta}$$
$$+ \frac{1}{2} \lambda \varepsilon_a \sin \omega t \sin 2\overline{\theta} \quad (25)$$

$$\frac{\overline{\gamma_{xy}}}{2} = \frac{1+\nu}{2} \varepsilon_a \sin \omega t \sin 2\overline{\theta} - \frac{1}{2} \lambda \varepsilon_a \sin \omega t \cos 2\overline{\theta} \quad (26)$$

The equivalent strain can be represented as:

$$\varepsilon_{eq} = \left[\overline{\varepsilon_\theta} + \frac{1}{3} \left(\frac{\overline{\gamma_\theta}}{2} \right)^2 \right]^{\frac{1}{2}} \quad (27)$$

Combining Eq.(13) with Eq.(27), the multiaxial fatigue damage model can be given as:

$$N_f = \frac{M_0}{1+p+\beta} \left\{ K \left[\left[\overline{\varepsilon_\theta} + \frac{1}{3} \left(\frac{\overline{\gamma_\theta}}{2} \right)^2 \right]^{\frac{1}{2}} \right]^n \right\}^{-\beta} \quad (28)$$

5. Experiments and Results

The material under investigation was 06Cr19Ni10 steel, a kind of widely used material in engineering. All indexes satisfy property requirement of 06Cr19Ni10 steel and the data will be the reference of the parameter of fatigue test.

In this paper, the reported fatigue life corresponds to the moment when a visible crack was found on the specimen surface. An Instron hydraulic tension-torsion loading frame (Figure 2) was used for the uniaxial and multiaxial proportional fatigue tests. The testing system was equipped with the Instron 8800 electronic control, computer control, and data acquisition.

Figure 2. Fatigue testing machine

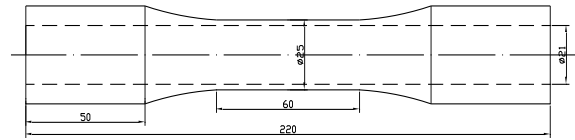The uniaxial results were listed in Table 1.

Table 1: Fatigue life of uniaxial experiment

ε(%)	0.48	0.59	0.69	0.8
N_f(cycles)	3881	2830	1962	1403

The parameters of Eq. (13) can be fitted using the uniaxial experiment data:

$$\frac{M_0{}^{\beta}}{1+p+\beta} = 7.3294 \times 10^{42}, \quad \beta = 13.5488$$

The shape of multiaxial fatigue sample is shown in Figure 3:

Figure 3. Shape of sample

The proposed model is used respectively to predict the crack initiation life when

$$\lambda_1 = \sqrt{3}, \lambda_2 = \sqrt{3}/2, \lambda_3 = 1/2.$$

The loading conditions are listed in Table 2:

Table 2. Amplitude of axial and torsional loading (%)

λ_1	σ	0.370	0.490	0.566	0.670	0.800
	γ	0.64	0.84	0.981	1.16	1.39
λ_2	σ	0.370	0.490	0.566	0.670	0.800
	γ	0.32	0.424	0.49	0.58	0.693
λ_3	σ	0.370	0.490	0.566	0.670	0.800
	γ	0.185	0.245	0.283	0.335	0.400

The way of loading is shown in Figure 4.
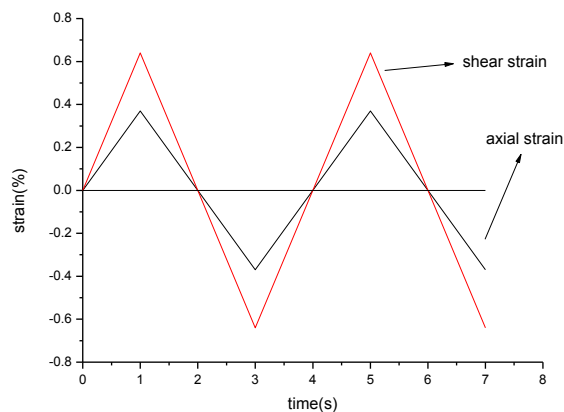
Figure 4. The way of loading

The experimental results and the predicted result are shown in Table 3:

Table 3. The data of multiaxial fatigue (cycles)

$\lambda=\sqrt{3}$	P	1751	1156	823	618	482
	E	1801	1209	856	632	493
$\lambda=\sqrt{3}/2$	P	1480	1613	1820	2209	2750
	E	1537	1594	1893	2284	2791
$\lambda=1/2$	P	1050	1187	1410	1721	2305
	E	971	1102	1371	1708	2277

P—predicted life; E—experimental life.

The predicted results using multiaxial nonlinear fatigue cumulative damage model are compared with the experimental results, and the comparison is shown in Figure5:
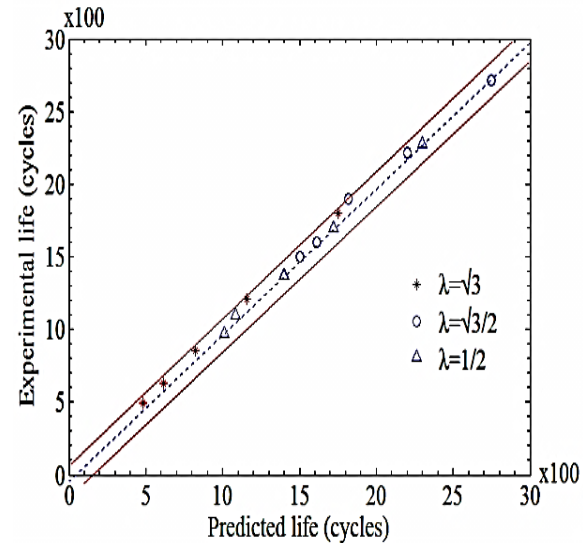

Figure 5. The comparison between predicted results and experimental results

Figure 5 shows the plots of the predicted life and experimental life when

$$\lambda_1 = \sqrt{3}, \lambda_2 = \sqrt{3}/2, \lambda_3 = 1/2.$$

It is obvious from the figure that life predictions based on the proposed approach were conservative within a factor of 8 for proportional loading. In this paper, the damage mechanics is applied to predict the crack initiation life that the fracture mechanics is unable to predict. At the same time, the physical significance of the critical plane method is considered. The multiaxial nonlinear fatigue cumulative damage model proposed in this paper makes use of the advantage of the above two method. It can be seen from the comparative analysis that this method can predict the crack initiation life under proportional loading well.

The parameters of the proposed model, such as the material constants and uniaxial fatigue data, can be easily obtained through theoretical analysis and the existing experimental data. On the basis of these parameters the crack initiation life can be well predicted. Thus, the new model can avoid conducting the multiaxial test which is time-consuming, money-consuming and troublesome and it is easy to apply in engineering.

Conclusion

The proposed method has been verified in comparison with the predicted results and experimental data. The method of combining damage mechanics with critical plane method can commendably predict the crack initiation life and it has a more practical value because the multiaxial fatigue damage model can predict the crack initiation life using the material constant and uniaxial fatigue data only.

References

[1] Dattoma V, Giancane S, Nobile R, et al. Fatigue life predicted under variable loading based on a new non-linear continuum damage mechanics model. International Journal of Fatigue Vol. 28 (2006) No 2, 89-95

[2] Tlilan H M, Al-Shyyab A S, Darabseh T, et al. Strain-Concentration Factor of Notched Cylindrical Austenitic Stainless Steel Bar with Double Slant Circumferential U-Notches Under Static Tension[J]. Jordan Journal of Mechanical and Industrial Engineering Vol. 1(2007) No. 2, 105-111.

[3] Brown M W, Miller K J. Mode I fatigue crack growth under biaxial stress at room and elevated temperature. Multiaxial Fatigue, ASTM STP, (1985) 853: 135-152.

[4] Hadoush A. On the Deformation Modes of Continuous Bending under Tension Test. Jordan Journal of Mechanical and Industrial Engineering Vol. 5 (2011) No. 6, 553-557.

[5] Almeanazel O T R. Total productive maintenance review and overall equipment effectiveness measurement[J]. Jordan Journal of Mechanical and Industrial Engineering Vol. 4 (2010) No. 4, 517-522.

[6] Lemaitre J, Chaboche J L. Mechanics of solid materials. Cambridge university press, 1994.

[7] Basaran C, Tang H. A damage mechanics based fatigue life predicted model for solder joints. Trans. ASME, J. Electron. Packaging Vol. 125 (2003) 120-125.

[8] Fatemi A, Socie D F. A Critical Plane Approach to Multiaxial Fatigue Damage Including out of Phase Loading. Fatigue & Fracture of Engineering Materials & Structures Vol. 11 (1988) No. 3, 149-165.

[9] Socie D. Critical plane approaches for multiaxial fatigue damage assessment. ASTM Special Technical Publication (1993) 1191: 7-7.

[10] Glinka G, Shen G, Plumtree A. A multiaxial fatigue strain energy density parameter related to the critical fracture plane[J]. Fatigue & Fracture of Engineering Materials & Structures Vol. 18 (1995) No. 1, 37-46.

[11] Chaboche J L. Continuous damage mechanics—a tool to describe phenomena before crack initiation. Nuclear Engineering and Design Vol. 64 (1981) No. 2, 233-247.

[12] Lemaitre J. Continuous damage mechanics model for ductile fracture. Transactions of the ASME. Journal of Engineering Materials and Technology Vol. 107(1985) No. 1, 83-89.

[13] Qiu J, Seth B B, Liang S Y, et al. Damage mechanics approach for bearing lifetime prognostics[J]. Mechanical systems and signal processing Vol.16 (2002) No. 5, 817-829.

[14] Kachanov L M. Rupture time under creep conditions. Problems of Continuum Mechanics (1961) 202-218.

[15] Socie D F. Multiaxial fatigue damage models[J]. Journal of Engineering Materials and Technology Vol. 109 (1987) No. 4, 293-298.

[16] Fatemi A, Yang L. Cumulative fatigue damage and life predicted theories: a survey of the state of the art for homogeneous materials. International Journal of Fatigue Vol. 20 (1998) No. 1, 9-34.

[17] You B R, Lee S B. A critical review on multiaxial fatigue assessments of metals[J]. International Journal of Fatigue Vol. 18 (1996) No. 4, 235-244.

[18] Sonsino C M. Multiaxial fatigue of welded joints under in-phase and out-of-phase local strains and stresses[J]. International Journal of Fatigue Vol. 17 (1995) No. 1, 55-70.

[19] Varvani-Farahani A. A new energy-critical plane parameter for fatigue life assessment of various metallic materials subjected to in-phase and out-of-phase multiaxial fatigue loading conditions. International Journal of Fatigue Vol. 22 (2000) No. 4, 295-305.

[20] Park J, Nelson D. Evaluation of an energy-based approach and a critical plane approach for predicting constant amplitude multiaxial fatigue life. International Journal of Fatigue Vol. 22 (2000) No. 1, 23-39.

[21] Chen X, Xu S, Huang D. A critical plane-strain energy density criterion for multiaxial low-cycle fatigue life under non-proportional loading[J]. Fatigue & Fracture of Engineering Materials & Structures Vol. 22 (1999) No. 8, 679-686.

[22] Karolczuk A, Macha E. A review of critical plane orientations in multiaxial fatigue failure criteria of metallic materials[J]. International Journal of Fracture Vol. 134 (2005) No. 3-4, 267-304.

[23] Shokrieh M M, Lessard L B. Multiaxial fatigue behaviour of unidirectional plies based on uniaxial fatigue experiments I. Modelling[J]. International Journal of Fatigue Vol. 19 (1997) No. 3, 201-207.

Static Bending Behavior of Functionally Graded Plates Subjected to Mechanical Loading

B. SiddaRedddy[a, *] , J. Suresh Kumar[b], C. EswaraReddy[c], K. Vijaya Kumar Reddy[d]

[a]*School of Mechanical Engineering, R.G.M. College of Engineering &Technology, Nandyal, Kurnool (Dt), Andhra Pradesh, India-518 501*

[b,d]*Department of Mechanical Engineering, J.N.T.U.H. College of Engineering, J.N.T.University, Hyderabad, India.*

[c] *The School of Engineering & Technology, SPMVV, Women's University, Tirupati, Chittoor (Dt) A.P, India*

Abstract

This paper presents analytical formulations and solutions for the bending behavior of simply supported functionally graded plates (FGPs) using Higher Order Shear Deformation Theory (HSDT) without enforcing zero transverse shear stresses on the top and bottom surfaces of the plate. It does not require shear correction factors. Material properties of the plate are assumed to vary in the thickness direction according to a power law distribution interns of the volume fractions of the constituents. The governing equations of motion and boundary conditions are derived using the principle of virtual work. Solutions are obtained for FGPs in closed-form using Navier's technique. The results of deflections and stresses are presented for simply supported boundary conditions. The present numerical results are compared with the available solutions in the literature for deflections and stresses, from which it can be concluded that the proposed theory results are very close agreement to the published ones. After validating the present theory results for FGM plates, the effect of side-to-thickness ratio, aspect ratio, modulus ratio, the volume fraction exponent,and through-the-thickness on the deflections and stresses are studied. The shear deformation effect and inhomogeneities played a greater role in estimating the deflctions and stress distribution in the functionally graded material plates.

1. Introduction

Laminated Composite materials are particularly attractive to aviation and aerospace applications because of their exceptional strength and stiffness-to-density ratios and superior physical properties. However, the sudden change in material properties across the interface between discrete materials can result in large interlaminar stresses leading to delamination. Furthermore, large plastic deformations at the interfaces may trigger the initiation and propagation of cracks in the material [1]. One way to overcome these adverse effects is to employ functionally graded materials in which the material properties are continually varied through the thickness direction by mixing two different materials. This is achieved by gradually changing the volume fraction of the constituent materials usually in the thickness direction only.

In the past, researchers on plates have received great attention and a variety of plate theories have been proposed to study the mechanical behavior of FGM plates. In particular, knowledge pertaining to static analysis is essential for optimal design of structures. For example, our numerical results clearly show that one could achieve an optimal design for FGM plates with a suitable power law index "*n*". It is useful to present some developments in plate theory. The Classical Laminate Plate Theory (CLPT) [2], which is an extension of the Classical Plate Theory (CPT), provides acceptable results only for the analysis of thin plates and neglects the transverse shear effects. However, for moderately thick plates, CPT underpredicts deflections and overpredicts buckling loads and natural frequencies. The First-order Shear Deformation Theories (FSDTs) are based on Reissner's [3] and Mindlin's [4] accounts for the transverse shear deformation effect by means of a linear variation of in-plane displacements and stresses through the thickness of the plate, but requires a correction factor to satisfy the free transverse shear stress conditions on the top and bottom surfaces of the plate. Although, the FSDT provides a sufficiently accurate description of response for thin to moderately thick plates, it is not convenient to use due to difficulty with determination of the correct value of shear correction factor [5]. In order to overcome the limitations of FSDT, many HSDTs were developed; they involved higher order terms in Taylors expansions of the displacements in the

---

* Corresponding author. e-mail: bsrrgmcet@gmail.com.

thickness coordinate, notable among them are Reddy [6], Zenkour [7-9], Kant and Co-workers [10-15], Kadkhodayan [16], Matsunaga [17,18], Xiang [19] and Ferreira [20]. A good literature review of these theories is available in Refs. [21-23]. Neves et al. [20, 24] derived a Higher-order Shear Deformation Theory (HSDT) for modeling of functionally graded material plates and focused on the thickness stretching issue on the static, free vibration, and buckling analysis of FGM plates by a meshless technique. They used the virtual work principle of displacements under Carrera's Unified Formulation (CUF) to obtain the governing equations and boundary conditions. The bending and Eigen problems are solved by collocation with radial basis functions. Mechab et al. [25] developed a two-variable refined plate theory to the bending analysis of functionally graded plates. Mantari and Soares [26] used the new trigonometric higher order shear deformation theory with stretching effect to develop the analytical solutions for static analysis of functionally graded materials. They employed the virtual work principle to derive the governing equations of motion and boundary conditions. The bi-sinusoidal load in the transverse direction is applied to the simply supported FGM plate to obtain the Navier-type solution.

Birman and Byrd [28] presented a review of the principle developments in FGMs on the recent work published since 2000 in diverse areas relevant to various aspects of the theory and applications of FGM that include homogenization of particulate FGM, heat transfer issues, stress, stability and dynamic analyses, testing, manufacturing and design, applications, and fracture.

Reddy [29] developed analytical solutions and finite element models based on third order shear deformation plate theory to analyze the isotropic functionally graded rectangular plates accounting for the thermo-mechanical coupling, time dependency, and the von Kármán-type geometric non-linearity. He assumed that the material properties vary according to power-law distribution in terms of volume fractions of the constituents.

Cheng and Batra [30-32] used a third order shear deformation plate theory to establish the relationships between its deflections predicted by third order and higher order shear deformation theories and that given by the classical Kirchhoff plate theory. They also used the third order theory to study the buckling and steady state vibrations of a simply supported functionally gradient isotropic polygonal plate resting on a Winkler Pasternak elastic foundation and subjected to uniform in-plane hydrostatic loads. They assumed that the Young's modulus and the Poisson ratio of the material of the plate vary only in the thickness direction and also considered the rotary inertia effects. The same authors used asymptotic expansion method to study three-dimensional mechanical deformations of an isotropic linear thermo-elastic elliptic plate, and the deformations due to thermal loads are straightforwardly found.

Gasik et al. [33] optimized the symmetric FGM plates and disks during sintering, using computer simulation to minimize the functionally graded material distortion, to avoid cracks and to generate an optimum residual stress distribution considering the processing parameters such as green density, particle size and composition profiles.

Batra and Love [34] studied the initiation and propagation of adiabatic shear bands in FGMs deformed at high strain rates in plane-strain tension.

Qian et al. [35] used meshless local Petrov–Galerkin (MLPG) Method to analyze plane strain static thermoelastic deformations of a simply supported functionally graded (FG) plate. They concluded that the number of nodes required to obtain an accurate solution for a FG plate is considerably more than that needed for a homogeneous plate.

Gilhooley et al. [36] used a meshless local Petrov–Galerkin (MLPG) method, and a Higher-Order Shear and Normal Deformable Plate Theory (HOSNDPT) to analyze infinitesimal deformations of a functionally graded thick elastic plate. They employed multiquadrics and thin plate spline radial basis functions for constructing the trail solutions, while a fourth-order spline function is used as the weight/test function over a local sub domain. They used Mori–Tanaka homogenization technique to compute the effective material properties.

Talha and Singh [37] developed the theoretical formulations based on higher order shear deformation theory with a considerable amendment in the transverse displacement using the finite element method to analyze the thermo-mechanical deformation behavior of shear deformable FGM plates.

Daouadji et al. [38] presented a theoretical formulation, Navier's solutions of rectangular plates based on a new higher order shear deformation model to study the static response of FG plates enforcing traction-free boundary conditions on plate surfaces. They also studied the effect of ceramic volume fraction, volume fractions profiles, aspect ratios, and length to thickness ratios on the static response of FG plates.

Xiang and Kang [39] used nth-order shear deformation theory and meshless global collocation method based on the thin plate spline radial basis function to the bending analysis of functionally graded plates.

Most of the above theories do not account for transverse shear stresses on the top and bottom surfaces of the plate. This should be considered in modeling of the FGPs, because of the transverse shear stresses and strains are not zero, when the FGPs used in aerospace structures may be subjected to transverse load/pressure on either side of the plate.

In the present paper, analytical formulations and solutions for the static analysis of Functionally Graded Plates (FGPs) using Higher-Order Shear Deformation Theory (HSDT) are developed without enforcing zero transverse shear stress on the top and bottom surfaces of the plate. This does not require shear correction factors. The plate material is graded through the thickness direction. The plate's governing equations and its boundary conditions are derived by employing the principle of virtual work. Navier-type analytical solution is obtained for plates subjected to transverse sinusoidal load for simply supported boundary conditions. The present numerical results are compared with the available solutions in the literature for deflections and stresses, from which it can be concluded that the proposed theory results are very close agreement to the published ones. After validating the present theory results for FGM plates, the effect of side-to-thickness ratio, aspect ratio, modulus

ratio, the volume fraction exponent,and through-the-thickness on the deflections and stresses are studied. The shear deformation effect and inhomogeneities played a greater role in estimating the deflctions and stress distribution in the functionally graded material plates.

2. Theoretical Formulation

In formulating the higher-order shear deformation theory, a rectangular plate of length a, width b and thickness h is considered, that composed of functionally graded material through the thickness. Figure 1 shows the functionally graded material plate with the rectangular Cartesian coordinate system x, y and z. The material properties are assumed to be varied in the thickness direction only and the bright and dark areas correspond to ceramic and metal particles respectively. On the top surface (z=+h/2), the plate is composed of full ceramic and graded to the bottom surface (z=-h/2) that composed of full metal. The reference surface is the middle surface of the plate (z=0). The functionally graded material plate properties are assumed to be the function of the volume fraction of constituent materials. The functional relationship between the material property and the thickness coordinates is assumed to be [9, 29,40]:

$$P(z) = (P_t - P_b)\left(\frac{z}{h} + \frac{1}{2}\right)^n + P_b \qquad (1)$$

where P denoted\s the effective material property, P_t, and P_b denotes the property on the top and bottom surface of the plate, respectively, and n is the material variation parameter that dictates the material variation profile through the thickness. The effective material properties of the plate, including Young's modulus, E, density, ρ, and shear modulus, G, vary according to Eq. (1), and poisons ratio (υ) is assumed to be constant.
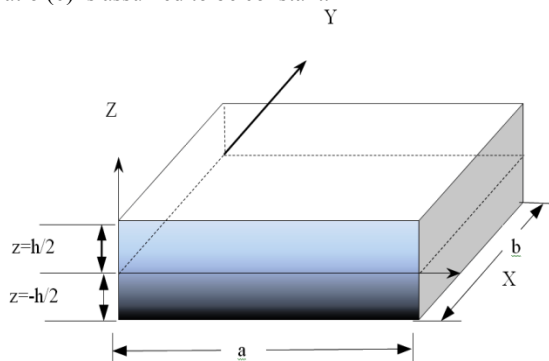

Figure 1.Functionally graded plate and coordinates

2.1. Displacement Models

In order to approximate 3D plate problem to a 2D one, the displacement components u (x, y, z, t), v (x, y, z, t) and w (x, y, z, t) at any point in the plate are expanded in terms of the thickness coordinate. The elasticity solution indicates that the transverse shear stress varies parabolically through the plate thickness. This requires the use of a displacement field, in which the in-plane displacements are expanded as cubic functions of the thickness coordinate. In addition, the transverse normal strain may vary nonlinearly through the plate thickness. A

higher-order shear deformation for composite laminated plates was developed by Pandya and Kant [41]. This paper extends this theory to functionally graded material plates. The displacement field is described in the following equations:

$$
\begin{aligned}
u(x,y,z) &= u_o(x,y) + z\theta_x(x,y) + z^2 u_o^*(x,y) \\
&+ z^3\theta_x^*(x,y) \\
v(x,y,z) &= v_o(x,y) + z\theta_y(x,y) + z^2 v_o^*(x,y) \\
&+ z^3\theta_y^*(x,y) \\
w(x,y,z) &= w_o(x,y)
\end{aligned}
\qquad (2)
$$

Where u_o, v_o, w_o, denote the displacements of a point (x, y) on the mid plane.

θ_x, θ_y are rotations of the normal to the mid plane about y and x-axes

u_0^*, v_0^*, θ_x^*, θ_y^* are the higher order deformation terms defined at the mid plane.

By substitution of displacement relations from Eq. (2) into the strain displacement equations of the classical theory of elasticity the following relations are obtained:

$$
\begin{aligned}
\varepsilon_x &= \varepsilon_{xo} + zk_x + z^2\varepsilon_{xo}^* + z^3 k_x^* \\
\varepsilon_y &= \varepsilon_{yo} + zk_y + z^2\varepsilon_{yo}^* + z^3 k_y^* \\
\varepsilon_z &= 0 \\
\gamma_{xy} &= \varepsilon_{xyo} + zk_{xy} + z^2\varepsilon_{xyo}^* + z^3 k_{xy}^* \\
\gamma_{yz} &= \phi_y + z\varepsilon_{yzo} + z^2\phi_y^* \\
\gamma_{xz} &= \phi_x + z\varepsilon_{xzo} + z^2\phi_x^*
\end{aligned}
\qquad (3)
$$

Where

$$\varepsilon_{xo} = \frac{\partial uo}{\partial x}, \varepsilon_{yo} = \frac{\partial vo}{\partial y}$$

$$\varepsilon_{xyo} = \frac{\partial uo}{\partial y} + \frac{\partial vo}{\partial x}$$

$$k_x = \frac{\partial\theta_x}{\partial x}, \quad k_y = \frac{\partial\theta_y}{\partial y}, \quad k_{xy} = \frac{\partial\theta_x}{\partial y} + \frac{\partial\theta_y}{\partial x}$$

$$k_x^* = \frac{\partial\theta_x^*}{\partial x}, \quad k_y^* = \frac{\partial\theta_y^*}{\partial y}, \quad k_{xy}^* = \frac{\partial\theta_x^*}{\partial y} + \frac{\partial\theta_y^*}{\partial x}$$

$$\varepsilon_{xo}^* = \frac{\partial u_o^*}{\partial x}, \quad \varepsilon_{yo}^* = \frac{\partial v_o^*}{\partial y}, \quad \varepsilon_{xyo}^* = \frac{\partial u_o^*}{\partial y} + \frac{\partial v_o^*}{\partial x}$$

$$\phi_y = \theta_y + \frac{\partial wo}{\partial y}, \quad \phi_x = \theta_x + \frac{\partial wo}{\partial x}$$

$$\varepsilon_{yzo} = 2v_o^*, \quad \varepsilon_{xzo} = 2u_o^*, \quad \phi_y^* = 3\theta_y^*, \quad \phi_x^* = 3\theta_x^*$$

2.2. Elastic Stress-Strain Relations

The elastic stress-strain relations depend on which assumption of $\varepsilon_z = 0$. In the case of functionally graded materials the constitutive equations can be written as:

$$\begin{Bmatrix}\sigma_x \\ \sigma_y \\ \tau_{xy} \\ \tau_{yz} \\ \tau_{xz}\end{Bmatrix} = \begin{bmatrix} Q_{11} & Q_{12} & 0 & 0 & 0 \\ Q_{12} & Q_{22} & 0 & 0 & 0 \\ 0 & 0 & Q_{33} & 0 & 0 \\ 0 & 0 & 0 & Q_{44} & 0 \\ 0 & 0 & 0 & 0 & Q_{55} \end{bmatrix} \begin{Bmatrix}\varepsilon_x \\ \varepsilon_y \\ \gamma_{xy} \\ \gamma_{yz} \\ \gamma_{xz}\end{Bmatrix} \quad (4)$$

Where $\sigma = (\sigma_x, \sigma_y, \tau_{xy}, \tau_{yz}, \tau_{xz})^t$ are the stresses
$\varepsilon = (\varepsilon_x, \varepsilon_y, \gamma_{xy}, \gamma_{yz}, \gamma_{xz})^t$ are the strains with respect to the axes

Q_{ij}'s are the plane stress reduced elastic coefficients in the plate axes that vary through the plate thickness given by:

$$Q_{11} = Q_{22} = \frac{E(Z)}{1-\upsilon^2} = \frac{(E_c - E_m)\left(\frac{z}{h}+\frac{1}{2}\right)^n + E_m}{1-\upsilon^2}$$

$$Q_{12} = Q_{21} = \upsilon Q_{11} \quad (5)$$

$$Q_{33} = Q_{44} = Q_{55} = \frac{(1-\upsilon^2)}{2(1+\upsilon)}Q_{11}$$

Where E_c is the modulus of Elasticity of the ceramic material and E_m is the modulus of elasticity of the metal.

2.3. Governing Equations of Motion

The work, done by actual forces in moving through virtual displacements that are consistent with the geometric constraints of a body, is set to zero to obtain the equation of motion; this is known as energy principle. It is useful for: (a) deriving governing equations and the boundary conditions, and (b) obtaining approximate solutions by virtual methods.

Energy principles provide alternative means to obtain the governing equations and their solutions. In the present study, the principle of virtual work is used to derive the equations of motion for functionally graded material plates.

The governing equations of displacement model in Eq. (2) will be derived using the dynamic version of the principle of virtual displacements [42], i.e.:

$$\int_0^T (\delta U + \delta V - \delta K)\, dt = 0 \quad (6)$$

Where δU = virtual strain energy
δV = virtual work done by applied forces
δK = virtual kinetic energy
$\delta U + \delta V$ = total potential energy.

The virtual strain energy, work done and kinetic energy are given by:

$$\delta U = \int_A \left\{ \int_{-h/2}^{h/2} \left[\begin{array}{c} \sigma_x \delta \in_x + \sigma_y \delta \in_y + \tau_{xy} \delta \gamma_{xy} \\ + \tau_{xz} \delta \gamma_{xz} + \tau_{yz} \delta \gamma_{yz} \end{array} \right] dz \right\} dx\, dy \quad (7)$$

$$\delta V = -\int q \delta w_0\, dx\, dy \quad (8)$$

$$\delta K = \int_A \left\{ \int_{-h/2}^{h/2} \rho_0 \left[\begin{array}{c} \left(\dot{u}_0 + Z\dot{\theta}_x + Z^2 \dot{u}_0^* + Z^3 \dot{\theta}_x^*\right) \\ \left(\delta\dot{u}_0 + Z\delta\dot{\theta}_x + Z^2 \delta\dot{u}_0^* + Z^3 \delta\dot{\theta}_x^*\right) \\ + \left(\dot{v}_0 + Z\dot{\theta}_y + Z^2 \dot{v}_0^* + Z^3 \dot{\theta}_y^*\right) \\ \left(\delta\dot{v}_0 + Z\delta\dot{\theta}_y + Z^2 \delta\dot{v}_0^* + Z^3 \delta\dot{\theta}_y^*\right) \\ + \dot{w}_0 \delta\dot{w}_0 \end{array} \right] dz \right\} dx\, dy \quad (9)$$

Where

q = distributed load over the surface of the plate.
ρ_0 = density of plate material

Substituting for δU, δV and δK in the virtual work statement in Eq. (6) and integrating through the thickness, integrating by parts and collecting the coefficients of

$$\delta u_o, \delta v_o, \delta w_o, \delta\theta_x, \delta\theta_y, \delta u_o^*, \delta v_o^*, \delta\theta_x^*, \delta\theta_y^*$$

the following equations of motion are obtained:

$$\delta u_0 : \frac{\partial N_x}{\partial x} + \frac{\partial N_{xy}}{\partial y} = I_1 \ddot{u}_0 + I_2(\ddot{\theta}_x) + I_3 \ddot{u}_0^* + I_4 \ddot{\theta}_x^*$$

$$\delta v_0 : \frac{\partial N_y}{\partial y} + \frac{\partial N_{xy}}{\partial x} = I_1 \ddot{v}_0 + I_2(\ddot{\theta}_y) + I_3 \ddot{v}_0^* + I_4 \ddot{\theta}_y^*$$

$$\delta w_0 : \frac{\partial Q_x}{\partial x} + \frac{\partial Q_y}{\partial y} + q = I_1 \ddot{w}_0$$

$$\delta\theta_x : \frac{\partial M_x}{\partial x} + \frac{\partial M_{xy}}{\partial y} - Q_x = I_2 \ddot{u}_0 + I_3(\ddot{\theta}_x) + I_4 \ddot{u}_0^* + I_5 \ddot{\theta}_x^*$$

$$\delta\theta_y : \frac{\partial M_y}{\partial y} + \frac{\partial M_{xy}}{\partial x} - Q_y = I_2 \ddot{v}_0 + I_3(\ddot{\theta})_y + I_4 \ddot{v}_0^* + I_5 \ddot{\theta}_y^*$$

$$\delta u_0^* : \frac{\partial N_x^*}{\partial x} + \frac{\partial N_{xy}^*}{\partial y} - 2S_x = I_3 \ddot{u}_0 + I_4(\ddot{\theta}_x) + I_5 \ddot{u}_0^* + I_6 \ddot{\theta}_x^*$$

$$\delta v_0^* : \frac{\partial N_y^*}{\partial y} + \frac{\partial N_{xy}^*}{\partial x} - 2S_y = I_3 \ddot{v}_0 + I_4(\ddot{\theta})_y + I_5 \ddot{v}_0^* + I_6 \ddot{\theta}_y^*$$

$$\delta\theta_x^* : \frac{\partial M_x^*}{\partial x} + \frac{\partial M_{xy}^*}{\partial y} - 3Q_x^* = I_4 \ddot{u}_0 + I_5(\ddot{\theta}_x) + I_6 \ddot{u}_0^* + I_7 \ddot{\theta}_x^*$$

$$\delta\theta_y^* : \frac{\partial M_y^*}{\partial y} + \frac{\partial M_{xy}^*}{\partial x} - 3Q_y^* = \quad (10)$$

$$I_4 \ddot{v}_0 + I_5(\ddot{\theta}_y) + I_6 \ddot{v}_0^* + I_7 \ddot{\theta}_y^*$$

Where the force and moment resultants are defined as:

$$\begin{Bmatrix} N_x & | & N_x^* \\ N_y & | & N_y^* \\ N_{xy} & | & N_{xy}^* \end{Bmatrix} = \sum_{L=1}^n \int_{\frac{-h}{2}}^{\frac{h}{2}} \begin{Bmatrix} \sigma_x \\ \sigma_y \\ \tau_{xy} \end{Bmatrix} \left[1 \mid z^2 \right] dz \quad (11)$$

197

$$\begin{Bmatrix} M_x & | & M_x^* \\ M_y & | & M_y^* \\ M_{xy} & | & M_{xy}^* \end{Bmatrix} = \sum_{L=1}^{n} \int_{\frac{-h}{2}}^{\frac{h}{2}} \begin{Bmatrix} \sigma_x \\ \sigma_y \\ \tau_{xy} \end{Bmatrix} \begin{bmatrix} z & | & z^3 \end{bmatrix} dz \quad (12)$$

And the transverse force resultants and the inertias are given by:

$$\begin{Bmatrix} Q_x & | & S_x & | & Q_x^* \\ Q_y & | & S_y & | & Q_y^* \end{Bmatrix} = \sum_{L=1}^{n} \int_{\frac{-h}{2}}^{\frac{h}{2}} \begin{Bmatrix} \tau_{xz} \\ \tau_{yz} \end{Bmatrix} \begin{bmatrix} 1 & | & z & | & z^2 \end{bmatrix} dz \quad (13)$$

$$I_1, I_2, I_3, I_4, I_5, I_6, I_7 =$$

$$\int_{-h/2}^{h/2} \left[(\rho_c - \rho_m) \left(\frac{2z - h}{2h} \right)^n + \rho_m \right] \quad (14)$$

$$\left(1, z, z^2, z^3, z^4, z^5, z^6 \right) dz$$

The resultants in Equations (11)-(13) can be related to the total strains in Eq. (4) by the following matrix:

$$: \begin{Bmatrix} N \\ N^* \\ -- \\ M \\ M^* \\ -- \\ Q \\ Q^* \end{Bmatrix} = \begin{bmatrix} A & | & B & | & 0 \\ B^t & | & D_b & | & 0 \\ 0 & | & 0 & | & D_s \end{bmatrix} \begin{Bmatrix} \varepsilon_0 \\ \varepsilon_0^* \\ -- \\ K_s \\ K^* \\ -- \\ \phi \\ \phi^* \end{Bmatrix} \quad (15)$$

Where,

$$N = [N_x \ N_y \ N_{xy}]^t \ ; \ N^* = [N_x^* \ N_y^* \ N_{xy}^*]^t$$

N, N^* are called the in-plane force resultants

$$M = [M_x \ M_y \ M_{xy}]^t \ ; \ M^* = [M_x^* \ M_y^* \ M_{xy}^*]^t$$

M, M^* are called as moment resultants

$$Q = [Q_x \ Q_y]^t \ ; \ Q^* = [S_x \ S_y \ Q_x^* \ Q_y^*]^t$$

Q, Q^* denotes the transverse force result

$$\varepsilon_0 = [\varepsilon_{x0} \ \varepsilon_{y0} \ \varepsilon_{xy0}]^t \ ; \varepsilon_0^* = [\varepsilon_{x0}^* \ \varepsilon_{y0}^* \ \varepsilon_{xy0}^*]^t$$

$$K_s = [K_x \ K_y \ K_{xy}]^t \ ; \ K^* = [K_x^* \ K_y^* \ K_{xy}^*]^t$$

$$\phi = [\phi_x \ \phi_y]^t \ ; \ \phi^* = [\varepsilon_{xz0} \ \varepsilon_{yz0} \ \phi_x^* \ \phi_y^*]^t$$

The matrices [A], [B], [D], and [Ds] are the plate stiffness whose elements can be calculated using Eq. (4), and Eq. (11)-(13).

3. Analytical Solutions

Rectangular plates are generally classified by referring to the type of support used. We are here concerned with the analytical solutions of the Eq. (10) - (15) for simply supported FG plates. Exact solutions of the partial

differential Eq. (10) an arbitrary domain and for general boundary conditions are difficult. Although, the Navier-type solutions can be used to validate the present higher order theory, more general boundary conditions will require solution strategies involving, e.g., boundary discontinuous double Fourier series approach.

Solution functions that completely satisfy the boundary conditions in the Equations below are assumed as follows:

$$u_0(x, y, t) = \sum_{m=1}^{\infty} \sum_{n=1}^{\infty} U_{mn} \cos \alpha x \sin \beta y;$$
$$0 \le x \le a; \ 0 \le y \le b \qquad 16(a)$$

$$v_0(x, y, t) = \sum_{m=1}^{\infty} \sum_{n=1}^{\infty} V_{mn} \sin \alpha x \cos \beta y;$$
$$0 \le x \le a; \ 0 \le y \le b \qquad 16(b)$$

$$w_0(x, y, t) = \sum_{m=1}^{\infty} \sum_{n=1}^{\infty} W_{mn} \sin \alpha x \sin \beta y;$$
$$0 \le x \le a; \ 0 \le y \le b \qquad 16(c)$$

$$\theta_x(x, y, t) = \sum_{m=1}^{\infty} \sum_{n=1}^{\infty} X_{mn} \cos \alpha x \sin \beta y;$$
$$0 \le x \le a; \ 0 \le y \le b \qquad 16(d)$$

$$\theta_y(x, y, t) = \sum_{m=1}^{\infty} \sum_{n=1}^{\infty} Y_{mn} \sin \alpha x \cos \beta y;$$
$$0 \le x \le a; \ 0 \le y \le b \qquad 16(e)$$

$$u_0^*(x, y, t) = \sum_{m=1}^{\infty} \sum_{n=1}^{\infty} U_{mn}^* \cos \alpha x \sin \beta y;$$
$$0 \le x \le a; \ 0 \le y \le b \qquad 16(f)$$

$$V_o^*(x, y, t) = \sum_{m=1}^{\infty} \sum_{n=1}^{\infty} V_{mn}^* \sin \alpha x \cos \beta y;$$
$$0 \le x \le a; \ 0 \le y \le b \qquad 16(g)$$

$$\theta_x^*(x, y, t) = \sum_{m=1}^{\infty} \sum_{n=1}^{\infty} X_{mn}^* \cos \alpha x \sin \beta y;$$
$$0 \le x \le a; \ 0 \le y \le b \qquad 16(h)$$

$$\theta_y^*(x, y, t) = \sum_{m=1}^{\infty} \sum_{n=1}^{\infty} Y_{mn}^* \sin \alpha x \cos \beta y;$$
$$0 \le x \le a; \ 0 \le y \le b \qquad 16(i)$$

Where

$$\alpha = \frac{m\pi}{a} \text{ and } \beta = \frac{n\pi}{b}$$

The Mechanical load is expanded in double Fourier sine series as:

$$q(x, y,) = \sum_{m=1}^{\infty} \sum_{n=1}^{\infty} Q_{mn} \sin \alpha x \sin \beta y \qquad (17)$$

Substituting Eq. (16a) - (16i) into Eq. (10) and collecting the coefficients we obtain:

$$[S]_{9\times 9}\begin{Bmatrix} U_{mn} \\ V_{mn} \\ W_{mn} \\ X_{mn} \\ Y_{mn} \\ U_{nm}^{*} \\ V_{mn}^{*} \\ X_{mn}^{*} \\ Y_{mn}^{*} \end{Bmatrix}_{9\times 1} = \begin{Bmatrix} 0 \\ 0 \\ Q_{mn} \\ 0 \\ 0 \\ 0 \\ 0 \\ 0 \\ 0 \end{Bmatrix}_{9\times 1} \qquad (18)$$

For any fixed value of m and n. Solutions of the Eq. (18) are obtained for each m,n =1,2....as Umn, Vmn, Wmn, Xmn,Ymn.

The coefficients Umn, Vmn, Wmn, Xmn, Ymn,

$U_{mn}^{*}, V_{mn}^{*}, X_{mn}^{*}, Y_{mn}^{*}$ which are used to

compute $u_o, v_o, w_o, \theta_x, \theta_y, u_o^{*}, v_o^{*}, \theta_x^{*}, \theta_y^{*}$.

4. Results and Discussion

4.1. Comparative Studies

In this section, numerical examples are presented and discussed to verify the accuracy of the present higher-order shear deformation theory in predicting the deflections and stresses of a simply supported functionally graded material plate. For numerical results, an Al/Al$_2$O$_3$ Plate is considered and graded from aluminum (as metal) at the bottom to alumina (as ceramic) at the top surface of the plate. The material properties adopted here are:

Aluminium Young's modulus (E$_m$): 70GPa, density(ρ_m)= 2702 kg/m^3, and Poisson's ratio (υ): 0.3

Alumina Young's modulus (E$_c$): 380GPa, density (ρ_c)= 3800kg/m^3, and Poisson's ratio (υ): 0.3

For convenience, the transverse displacement, in-plane and the transverse shear stresses are presented in nondimensionalized form as:

$$\overline{w} = 10 w_0 \left(\frac{a}{2}, \frac{b}{2}\right) \times \frac{E_c h^3}{q a^4} \; ; \; \overline{\sigma}_x = \frac{h}{aq} \sigma_x \left(\frac{a}{2}, \frac{b}{2}, \frac{h}{2}\right)$$

$$\overline{\sigma}_y = \frac{h}{aq} \sigma_x \left(\frac{a}{2}, \frac{b}{2}, \frac{h}{3}\right); \overline{\tau}_{xy} = \frac{h}{aq} \tau_{xy} \left(0, 0, -\frac{h}{3}\right)$$

$$\overline{\tau}_{yz} = \frac{h}{aq} \tau_{yz} \left(\frac{a}{2}, 0, \frac{h}{6}\right); \overline{\tau}_{xz} = \frac{h}{aq} \tau_{xz} \left(0, \frac{b}{2}, 0\right)$$

and $\overline{z} = \dfrac{z}{h}$

In Table 1, we present results for in-plane longitudinal, normal stresses and transverse displacements for various material variation parameter *"n"* of the power law and for side-to-thickness ratios (a/h) is 10. The present results are compared with the Zenkour [9], Reddy [6], Touraiter [27] and Mechab [25].

The results from present higher-order shear deformation theory considering ε$_z$=0 are in good agreement with those from Touraiter [27] and Mechab [25] who also consider ε$_z$=0. It can also be seen that the effect of the exponent "n" of the power law on the dimensionless deflections and stresses of an FGM plate is being demonstrated in the results presented in Table 1. From Table 1, it is important to observe that as the plate becomes more and more metallic, the difference increases for maximum center deflection and maximum normal stress ($\overline{\sigma}_x$), while it decreases for normal stress ($\overline{\sigma}_y$). Also, it is noticed that the stresses for a fully ceramic plate are the same as that for a fully metal plate. This may be because of the fact that the plate is fully homogeneous at the top and bottom surface and the nondimensionalized stresses do not depend on the value of the modulus of elasticity.

Table 2 compares the deflections and transverse shear stresses in a square FG plate subjected to sinusoidal distributed load. For convenience, the transverse displacement, and the transverse shear stresses in Table 2 are presented in a nondimensionalized form as:

$$\overline{w} = w_0 \left(\frac{a}{2}, \frac{b}{2}\right) \times \frac{E_c}{qh}; \quad \overline{\tau}_{xz} = \frac{\tau_{xz}}{q} \left(0, \frac{b}{2}, 0\right)$$

It can be seen that the deflections and stresses are in good agreementg with the higher order shear deformation theory [18] and refined plate theory [25]. This allows us to conclude that the developed higher order shear deformation theory is good for modelling of simply supported FGM plates. Results in Table 1 and Table 2 should serve as benchmark results for future comparisons.

Table 1: Comparison of Non-dimensional Central deflections and stresses in a square FG-plate subjected to sinusoidal distributed load, a/h=10.

n	Source	$\overline{w}$	$\overline{\sigma}_x$	$\overline{\sigma}_y$	$\overline{\tau}_{xy}$	$\overline{\tau}_{yz}$	$\overline{\tau}_{xz}$
Ceramic	Ref.[9]	0.2960	1.995500	1.312100	0.706500	0.213200	0.246200
	Ref.[6]	0.29423	1.989150	1.310350	0.705570	0.190510	0.237780
	Ref.[27]	0.2960	1.995500	1.312100	0.706500	0.213200	0.246200
	Ref.[25]	0.2961	1.994300	1.312400	0.706700	0.212100	0.238600
	Present	**0.2961**	**1.99426**	**1.31238**	**0.706667**	**0.211994**	**0.238413**
0.2	Ref.[6]	0.33767	2.126710	1.309580	0.667570	0.180450	0.225320
	Present	**0.3599**	**2.259090**	**1.38728**	**0.720591**	**0.225440**	**0.242348**
0.5	Ref.[6]	0.4407	2.610510	1.471470	0.666680	0.190710	0.238170
	Present	**0.4537**	**2.61874**	**1.45902**	**0.691134**	**0.240484**	**0.243518**
1	Ref.[9]	0.5889	3.087000	1.489400	0.611000	0.262200	0.246200
	Ref.[6]	0.58895	3.085010	1.489800	0.611110	0.190710	0.238170
	Ref.[27]	0.5889	3.087000	1.489400	0.611000	0.262200	0.246200
	Ref.[25]	0.5890	3.085000	1.489800	0.611100	0.260800	0.238600
	Present	**0.5890**	**3.08782**	**1.49034**	**0.610704**	**0.254721**	**0.238405**
2	Ref.[9]	0.7573	3.609400	1.395400	0.544100	0.276300	0.226500
	Ref.[6]	0.75747	3.606640	1.395750	0.544340	0.180700	0.225680
	Ref.[27]	0.7573	3.609400	1.395400	0.544100	0.276300	0.226500
	Ref.[25]	0.7573	3.606700	1.396000	0.544200	0.273700	0.218600
	Present	**0.7578**	**3.61635**	**1.39638**	**0.543421**	**0.263908**	**0.222026**
3	Ref.[27]	0.8377	3.874200	1.274800	0.552500	0.271500	0.210700
	Ref.[25]	0.8375	3.870900	1.275600	0.552600	0.267700	0.202400
	Present	**0.8383**	**3.88527**	**1.27495**	**0.551783**	**0.260625**	**0.208393**
4	Ref.[27]	0.8819	4.069300	1.178300	0.566700	0.258000	0.202900
	Ref.[25]	0.8816	4.065500	1.179400	0.566900	0.253700	0.194400
	Present	**0.8823**	**4.08134**	**1.17786**	**0.566122**	**0.250169**	**0.201285**
5	Ref.[9]	0.91180	4.248800	1.102900	0.575500	0.242900	0.201700
	Ref.[6]	0.90951	4.242930	1.105390	0.573680	0.173070	0.216090
	Ref.[27]	0.9118	4.248800	1.102900	0.575500	0.242900	0.201700
	Ref.[25]	0.9112	4.244700	1.104100	0.575700	0.238500	0.193000
	Present	**0.9121**	**4.25983**	**1.1022**	**0.574958**	**0.237709**	**0.199975**
6	Ref.[27]	0.9356	4.424400	1.041700	0.580300	0.229600	0.204100
	Ref.[25]	0.9352	4.420100	1.042800	0.580600	0.225500	0.195400
	Present	**0.9357**	**4.43346**	**1.04095**	**0.579958**	**0.226524**	**0.202127**
7	Ref.[27]	0.9562	4.597100	0.990300	0.583400	0.219400	0.208100
	Ref.[25]	0.9557	4.592800	0.991500	0.583600	0.215700	0.199400
	Present	**0.9562**	**4.60395**	**0.98971**	**0.583103**	**0.217854**	**0.205747**
8	Ref.[27]	0.9750	4.766100	0.946600	0.585600	0.212100	0.212400
	Ref.[25]	0.9743	4.761900	0.947700	0.585800	0.208800	0.203700
	Present	**0.9749**	**4.77066**	**0.946138**	**0.585446**	**0.211753**	**0.209630**

n	Source	$\overline{w}$	$\overline{\sigma}_x$	$\overline{\sigma}_y$	$\overline{\tau}_{xy}$	$\overline{\tau}_{yz}$	$\overline{\tau}_{xz}$
9	Ref.[27]	0.9925	4.930300	0.909200	0.587500	0.207200	0.216400
	Ref.[25]	0.9922	4.926100	0.910300	0.587800	0.204200	0.207800
	Present	**0.9924**	**4.93267**	**0.908967**	**0.587472**	**0.207791**	**0.213196**
10	Ref.[27]	1.0089	5.089000	0.877500	0.589400	0.204100	0.219800
	Ref.[25]	1.0085	5.084900	0.878500	0.589600	0.201400	0.211400
	Present	**1.0089**	**5.08932**	**0.87743**	**0.589390**	**0.205434**	**0.216235**
Metal	Ref.[9]	1.60700	1.995500	1.312100	0.706500	0.213200	0.246200
	Ref.[6]	1.59724	1.989150	1.310350	0.705570	0.190510	0.237780
	Ref.[27]	1.6070	1.995500	1.312100	0.706500	0.213200	0.246200
	Ref.[25]	1.6074	1.994300	1.312400	0.706700	0.212100	0.238600
	Present	**1.6072**	**10.826**	**1.31238**	**0.706667**	**0.211994**	**0.238413**

Table 2: Comparison of Non-dimensional Central deflections and transverse shear stress in a square FG-plate subjected to sinusoidal distributed load

a/h	Power law index, *n*	$\overline{w}$			$\overline{\tau}_{xz}$		
		Ref.[18]	Ref.[25]	Present	Ref.[18]	Ref.[25]	Present
	0	20.98	21.46	21.4575	1.186	1.19	1.18735
	0.5	31.79	32.35	32.3549	1.209	1.217	1.21301
5	1	41.39	41.8	41.816	1.184	1.19	1.18719
	4	65.12	65.06	65.2529	1.076	0.969	1.0005
	10	76.21	76.72	76.7671	1.078	1.053	1.07547
	0	294.3	296.1	296.058	2.383	2.385	2.38413
	0.5	450.4	453.7	453.716	2.431	2.439	2.43518
10	1	587.5	589	589.03	2.383	2.385	2.38405
	4	882.3	881.6	882.341	2.175	1.943	2.01285
	10	1007	1008.5	1008.92	2.167	2.113	2.16235

4.2. Parametric Study

4.2.1. Effect of Side-to-Thickness Ratio

The variation of nondimensionalized displacements and stresses for various side to thickness ratios (a/h) and material variation parameter (n) for displacement model are shown in Figures 2 - 7. Figure 2 shows the variation of center deflection for various volume fraction exponents "n" and with different side-to-thickness ratios, respectively. It is observed that the deflection of FGM plate is between ceramic and metal and the deflection of metal rich plates is larger compared to ceramic rich plates, this is due to the fact that the modulus of elasticity of ceramic (Al_2O_3=380GPa) is higher than that of metal (Al:70GPa). Hence for FGM plates, the transverse deflection decreases as the volume fraction exponent, n, decreases, whereas it may be unchanged as the side-to-thickness ratio increases. The normal stresses increases with the increase of side-to-thickness ratio and decreases with the decrease of volume fraction exponent which can be seen in Figure 3 and Figure 4. Figures 5 - 7 show the variation of nondimensionalized shear stress for various side-to-thickness ratios and with different power-law index values. It can be seen that the longitudinal shear stress

($\overline{\tau}_{xy}$) increases with the increase of side-to-thickness ratio's and power-law index values. This is due to the decrease of the stiffness of the plate. The transversal shear stresses may be unchanged as the side-to-thickness ratio increases. The shear deformation effect is to increase the deflections and decrease the normal stresses, longitudinal and transverse shear stresses, especially for a/h≤5.
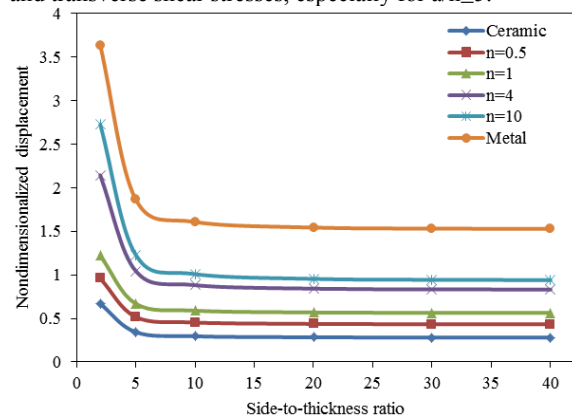

Figure 2. Nondimensionalized displacement ($\overline{w}$) as a function of side-to-thickness ratio (a/h) of an FGM plate for various values of power law index (n)
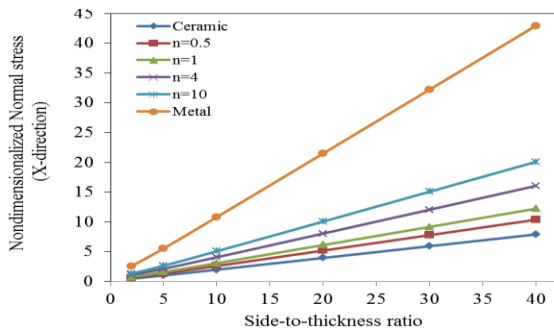
Figure 3. Nondimensionalized Normal stress ($\overline{\sigma}_x$) as a function of side-to-thickness ratio (a/h) of an FGM plate for various values of power law index (n)
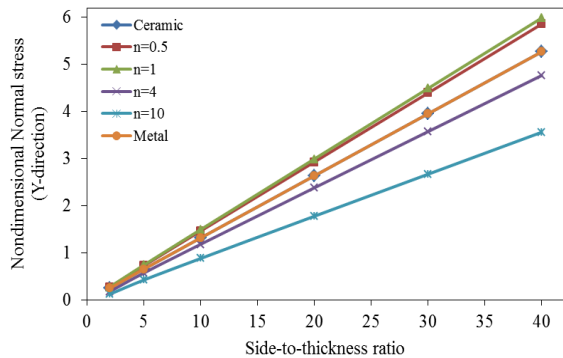

Figure 4. Nondimensionalized Normal stress ($\overline{\sigma}_y$) as a function of side-to-thickness ratio (a/h) of an FGM plate for various values of power law index (n)
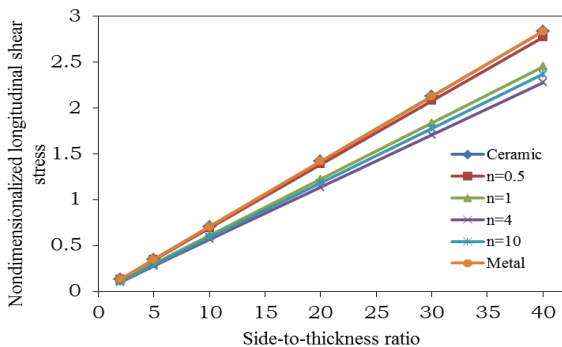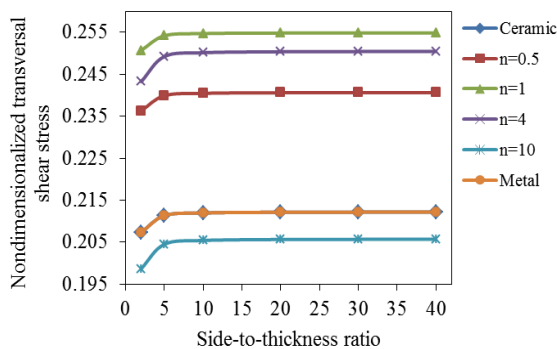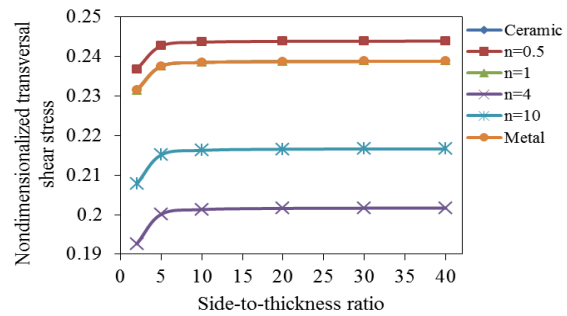

Figure 5: Nondimensionalized longitudinal shear stress ($\overline{\tau}_{xy}$) as a function of side-to-thickness ratio (a/h) of an FGM plate for various values of power law index (n)

Figure 6: Nondimensionalized transversal shear stress ($\overline{\tau}_{yz}$) as a function of side-to-thickness ratio (a/h) of an FGM plate for various values of power law index (n)

Figure 7: Nondimensionalized transversal shear stress ($\overline{\tau}_{xz}$) as a function of side-to-thickness ratio (a/h) of an FGM plate for various values of power law index (n)

4.2.2. Effect of Aspect Ratio

The effect of aspect ratios (a/b) and material variation parameter (n) for displacement model on nondimensionalized displacements and stresses are shown in Figures 8 - 13. From Figure 8 and Figure 9, it can be seen that the nondimensionalized center deflections and in-plane longitudinal stress ($\overline{\sigma}_x$) decreases with the increase of aspect ratio and volume fraction exponent. The nondimensionalized displacements are higher for metallic plates and lower for ceramic plates. This is because of more stiffness for ceramics plates than metal plates. Also, it is found that the response of FGM plates is intermediate to that of the ceramic and metal homogeneous plates. The normal stress ($\overline{\sigma}_y$) and the longitudinal shear stress ($\overline{\tau}_{xy}$) increases with the increase of aspect ratio up to 0.5 and then decreases, this can be observed in Figure 10 and Figure 11. It is due to the increase of elastic constants, Q_{ij}. It can be seen from Figure 12 that transversal shear stress ($\overline{\tau}_{yz}$) increases to a maximum when aspect ratio a/b=1 and power-law index=1. Further it decreases with the increase of aspect ratio. Figure 13 shows the variation of nondimensionalized transversal shear stress ($\overline{\tau}_{xz}$) with the aspect ratio for different power-law index values. It is observed that the transversal shear stress ($\overline{\tau}_{xz}$) decreases with the increase of aspect ratio. From Figure 8 to Figure 13, it can be seen that the effect of coupling increases as the aspect ratio increases.

4.2.3. Effect of Modulus Ratio

The effect of modulus ratios (E_m/E_c) and material variation parameter (n) for displacement model is shown in Figures 14 - 19. Figure 14 and Figure 15 show the variation of center deflection and in-plane longitudinal stress ($\overline{\sigma}_x$) with the modulus ratios and volume fraction exponent. The deflections and in-plane longitudinal stress decreases with the increase of volume fraction exponent and modulus ratios. From the figures, it is seen that maximum center deflections decrease smoothly with the decrease of volume fraction exponent, n, and metal-ceramic modulii ratio increases. This is because of the increase of the ratio of metal-ceramic modulii. The in-plane-normal stress ($\overline{\sigma}_y$) and the shear stresses variation with volume fraction exponent is depicted in Figures 16 - 19. The shear stresses, $\overline{\tau}_{xy}, \overline{\tau}_{xz}$ increase with the increase

of modulus ratio and maximum shear stress occurs at volume fraction exponent, n=0.2 and 0.5, respectively, while transverse shear stress, $\bar{\tau}_{yz}$ decreases with increase of volume fraction exponent.
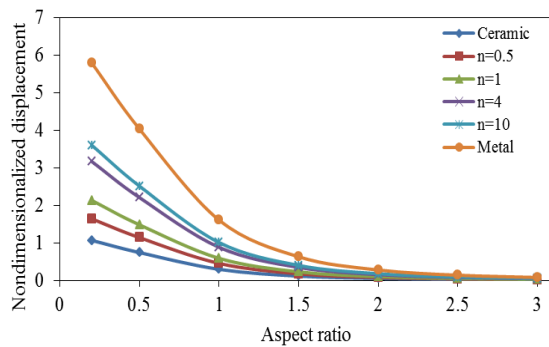

Figure 8: Nondimensionalized displacement ($\bar{w}$) as a function of aspect ratio (a/b) of an FGM plate for various values of power law index (n)
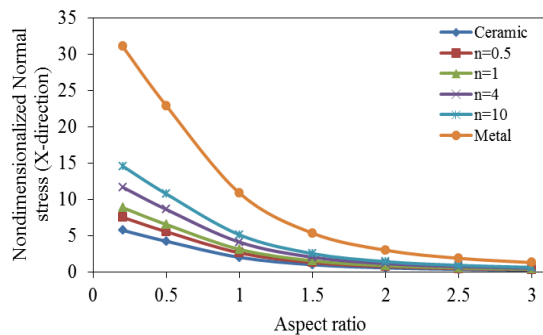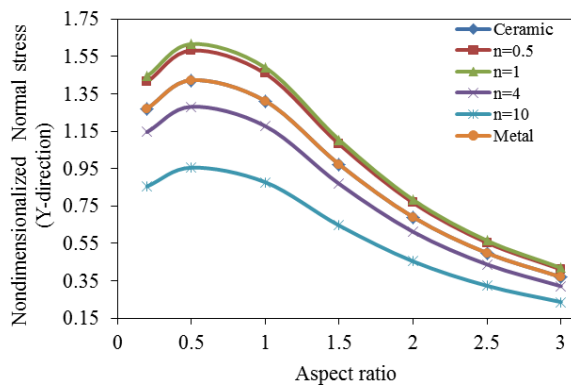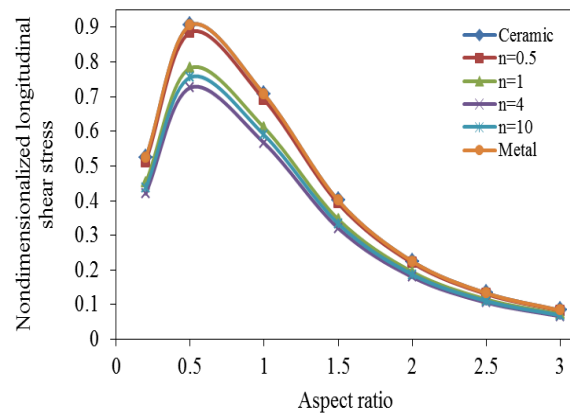

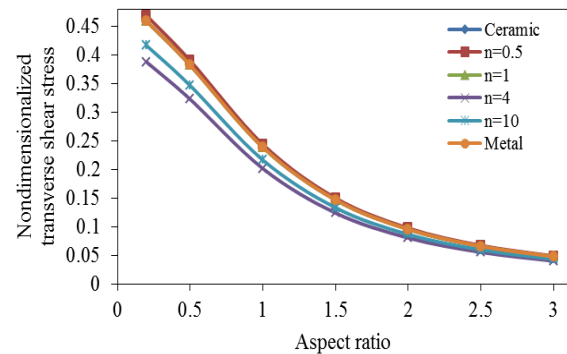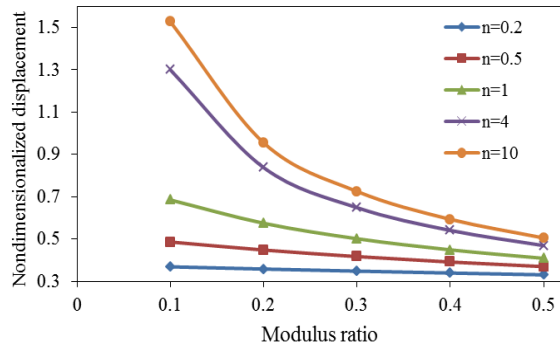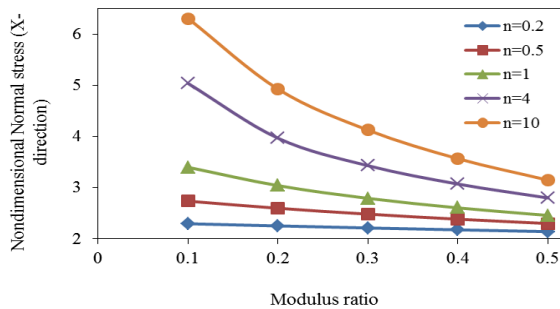**Figure 9**: Nondimensionalized Normal stress ($\bar{\sigma}_x$) as a function of aspect ratio (a/b) of an FGM plate for various values of power law index (n)
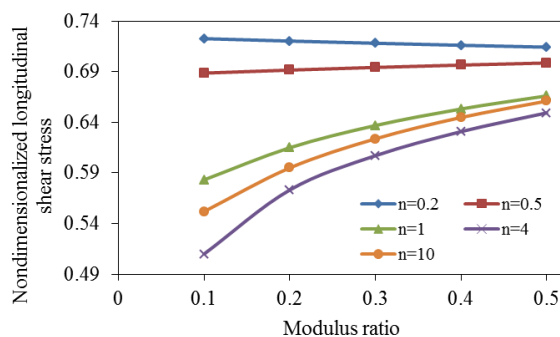

Figure 10: Nondimensionalized Normal stress ($\bar{\sigma}_y$) as a function of aspect ratio (a/b) of an FGM plate for various values of power law index (n)

Figure 11: Nondimensionalized longitudinal shear stress ($\bar{\tau}_{xy}$) as a function of aspect ratio (a/b) of an FGM plate for various values of power law index (n)
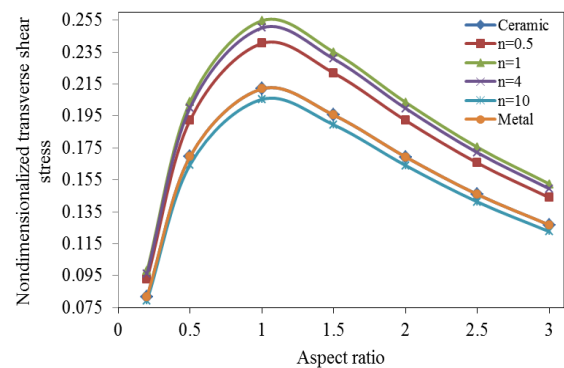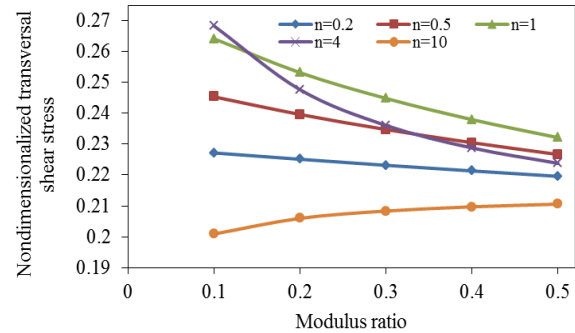

Figure 12: Nondimensionalized transversal shear stress ($\bar{\tau}_{yz}$) as a function of aspect ratio (a/b) of an FGM plate for various values of power law index (n)
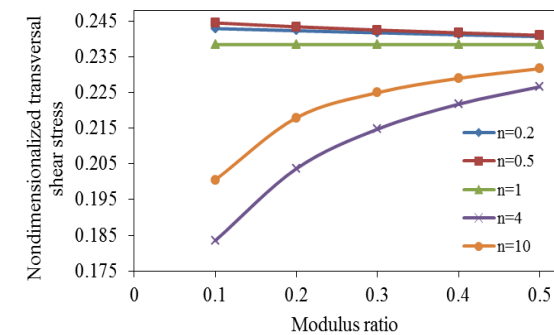

Figure 13: Nondimensionalized transversal shear stress ($\bar{\tau}_{xz}$) as a function of aspect ratio (a/b) of an FGM plate for various values of power law index (n)

Figure 14: Nondimensionalized displacement ($\overline{w}$) as a function of modulus ratio (E_c/E_m) of an FGM plate for various values of power law index (n)

Figure 15: Nondimensionalized Normal stress ($\overline{\sigma}_x$) as a function of modulus ratio (E_c/E_m) of an FGM plate for various values of power law index (n)
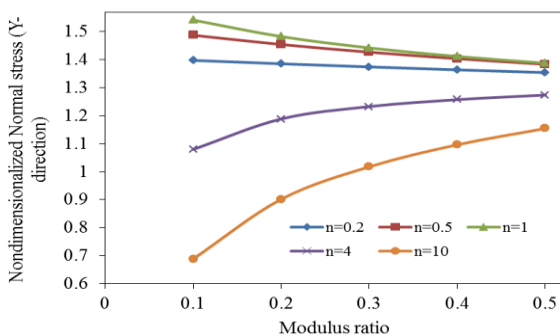
Figure 16: Nondimensionalized Normal stress ($\overline{\sigma}_y$) as a function of modulus ratio (E_c/E_m) of an FGM plate for various values of power law index (n)

Figure 17: Nondimensionalized longitudinal shear stress ($\overline{\tau}_{xy}$) as a function of modulus ratio (E_c/E_m) of an FGM plate for various values of power law index (n)

Figure 18: Nondimensionalized transversal shear stress ($\overline{\tau}_{yz}$) as a function of modulus ratio (E_c/E_m) of an FGM plate for various values of power law index (n) for model

Figure 19: Nondimensionalized transversal shear stress ($\overline{\tau}_{xz}$) as a function of modulus ratio (E_c/E_m) of an FGM plate for various values of power law index (n)

4.2.4. Variation of Stresses in Through-the-Thickness

Figures 20 - 24 show the variation of in-plane longitudinal stress ($\overline{\sigma}_x$), in-plane normal stress ($\overline{\sigma}_y$), longitudinal shear stress ($\overline{\tau}_{xy}$) and transversal shear stresses ($\overline{\tau}_{yz}$, $\overline{\tau}_{xz}$), respectively in the FGM plate under the sinusoidal load, for different values of power-law index values. As exhibited in Figure 20 and Figure 21, the in-plane longitudinal stress ($\overline{\sigma}_x$), in-plane normal stress ($\overline{\sigma}_y$), are compressive throughout the plate up to $\overline{z} \cong 0.157$ and then become tensile afterwards. The maximum tensile stresses occur at the top surface of the plate and maximum compressive stresses occur at a point on the bottom of the plate.

Figures 22 - 24 depict the through-the-thickness distributions of the shear stresses ($\overline{\tau}_{xy}$ $\overline{\tau}_{xy}$, $\overline{\tau}_{xy}$) in the FGM plate under sinusoidal load for different volume fraction exponents. The distinction among the curves is obvious. As the strain gradients increase, the inhomogeneities play a greater role in stress distribution calculations. The through-the-thickness distributions are not parabolic and it is to be noticed that the maximum shear stress value occurs at $\overline{z}$ =0.2 for volume fraction exponent, n=2, not at the plate center as in the case of homogeneous case.
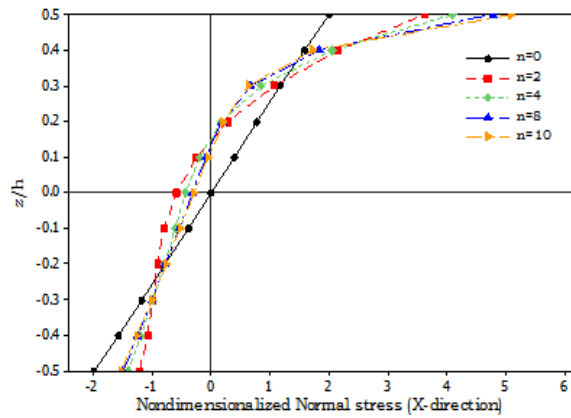
Figure 20: Variation of in-plane longitudinal stress ($\overline{\sigma}_x$) across the thickness of an FGM plate for different power-law index, n
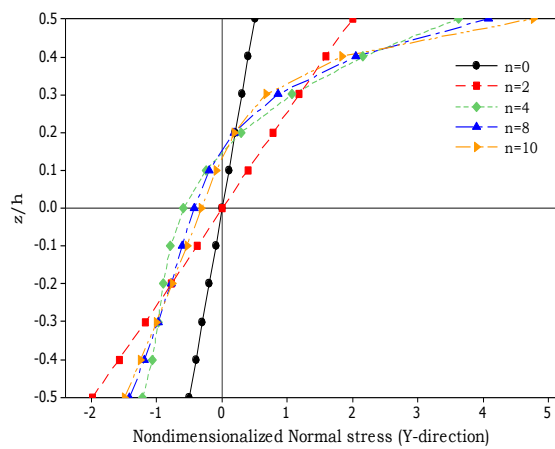

Figure 22:Variation of longitudinal shear stress ($\overline{\tau}_{xy}$) across the thickness of an FGM plate for different power-law index, n

Figure 21:Variation of in-plane normal stress ($\overline{\sigma}_y$) across the thickness of an FGM plate for different power-law index,n
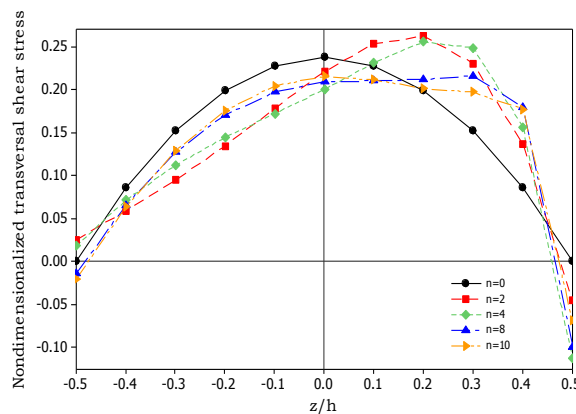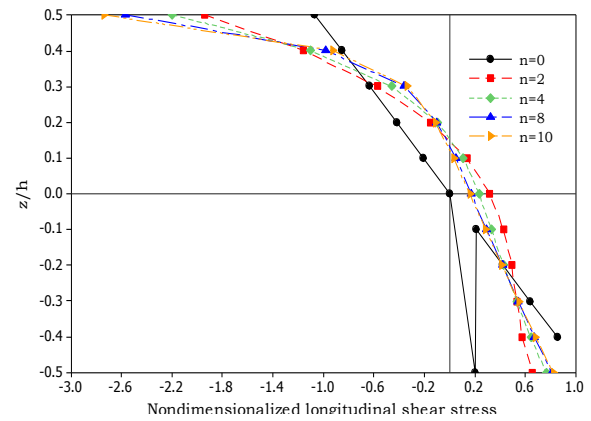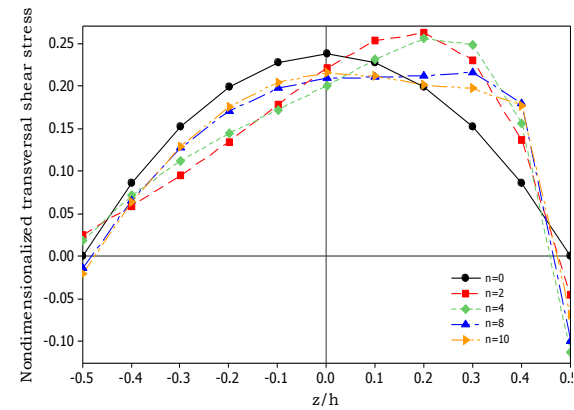

Figure 23:Variation of transversal shear stress ($\overline{\tau}_{yz}$) across the thickness of an FGM plate for different power-law index, n

Conclusions

A higher-order shear deformation theory was successfully developed for static bending behavior of simply supported functionally graded plates without enforcing zero transverse shear stresses on the top and bottom surfaces of the plate. This eliminated the need of shear correction factors. The material properties are assumed to vary according to power law distribution. The governing equations and boundary conditions are derived by employing the principle of virtual work. The governing equations are solved using Navier's type closed form solution, for FG plates subjected to sinusoidal load. Comparative studies are performed to demonstrate the accuracy and efficiency of the present theory. The gradients or inhomogeneities in materials play a vital role in determining the bending response of functionally graded material plates. The variation of material properties in the thickness direction can eliminate interface problems and thus the stress distributions are smooth. The analytical formulations and solutions presented herein should be useful in further studies and should provide engineers with the capability for the design of functionally graded material plates for advanced technical applications. Also, the present findings will be a useful benchmark for evaluating the other future plate theories and numerical methods, such as the finite element and meshless methods.

Figure 24:Variation of transversal shear stress ($\overline{\tau}_{xz}$) across the thickness of an FGM plate for different power-law index, n

References

[1] S.S. Vel, and R.C. Batra, "Exact solutions for thermoelastic deformations of functionally graded thick rectangular plates". *AIAA J*, Vol. **40** (2002) 1421-1433.

[2] E. Reissner and Y.Stavsk, "Bending and stretching of certain types of heterogeneous aelotropic elastic plates". *ASME J ApplMech*, Vol. 28 (1961) 402-428.

[3] E. Reissner,"The effect of transverse shear deformation on the bending of elastic plates". *ASME J ApplMech*, Vol. **12 (1945) No. 2**, 69-77.

[4] R. D Mindlin," Influence of rotary inertia and shear on flexural motions of isotropic, elastic plates". *ASME J ApplMech*, Vol. **18** (1951) 31-38.

[5] Huu-Tai Thai and ThucP.Vo, "A new sinusoidal shear deformation theory for bending, buckling, and vibration of functionally graded paltes". *Appl Math Model,*Vol. **37** (2013) 3269-3281.

[6] J.N. Reddy and C.D. Chin, "Thermomechanical analysis of functionally graded cylinders and plates". J Therm stress, Vol. 21(1998) No.6, 593-626.

[7] A.M. Zenkour, "A comprehensive analysis of functionally graded sandwich plates:Part-1-Deflection and stresses". Int J Solids Struct, Vol. 42(2005) No. 18-19, 5224-5242.

[8] A.M. Zenkour, "A comprehensive analysis of functionally graded sandwich plates:Part-2-Buckling and free vibration". Int J Solids Struct, Vol. 42 (2005) No. 18-19, 5243-5258.

[9] A.M. Zenkour"Generalized shear deformation theory for bending analysis of functionally graded plates". Appl Math Model,Vol. 30 (2006) No. 1, 67-84.

[10] T. Kant, D.R.J.Owen, and O. C Zienkiewicz,"A refined higher order C0 plate element". Computstruct, Vol. 15 (1982) No. 2, 177-183.

[11] B.N.Pandya, and T. Kant, "Higher-order shear deformable theories for flexure of sandwich plates-finite element evaluations". Int J solids Struct, Vol. 24 (1988) No. 12, 1267-1286.

[12] B.N.Pandya, and T. Kant, "Finite element analysis of laminated composite plates using a higher order displacement model". Compos SciTechnol,Vol. 32, (1988) No. 2, 137-155.

[13] T. Kant, and K. Swaminathan, "Analytical solutions for the static analysis of laminated composite and sandwich plates based on higher order refined theory". Composite struct, Vol. 56 (2002) No. 4, 329-344.

[14] T. Kant, and K. Swaminathan, "Analytical solutions for free vibration analysis of laminated composite and sandwich plates based on higher order refined theory". compositestruct, Vol. 53 (2001) No. 1, 73-85.

[15] Garg Ajay Kumar, KhareRakesh Kumar, Kant Tarun, "Higher order closed form solutions for free vibration of laminated composite and sandwich shells. J Sandwich struct Mater, Vol. 8 (2006) No. 3, 205-235.

[16] M. E. Golmakani, and M. Kadkhodayan, " Nonlinear bending analysis of annular FGM plates using higher order shear deformation plate theories". Composite struct,Vol. 93 (2011) 973-982.

[17] Hiroyuki Matsunaga, " Free vibration and stability of functionally graded plates according to a 2-D higher-order deformation theory". Composite struct, Vol. 82 (2008) 499-512.

[18] Hiroyuki Matsunaga, "Stress analysis of functionally graded plates subjected to thermal and mechanical loadings". Composite struct, Vol. 87 (2009) 344-357.

[19] Song Xiang and Gui-wen Kang, "A nth-order shear deformation theory for the bending analysis on the functionally graded plates". European Journal of Mechanics A/Solids,Vol. 37 (2013) 336-343.

[20] A.M.A. Neves, A.J.M. Ferreira, E.Carrera, M.Cinefra, C.M.C.Roque, R.M.N.Jorge, and C.M.M. Soares, "Free vibration analysis of functionally graded shells by a higher-order shear deformation theory and radial basis functions collocation, accounting for through-the-thickness deformations". European Journal of Mechanics A/Solids, Vol. 37 (2013) 24-34.

[21] J.N.Reddy, "A review of refined theories of laminated composite plates", Shock, Vib. Dig. Vol. 22 (199) 3-17.

[22] M. Mallikarjuna, T. Kant, "A Critical review and some results of recently developed refined theories of fibre reinforced laminated composites and sandwiches". Compos. Struct,Vol. 23 (1993) 293-312.

[23] L. Dahsin, L. Xiaoyu, "An overall view of laminate theories based on displacement hypothesis". J Composite materials,Vol.30 (1996) 1539-1561.

[24] A.M.A. Neves, A.J.M. Ferreira, E.Carrera, M.Cinefra, C.M.C.Roque ,, R.M.N. Jorge, and C.M.M. Soares, "Static, free vibration and buckling analysis of isotropic and sandwich functionally graded plates using a quasi-3D higher-order shear deformation theory and meshless technique". Compos: Part B, Vol. 44 (2013) 657-674.

[25] Mechab, Ismail.H.A. Atmane, HA.Belhadejand E.A. A. Bedia, "A two variable refined plate theory for the bending analysis of functionally graded plates". Act Mech Sin,Vol. 26 (2010) 941-949.

[26] J.L.Mantari and C.GuedesSoares, "A novel higher-order shear deformation theory with stretching effect for functionally graded plates". Composites: Part B, Vol. 45 (2013) 268-281.

[27] M.Touratier, "An efficient standard plate theory", Int. J. Eng. Sci. Vol. 29 (1991) 901-916.

[28] Victor Birman and Larry W. Byrd, "Modeling and Analysis of Functionally Graded Materials and Structures", Applied Mechanics Reviews, Vol. 60 (2007) September, 195-216.

[29] J. N. Reddy, "Analysis of functionally graded plates". International Journal for Numerical Methods in Engineering, Vol. 47 (2000) issue 1-3, 663-684.

[30] Z-Q. CHENG and R. C. BATRA, "Deflection relationships between the homogeneous Kirchhoff plate theory and different functionally graded plate theories". Arch. Mech, Vol. 52 (2000) No.1, 143-158.

[31] Z-Q. Cheng, R. C. Batra, "Exact correspondence between eigenvalues of membranes and functionally graded simply supported polygonal plates". Journal of Sound and vibration, Vol. 229 (2000) No.4, 879-895.

[32] Z.-Q. Cheng, R.C. Batra, "Three-dimensional thermoelastic deformations of a functionally graded elliptic plate, Composites: Part B". Vol. 31 (2000) 97–106.

[33] M Michael. Gasik, Baosheng Zhang, Omer Van der Biest, Jozef Vleugels, Guy Anné, Stijn Put, "Design and Fabrication of Symmetric FGM Plates". Materials Science Forum, Vols. 23-28 (2003) 423-425.

[34] Batra and B. M. Love, "Adiabatic shear bands in functionally, Graded materials". Journal of Thermal Stresses, Vol. 27 (2004) 1101-1123.

[35] L. F. Qian, R. C. Batra, L. M. Chen, "Analysis of cylindrical bending thermoelastic deformations of functionally graded plates by a meshless local Petrov–Galerkin method". Computational Mechanics, Vol. 33 (2004) 263–273.

[36] D.F. Gilhooley, R.C. Batra, J.R. Xiao , M.A. McCarthy, J.W. Gillespie Jr, "Analysis of thick functionally graded plates by using higher-order shear and normal deformable plate theory and MLPG method with radial basis functions". Composite Structures, Vol. 80 (2007) 539–552.

[37] Mohammad Talha and B N Singh, "Thermo-mechanical deformation behavior of functionally graded rectangular plates subjected to various boundary conditions and loadings". International Journal of Aerospace and Mechanical Engineering, Vol. 6 (2012) No.1, 14-25.

[38] Tahar Hassaine Daouadji AbdelazizHadj Henni, Abdelouahed Tounsi, and Adda Bedia El Abbes, "A New Hyperbolic Shear Deformation Theory for Bending Analysis of Functionally Graded Plates", Hindawi Publishing Corporation, Modelling and Simulation in Engineering, Vol. 2012, 1-10, doi:10.1155/2012/159806.

[39] Song Xiang, Gui-wen Kang, "A nth-order shear deformation theory for the bending analysis on the functionally graded plates". European Journal of Mechanics A/Solids, Vol. 37 (2013) 336-343.

[40] S. Suresh, A. Mortensen, "Fundamentals of functionally graded materials". 1st ed. London: IOM Communications; 1998.

[41] B.N. Pandya and T. Kant, "Finite element stress analysis of laminated composite plates using higher order displacement model". Compos Sci Technol, Vol. 32 (1988) 137–55.

[42] J.N. Reddy, "Energy principles and variational methods in applied mechanics". John Wiley & Sons Inc; 2002.

Dynamic Analysis and Design of Steel-Ball Grinding Machines Based on No-Slip Cases

Jingjun Zhang *, Guoguang Li, Ruizhen Gao, Bin Yan, Huimin Xue

Hebei University of Engineering, Handan, China 056038

Abstract

Based on no-slip cases between steel balls and lapping discs while a horizontal grinding machine is working, the motion equations of the ball lapping are established and the law of motion is revealed by the MATLAB software. This paper shows that the difference of the trace spacing is reduced by increasing the disc diameter, which can make the trace distribution of the steel ball surface more uniform. In order that balls do not slip when rotary disc drives them to rotate, the ranges of the lapping pressure and lapping disc speed is deduced by using the dynamics analysis considering from the vertical trench surface and along the groove surface, respectively. Finally, this paper takes the selected material as an example to analyze the process parameters that affect the lapping curves, and explains the selection principles of alpha and beta when the trench has some bias, which can provide a reference to improve the quality of the steel balls surface.

1. Introduction

Bearings are one kind of vital parts of modern machinery and equipment. They are widely used in many industries. Their main function is to support the mechanical rotating body and reduce the coefficient of load friction in the transmission process. As shown in Figure 1, steel balls are important component of ball bearings, which processing technology has unique specialized characteristics and the processing quality will largely affect the life and reliability of the ball bearings [1-3].

Figure 1. Ball bearing

Lapping is the last step in steel balls processing technology. In the meantime, steel ball-billets are squeezed, scraped by lapping discs and abrasive, which can remove the machining allowance of the ball surface and improve steel balls sphericity as well as reduce the roughness of the surface [4, 5]. The sphericity is a main technical index of steel balls and it has a great impact on bearing performance (such as accuracy, noise, vibration, etc.) [6-8]. About lapping, the conventional view is that rotary disc drives steel balls revolution around the disc axis, and the linear velocity difference of the arc between the spherical surface and groove makes balls rotation. The revolution and rotation complete the lapping of steel balls together [9]. This interpretation is relatively simple because the revolution speed is much greater than the speed of the rotation, which will make balls become ellipsoid in the lapping process. Zhu [10] proposed that the lapping disc grinds along the three circles on the steel ball surface repetitively through the contact points under the lapping method of two discs along a coaxial. It has been proved that the lapping trajectory is a trace circle rounding an axis of the ball center when a steel ball is in motion.

This paper presents the motion equations of the lapping model without slipping, and the angular velocity of rotation, angular velocity of revolution as well as angle of deflection are calculated by using the MATLAB software. Based on the analysis of the trace distribution of the steel ball surface, it is shown that reducing the difference of two trace circles can make the trace distribution of the steel ball surface more uniform. In order for the balls not to slip when the rotary disc drives them to rotate, the ranges of the lapping pressure and lapping disc speed are deduced by using the dynamics analysis considering from the vertical

---
* Corresponding author. e-mail: santt88@163.com.

trench surface and along the groove surface, respectively. Finally, this paper takes the lapping disc material HT300, steel balls material GCr15 as an example to analyze the fact that process parameters affect the apping curves, and explains the selection principles of alpha and beta when the trench has some bias, which can provide a reference to improve the quality of the steel balls surface.
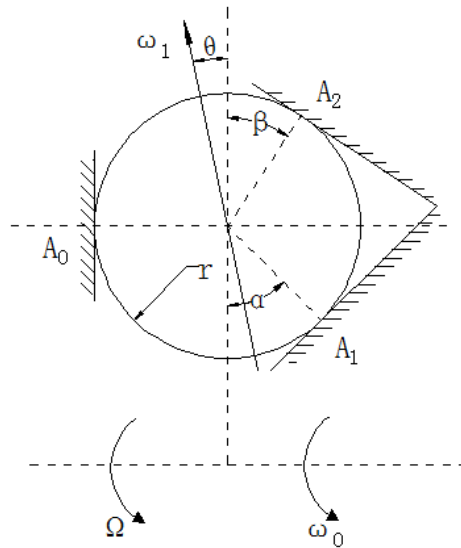
2. Dynamic Analysis of Ball Lapping

2.1. Motion Equation

Figure 2. The motion analysis of a steel ball
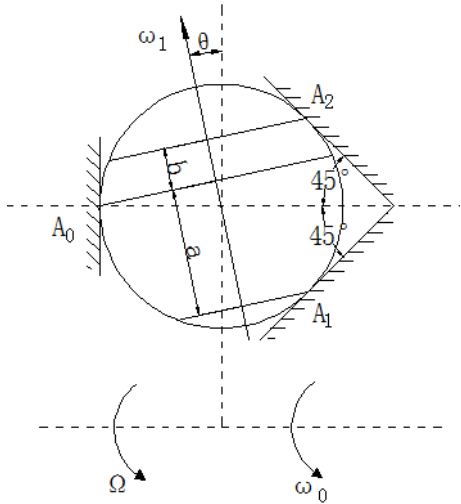
Figure 3. The trace distribution of lapping

Balls and lapping discs are regarded as rigid bodies when a horizontal grinding machine is working and the contacts between them are idealized as point contacts. As shown in Figure 2, A_0, A_1 , A_2 are three contact points between balls and lapping discs, the revolution radius of the balls are R_0, R_1, R_2. The motion of balls in the groove can be divided into ω_0 that revolves around the center of discs and ω_1 that rotates around its own sphere center. Generally, the rotation ω_1 can also be decomposed into pivot motion and roll motion [11]. Without considering the contact deformation and applying the general principle of

rigid bodies, the equations of lapping motion without slipping at three contact points is expressed as follows:

$$\begin{cases} \omega_0 R_0 + \omega_1 r \cos\theta = \Omega R_0 \\ \omega_0 R_1 - \omega_1 r \sin(\alpha - \theta) = 0 \\ \omega_0 R_2 - \omega_1 r \sin(\beta + \theta) = 0 \end{cases} \quad (1)$$

where Ω denotes the angular speed of rotary disc, θ is the angle of deflection, and r is the radius of steel ball.
Lapping parameters are calculated, respectively, as:

$$\begin{cases} \tan\theta = \dfrac{-R_1 \sin\beta + R_2 \sin\alpha}{R_1 \cos\beta + R_2 \cos\alpha} \\ \omega_0 = \dfrac{R_0 \sin(\alpha+\beta)\Omega}{R_0 \sin(\alpha+\beta) + R_1 \cos\beta + R_2 \cos\alpha} \\ \omega_1 = \dfrac{R_0 R_2 \Omega}{r\left[R_0 \sin(\beta+\theta) + R_2 \cos\theta\right]} \end{cases} \quad (2)$$

In which $R_1 = R_0 - r\cos\alpha$, $R_2 = R_0 + r\cos\beta$.
The above formulae provide the no slipping laws of lapping motion. When the position of steel balls in the groove and the speed of rotary disk are determined, θ, ω_0 and ω_1 will have a unique solution, which means the motion can be uniquely identified. It also shows that ω_0, ω_1 are proportional to Ω. Since θ is generally not equal to 0, ω_1 will have a normal component and a tangential component. The corresponding movement of normal component and tangential component take a part mainly in grinding steel balls and rolling steel balls, respectively. The lapping of steel balls is implemented by the movements together.

2.2. Structure Optimization of Lapping Disc

There exists the angle of deflection θ remaining unchanged when the trench truncate $\alpha=\beta=45^0$ is taken into consideration. In the same circulation with different rotational loops, the lapping traces are three circles around the axis of rotation. The final machining is completed by using the repeated lapping.
As shown in Figure 3, the distance among three traces are a and b, which can be expressed as:

$$\begin{cases} a = r \cos(45^\circ - \theta) + r \sin\theta \\ b = r\cos(45^\circ + \theta) - r \sin\theta \\ \tan\theta = \dfrac{-R_1 + R_2}{R_1 + R_2} \end{cases} \quad (3)$$

From the above formulae, we can get

$$\frac{a}{b} = \frac{(1+\sqrt{2})\dfrac{r}{R_0} + \sqrt{2}}{-(1+\sqrt{2})\dfrac{r}{R_0} + \sqrt{2}} \quad (4)$$

There are three trace circles on the surface of steel balls, where A_0 is in the middle of A_1 and A_2. It can be seen from Eq. (4) that the interval ratio of trace circles are only relevant to r/R_0, and the relation curve of which is shown in Figure 4. It is showed by tests that the value of a/b influences the lapping balls quality and efficiency, and

the accuracy of balls surface will be improved when the value is close to 1 [12].
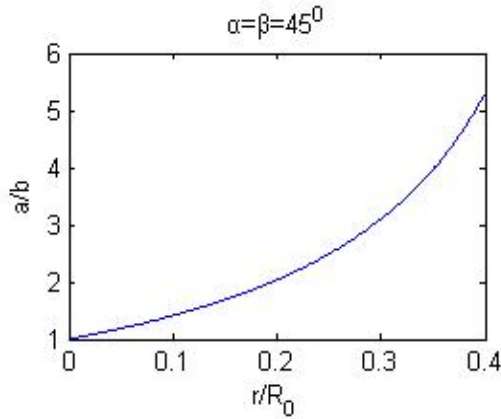

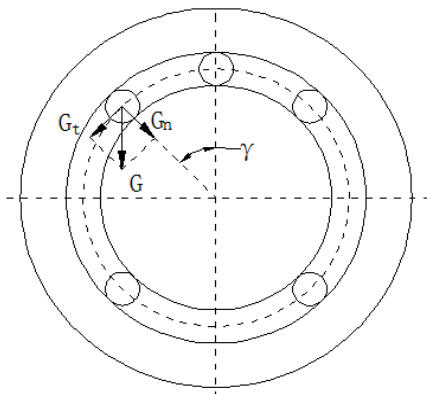**Figure 4**. The curve of r/R_0-a/b

Figure 5. The gravity decomposition of steel balls

When the ordinate is equal to 1, the abscissa will be close to 0 infinitely, which means that the radius of the revolution is much larger than the ball radius. The abscissa of outside groove can be reduced by increasing the disc diameter, and the quality of balls surface can be improved. However, there are some problems when increasing the diameter. The linear velocities inside and outside the groove will inevitably lead to a great difference, which means that it cannot make all balls get in and out of the groove smoothly at the same time, and then the steel ball surface will be destroyed. Thus, it is essential to consider the above two aspects when the value of r/R_0 is selected.

3. Dynamic Analysis of Lapping Ball

Figure 5 presents the ball distribution in the same trench for horizontal lapping machine. Supposing the weight of a single ball is G, the components of four quadrants are calculated as:

$$\begin{cases} G_n = G\cos\gamma \\ G_t = -G\sin\gamma \end{cases}, \quad \begin{cases} G_n = G\cos\gamma \\ G_t = G\sin\gamma \end{cases}$$

$$\begin{cases} G_n = -G\cos\gamma \\ G_t = G\sin\gamma \end{cases}, \quad \begin{cases} G_n = -G\cos\gamma \\ G_t = -G\sin\gamma \end{cases} \tag{5}$$

3.1. Dynamic Equation of the Vertical Trench Surface

Without taking into account the ball interaction and the impact of lapping fluid, a single steel ball without slipping is chosen to be the research object. In order for the balls not to slip in all directions, the vertical trench surface and along the groove surface are analyzed, respectively, as shown in Figure 6 and Figure 7.
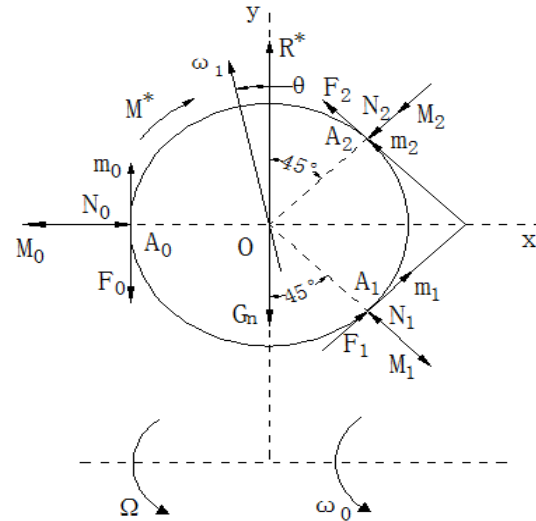

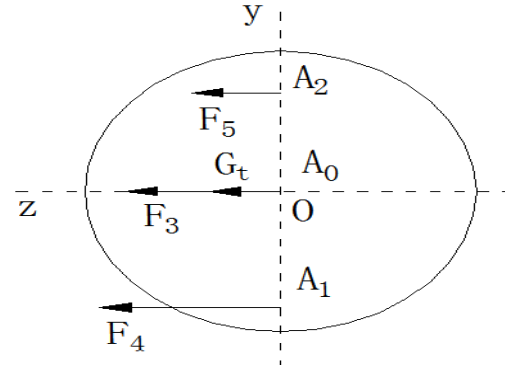**Figure 6.** The stress analysis of the vertical trench surface

Figure 7. The stress analysis along the groove surface

In case that steel balls are not allowed to slip around the direction of z-axis in the V-shaped groove, the conditions that the dynamic equation has to satisfy are as follows:

$$\sum F_x = 0, \quad \sum F_y = 0, \quad \sum M_z(F) = 0 \tag{6}$$

It can be also written in the form as follows:

$$\begin{cases} N_0 - N_1\sin 45° - N_2\sin 45° + F_1\cos 45° - F_2\cos 45° = 0 \\ N_1\sin 45° - N_2\sin 45° + R^* - F_0 - G_n + F_1\cos 45° + F_2\cos 45° = 0 \\ (F_0 + F_1 + F_2)*r - M^* = 0 \end{cases} \tag{7}$$

Where N_0, N_1, N_2 represent the pressures at three contact points, F_0, F_1, F_2 denote the forces of the sliding friction at three contact points, R^* and M^* are the inertia force and couple of a ball, respectively.

Suppose that the critical pressures of three contact points are $[N_0]$, $[N_1]$, $[N_2]$, and the critical forces of the sliding friction are $[F_0]$, $[F_1]$, $[F_2]$, respectively, their relation can be expressed as follows:

$$[F_0]=f[N_0], \quad [F_1]=f[N_1], \quad [F_2]=f[N_2] \tag{8}$$

Combining Eqs.(7) and (8), it can be obtained as

$$\begin{cases} [N_0]=\dfrac{(-2+\sqrt{2})}{2}\left[\dfrac{-2R^*f}{1+f^2}+\dfrac{2G_nf}{1+f^2}-\dfrac{\sqrt{2}M^*}{rf}\right] \\[2mm] [N_1]=\dfrac{(-2+\sqrt{2})}{2}\left[\dfrac{(1+\sqrt{2}+f)R^*}{1+f^2}-\dfrac{(1+\sqrt{2}+f)G_n}{1+f^2}-\dfrac{M^*}{rf}\right] \\[2mm] [N_2]=\dfrac{(2-\sqrt{2})}{2}\left[\dfrac{(1+\sqrt{2}-f)R^*}{1+f^2}-\dfrac{(1+\sqrt{2}-f)G_n}{1+f^2}+\dfrac{M^*}{rf}\right] \end{cases} \tag{9}$$

Each of critical pressures contains R^*, G_n and M^*. Generally, R^*, G_n, M^*/r have the same order of magnitude, and the sliding friction coefficients are relatively small. Thus, Eq. (9) can be expressed approximately as:

$$[N_0]=\frac{(\sqrt{2}-1)M^*}{rf}, [N_1]=\frac{(2-\sqrt{2})M^*}{2rf}, [N_2]=\frac{(2-\sqrt{2})M^*}{2rf} \tag{10}$$

To the motion balls, the rotational inertia J and inertia couple M* are calculated as:

$$J=\frac{2}{5}mr^2, \qquad M^*=J\omega_1\times\omega_0 \tag{11}$$

The critical pressures need to less than the actual lapping pressures at three contact points in order not to slip, which can be written as:

$$[N_0]<N_0, \qquad [N_1]<N_1, \qquad [N_2]<N_2 \tag{12}$$

Using Eqs.(10), (11) and (12), the lower limit inequality of N0 can be derived as

$$N_0>\frac{2(\sqrt{2}-1)mr\omega_0\omega_1\cos\theta}{5f} \tag{13}$$

3.2. Dynamic Equation along the Groove Surface

Analogously, to prevent steel balls from slipping around the direction of x-axis and y-axis, the conditions have to be satisfied as follows:

$$\sum F_z=0, \sum M_x(F)=0, \sum M_y(F)=0 \tag{14}$$

Which can be written in the following form:

$$\begin{cases} F_3+F_4+F_5+G_t=0 \\ (-F_4\cos 45^0+F_5\cos 45^0)r+m_x=0 \\ (F_3-F_4\sin 45^0-F_5\sin 45^0)r+m_y=0 \end{cases} \tag{15}$$

where F_3, F_4, F_5 represent the forces of the sliding friction at three contact points, M_0, M_1, M_2 denote the pivot frictional moments at three contact points, m_0, m_1, m_2 are the rolling frictional moments at three contact points, m_x, m_y refer to the algebraic sums of projection that

pivot frictional and rolling frictional moments work on x-axis and y-axis, respectively, and in which

$$m_x=-M_0+(M_1-M_2)\cos 45^0+(m_1-m_2)\cos 45^0$$
$$m_y=-(M_1+M_2)\sin 45^0+m_0+(m_1+m_2)\sin 45^0$$

Because the rolling frictional moment is far less than pivot frictional moment at the contact points, one can wish to omit the rolling frictional moment, which means only to consider the pivot frictional moment. Then the above expressions can be simplified as:

$$m_x=-M_0+(M_1-M_2)\cos 45^0,$$
$$m_y=-(M_1+M_2)\sin 45^0 \tag{16}$$

By Eq. (15) and (16), it can be obtained as:

$$\begin{cases} F_3=\dfrac{(\sqrt{2}-1)(M_1+M_2-rG_t)}{r} \\[2mm] F_4=\dfrac{(2-\sqrt{2})}{2r}\left[-(\sqrt{2}+1)M_0+M_1-(1+\sqrt{2})M_2-rG_t\right] \\[2mm] F_5=\dfrac{\sqrt{2}}{2r}\left[M_0-M_1+(\sqrt{2}-1)M_2+(1-\sqrt{2})rG_t\right] \end{cases} \tag{17}$$

Supposing that the elastic modulus and poisson's ratio of steel balls are E_g, υ_g, the elastic modulus and poisson's ratio of lapping discs are E_y, υ_y. According to the elastic contact theory [13], the pivot frictional moments can be calculated as follows:

$$\begin{cases} M_0=\dfrac{3\pi f}{2}N_0\sqrt[3]{\dfrac{3rN_0}{4}(\dfrac{1-\upsilon_g^2}{E_g}+\dfrac{1-\upsilon_y^2}{E_y})} \\[2mm] M_1=\dfrac{3\pi f}{2}N_1\sqrt[3]{\dfrac{3rN_1}{4}(\dfrac{1-\upsilon_g^2}{E_g}+\dfrac{1-\upsilon_y^2}{E_y})} \\[2mm] M_2=\dfrac{3\pi f}{2}N_2\sqrt[3]{\dfrac{3rN_2}{4}(\dfrac{1-\upsilon_g^2}{E_g}+\dfrac{1-\upsilon_y^2}{E_y})} \end{cases} \tag{18}$$

Analyzing the statics of steel balls in the groove, it can be found that the ratio of lapping pressure is approximately equal to the ratio of critical pressure. Thus, it is reasonable that the relative relation of actual lapping pressure is:

$$N_0:N_1:N_2=\sqrt{2}:1:1 \tag{19}$$

Substituting Eq.(18) and Eq.(19) into Eq.(17), it is obtained as follows

$$\begin{cases} F_3=\dfrac{\sqrt[3]{2}(\sqrt{2}-1)}{r}M_0-(\sqrt{2}-1)G_t \\[2mm] F_4=\dfrac{-(2-\sqrt{2})(\sqrt{2}+1+2^{-\frac{1}{6}})}{2r}M_0-\dfrac{2-\sqrt{2}}{2}G_t \\[2mm] F_5=\dfrac{\sqrt{2}+\sqrt[3]{2}-2^{\frac{5}{6}}}{2r}M_0-\dfrac{2-\sqrt{2}}{2}G_t \end{cases} \tag{20}$$

In the lapping process, the rotary disk has to overcome the pivot frictional moment and rolling frictional moment, and then drives steel balls to rotate. To stop balls from slipping when they are rotated, the conditions that have to be satisfied are as follows

$$|F_3|<N_0 f, \quad |F_4|<N_1 f, \quad |F_5|<N_2 f \qquad (21)$$

From Eq. (20), it can be seen that F_4 is greater than the other two forces of the sliding friction. Selecting F_4 as the represented formula and substituting Eq. (20) into Eq. (21), one obtains

$$\frac{1}{f}[\frac{1+2^{-\frac{1}{6}}(\sqrt{2}-1)}{r}M_0 + (\sqrt{2}-1)G_t] < N_0 \qquad (22)$$

3.3. Selection of the Pressure and Speed

It can be drawn from Eq. (18) that M_0 is proportional to $N_0^{4/3}$, and it is obtained that N_0 is less than a specified value, referred to as B by substituting Eq. (18) into Eq. (22). Similarly, to solve the first and third inequalities of Eq. (21), it can deduce that N_0 is less than A and C, respectively.

Therefore, the following inequality has to be satisfied if lapping balls do not slip in all directions:

$$\frac{2(\sqrt{2}-1)mr\omega_0\omega_1\cos\theta}{5f} < N_0 < \min\{A,B,C\} \qquad (23)$$

Substituting Eq. (2) into Eq. (23) gives that the expression of the lower limit is proportional to Ω^2. Since A, B, C are constant and independent of the rotary disc speed, it can deduce $\Omega<D$, which means D is the maximum allowable speed of the rotary disc.

4. Influencing Parameter

4.1. Process Parameter

When the steel balls rotate without slipping in the groove, the radius of the revolution affects the lapping pressure and the maximum allowable speed. Here select HT300 as the material of lapping discs, GCr15 as the material of steel balls, and 315mm as the revolution radius of R_0.
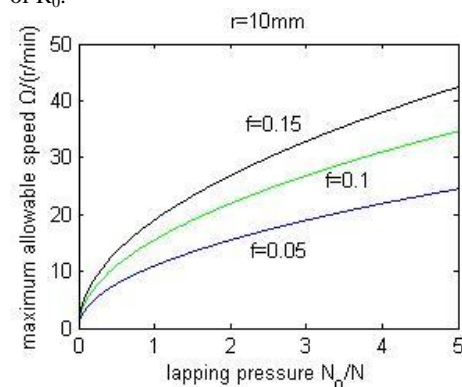

Figure 8. Coefficients of friction that work on lapping curves
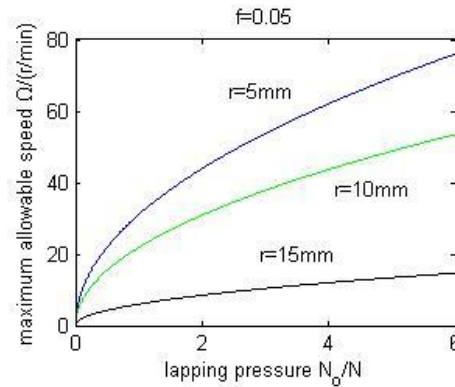

Figure 9. Sizes of balls that work on lapping curves

As shown in Figure 8, it is the relation curve between the lapping pressure and maximum allowable speed. The curve shows that with the increase of the lapping pressure, the maximum allowable speed rises. The maximum allowable speed of the rotary disc can achieve a higher value when the coefficient of the friction increases, which generates that steel balls are less likely to slip in the lapping process. In Figure 9, it can be seen that the maximum allowable speed of the rotary disc decreases while the sizes of the steel balls are increasing, which illustrates that the steel balls will slip easily. The lapping pressure will be increasing and the speed of the rotary disc will be reducing at this moment.

4.2. Trench Bias

There are many factors that affect the surface quality of the ball in the lapping process, such as the groove shape, machine accuracy, mechanical properties of lapping disc, etc. The groove shape is relatively easy to control and change, which can be achieved by changing the parameters α and β. As shown in Figure 10, the normal angular velocity and angular tangential velocity at three points are as follows:

$$\begin{cases} \omega_0^n = \omega_1\sin\theta, \quad \omega_0^t = \omega_1\cos\theta \\ \omega_1^n = \omega_1\cos(\alpha-\theta), \quad \omega_1^t = \omega_1\sin(\alpha-\theta) \\ \omega_2^n = \omega_1\cos(\beta+\theta), \quad \omega_2^t = \omega_1\sin(\beta+\theta) \end{cases} \qquad (24)$$

From the above formulae, it can be seen that the normal component and tangential component are the negative relations, and there exist different lapping conditions at the contact points. In Figure 11, it is the relation curve between α and tanθ, which shows that tanθwill be equal to 0 when α is near to the value of π/4, and at this time the difference of the lapping condition is relatively smaller. Thus, αand βshould comply with the certain principle when the trench is bias. They should be unequal, the difference between them is very small, and their sum is around π/2. It can make the trace circles have a good distribution and improve the efficiency of the ball lapping simultaneously.
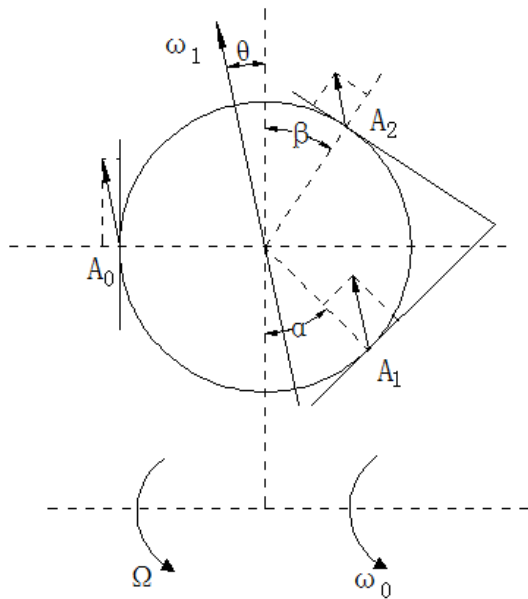
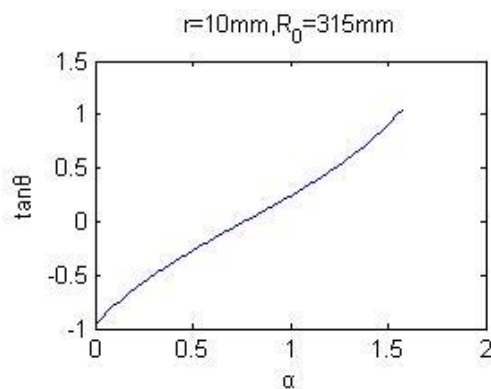**Figure 10.** The relative rotation of three contact points.

Figure 11. The curve of α-tanθ

5. Conclusions

This paper reveals the motion law of grinding balls through establishing the motion equations. Based on the vertical trench surface and along the groove surface, respectively, the dynamics analysis of a single steel ball is achieved and the influence on the quality of the steel ball surface by different parameters is compared. It can be drawn as follows:

(1) The motion law can be uniquely identified when steel balls do not slip in the groove, and the angular velocities of the revolution and rotation are both proportional to the rotational speed of the rotary disc.

(2) When steel balls are ground by a horizontal grinding machine, in order to prevent them from slipping, the lapping pressure has to satisfy a certain range, and the rotary speed of the rotary disc also has to be less than the maximum allowable speed.

(3) The possibility of slip cases can be reduced by increasing the lapping pressure or the coefficient of the friction. Lapping big steel balls are easier to slip than the small ones, and the ways of increasing the lapping pressure and decreasing the rotary speed can solve this problem effectively.

(4) A satisfactory distribution of trace circles can be achieved if the difference between αand β is not big as well as their sum is approximatively equal to 90^0. It will provide a better foundation for the further research.

Acknowledgments

References

[1] Y.Q.Zhang, Z.Y.Wu, "The status quo and development trend of China steel balls processing equipment". Bearing, (2011)No. 4, 59-62 (in Chinese).

[2] J.L.Zhou, J.C.Chen, G.Q.Wu, X.Y.Chen, "Effect of test rig structure parameters on contact stress of specimen". Engineering Mechanics, Vol. 28(2011)No. 6, 226-230(in Chinese).

[3] T.H.C.Childs, S.Mahmood, H.J.Yoon, "Magnetic fluid lapping of ceramic balls". Tribology International, Vol. 28(1995)No. 6, 341-348.

[4] X.L. Liu, "Super lapping of steel ball and whet liquid". Journal of Harbin Bearing, Vol. 27(2006)No. 1, 32-33(in Chinese).

[5] H. Liang, X.J. Zhao, Y.J. Qiu, "Analysis of the flaking of bearing steel balls in the production process", Bearing, (2008)No. 8, 26-27(in Chinese).

[6] H.Ohta, K.Kobayashi, "Vibrations of hybrid ceramic ball bearings". Journal of Sound and Vibration, Vol. 192(1996)No. 2, 481-493.

[7] B.W.Huang, H.K.Kung, "Variations of instability in a rotating spindle system with various bearings". International Journal of Mechanical Sciences, (2003)No. 45, 57-72.

[8] T.M. Banda, "Sound and Vibration in Rolling Bearings". Motion & Control, (1999)No. 6, 29-37.

[9] L.F. Nie, X.J. Zhao, "The conditions that process into round ball and explore the influencing factors, Bearing". (2001)No. 1, 16-18(in Chinese).

[10] C. Zhu, "Mechanical analysis of the two kinds of ball lapping method". Bearing, (2000)No. 9, 11-13(in Chinese).

[11] Z. Xue, C.A. Fu, T. Zhang, "Research on mechanism of lapping balls, Journal of Jiangnan University". Vol. 8(2009)No. 4, 439-444(in Chinese).

[12] Xia XT, Ma W, Tancheng Xie, Manufacturing technology of rolling bearing. Beijing: China Machine Press; 2007(in Chinese).

[13] Zhu C, The mechanics principle of lapping ball. Zhengzhou: Henan Science and Technology Press; 1995 (in Chinese).

Optimization of NOx Emission from Soya Biodiesel Fuelled Diesel Engine using Cetane Improver (DTBP)

Patel N. K., Singh R. N. [*]

School of Energy and Environmental Studies, Devi Ahiliya Vishwavidyalaya,
Indore (M P) - India-452001

Abstract

Within the depleting resources of fossil fuels and the increase in their price, in the recent past a lot of interest has been given to the use of plant oil specially the non-edible oil and its ester (biodiesel). Although the use of biodiesel in place of diesel has resulted in much lesser tail pipe emission, a substantial increase of NOx is reported by several researchers. It may be due to low cetane number and fuel radical's formation during the combustion. Literature reported that mixing of an anti-NOx additive, such as di-tert-butyl peroxide (DTBP) in the bio-diesel before feeding to the nozzle, may reduce the NOx concentration in the CI engine emission. Considering this, a study was conducted on single cylinder four stroke diesel engines using blended soya methyl ester (B50) to optimize the NOx emission with the addition of DTBP cetane improver. The engine was first run on petroleum diesel (B0), followed by B50 and combination of B50 and DTBT. A number of combinations, 50% biodiesel (B50) and 50% petroleum diesel along with di-tert-butyl peroxide (DTBT) such as B50/D0.5, B50/D1.0, B50/D1.5, B50/D2.0, B50/D2.5 and B50/D3, were used in this study. For each test, engine performance and emission were measured. The addition of cetane improver could reduce the NOx emission significantly with the penalty of BSFC, CO and unburned hydrocarbon. The addition of DTBP by volumes of 0.5, 1, 1.5, 2, 2.5 and 3% to B50, the NOx reduction was found as 3.57, 5.0, 5.0, 4.29, 4.88 and 4.9%, respectively as compared to B50 without additive. It was also noted that CO and SOx reduce up to 25% and 33.33%, respectively, compared with petroleum diesel when 1% of DTBP is used. Considering the emission parameters, and the cost of the additive, 1% DTBP would give the optimum results for NOx reduction.

© 2014 Jordan Journal of Mechanical and Industrial Engineering. All rights reserved

Nomenclature

AC	Alternate current
BIS	Bureau of Indian Standards
B0	Petroleum diesel
B50	50% Soya biodiesel and 50% petroleum diesel
BSFC	Brake specific fuel consumption
CI	Compression ignition
CO	Carbon monoxide
CO2	Carbon Dioxide
DTBP	di-tert-butyl peroxide
EHN	ethyl-hexyl nitrate
EPA	Environmental protection agency
HC	Hydro carbon
KVA	Kilo volt ampere
kWh	Kilo Watts hour
NREL	National renewable energy laboratory
NOx	Nitrous oxides
PM	Particulate matter
SOx	Sulfur oxides

1. Introduction

The rapid depletion of petroleum reserves and rising oil prices have led to the search for alternative fuels. The methyl esters of vegetable oils, known as biodiesel, are becoming increasingly popular because of their low environmental impact and potential as a green alternative fuel for diesel engines and they would not require a significant modification of existing engine hardware [1]. Many researchers have suggested the biodiesel as a replacement, either completely or partially blended, because they reduce the tail pipe emissions. Biodiesel by weight contains less carbon, sulphur, water and more oxygen than the petroleum diesel [2]. Numerous studies have shown that with the decrease of carbon monoxide (CO), carbon dioxide (CO_2), particulate matter, sulphur compounds (SOx), volatile organic compound and unburned hydrocarbons, the NOx emissions are increasing [3]. Thermal, prompt, fuel NOx and Nitrous Oxide (N_2O) pathways are the common cause for the formation of NOx emissions during combustion [4]. Thermal NOx is formed by the oxidation of atmospheric nitrogen at elevated

---

[*] Corresponding author. e-mail: rnsingh7@yahoo.com.

temperature (above 1700˚K), and prompt NOx by the formation of free radicals in the flame front of hydrocarbon flames. It is believed that the NOx formation is mainly due to thermal (Zeldovich mechanism) and prompt or Fennimore mechanism [5]. However, in biodiesel, a significant amount of NOx is formed due the prompt or Fennimore mechanism (<1000˚K) [6].

The cetane index is the basic properties of both diesel and biodiesel; it is the measure of ignition performance of the fuel. This parameter is influenced by structural features of fatty acid alkyl esters, such as chain length, degree of un-saturation and branching of the chain. It should be emphasized that the higher the cetane index, the better the combustion will be, improving the engine motor efficiency. Usually, the cetane number increases, with the increasing chain length and decreases with the increasing un-saturation. Residual methanol in biodiesel is responsible for a decrease in the cetane number. The cetane number of biodiesel is always more than 47, which is higher than the petroleum diesel [7]. Researcher reported that cetane index of biodiesel is about 60, whereas that of the diesel is around 42. It should be emphasized that the higher the cetane index, the better the combustion will be, improving the engine motor efficiency. Biodiesel contains about 10–11% inbuilt oxygen by weight, which can lead to a more complete combustion than hydrocarbon based diesel in an engine and high cetane number reduces the ignition delay of the fuel. As biodiesel is completely miscible with diesel, the blending of both fuels in any proportion is possible and recommended in order to improve its qualities. However, the differences in chemical nature of biodiesel and petroleum diesel may cause differences in the physicochemical properties, affecting engine performance and pollutant emissions [3]. Thus, the quality control of biodiesel blends should be monitored in several aspects.

The National Renewable Energy Laboratory (NREL) reported that cetane improvers, like di-tert-butyl peroxide (DTBP) and ethyl-hexyl nitrate (EHN), are effective for reducing NOx by 4% in B20 blends [6]. In this study, the B50 (50% Soya biodiesel and 50% petroleum diesel) test fuel is taken. Because it is reported that as the concentration of Soya methyl ester (biodiesel) increases the NOx emission get increased drastically [7]. Moreover, for a lower concentration of biodiesel (B30 & B20) along di-tert-butyl peroxide applications, NOx emissions results are available [8]; however, for higher concentration, literature is silent.

2. Materials & Methods

2.1. Biodiesel production

The soya oil, procured from open market, was used for the production of biodiesel. Environmental Protection Agency (EPA) suggested that soya methyl ester (SME) produces 2% more NOx and 10%, 20% and 10% less CO, HC & PM, respectively as compared to biodiesel obtained from other oil [9]. The biodiesel is extracted by the alkaline catalyst method because it gives the maximum recovery of biodiesel. The method suggested by Gupta was used for production of biodiesel [10].

2.2. Preparation of B50 and DTBP Mixture

B50 was prepared by blending of 50% biodiesel and 50% petroleum diesel with continuous stirring. Latter DTBP was added in B50 at the rate of 0.5, 1, 1.5, 2, 2.5 & 3% by volume. The mixtures were designated as B50D0.5, B50D1.0, B50D1.5, B50D2.0, B50D2.5, and B50D3.0 respectively.

2.3. Properties of liquid Mixture

The method suggested by Sangha et al. [11] was used for estimation of kinetic viscosity and density of petroleum diesel, B50 and B50-DTBP mixture; however flash points and fire points were measured using Fire & flash point apparatus. Results are tabulated in Table 1.

Table 1. Test fuel properties

Test fuel Properties	Density (kg/m³)	Fire point (°C)	Flash point (°C)	Kinematic viscosity at 40°C (mm²/ sec)
Diesel	862.9	76	73	3.06
B50	870.3	60	57	4.75
B50/D0.5	871.1	59	55	4.78
B50/D1.0	872.4	59	54	4.79
B50/D1.5	873.1	58	53	4.82
B50/D2.0	875.2	57	51	4.85
B50/D2.5	876.6	56	49	4.87
B50/D3.0	877.0	54	47	4.90

2.4. Experimental Setup and Measurement Device

A 7.5 kWh Kirloskar engine, as per specifications given in Table 3, and coupled with a single phase AC generator (7.5 kVA) was used. Performance parameters planned to be studied include: fuel consumption rate, operating efficiency at fixed load and different mixture of fuel, engine exhaust temperature and emissions. The fuel flow rate was measured on a volumetric basis. Speed of engine was maintained constant (1500±10) throughout the experiments and monitored with the help of contact type tachometer. An electric heater was used to load the engine; however, a microprocessor based engine exhaust gas analyzer (testo 340) was used for the measurement of emissions level. The tail pipe exhaust gas temperature was measured with the help of temperature sensor of flue gas analyzer. The measuring range and accuracies of flue gas analyzer is shown in Table 2.

Table 2: Measuring ranges and accuracies of flue gas analyzer

Parameter	Measuring range (ppm)	Accuracy
CO	0-10000	±10% of test reading
SO₂	0-5000	±10% of test reading
NO₂	0-500	±5% of test reading
NO	0-3000	±5% of test reading

Depending upon the facility available with Institute, all the experiments were carried at a fixed load (67% of the maximum load). A sampling port was provided in the exhaust pipe for measuring flue gas temperature and to collect flue gas samples. The test was conducted as per BIS Code No.13018 [12]. However, due to limitation of sources/ facility all the parameters as mentioned in BIS Code No.13018 could not be measured

Table 3. Engine specification

Manufacturer	Kirloskar Engines Ltd
Model	DAF 10
Rated Brake Power, bhp/kWh	9.8/7.5
Rated Speed, rpm	1500 (constant rpm)
No. of Cylinder	One
Bore X Stroke	80 X 110 mm
Compression ratio	17.5:1
Lubrication System	Forced Feed
Types of Fuel pump	High pressure mechanical type
Fuel injection pressure	140Pa (900-1099rpm)
	200Pa (1100-1500rpm)
Type of injection nozzle	Pintle
Number of nozzle hole	One
Nozzle hole diameter	0.25 mm
SFC at constant (1500) rpm	251 g/kWh (185 g/bhp-hr)
Starting	Hand start with cranking handle
Fuel injection timing	24 degree BTDC

2.5. Test Condition and Variables

The engine was operated first on petroleum diesel mode, later with B50 and then B50/D0.5, B50/D1, B50/D1.5, B50/D2, B50/D2.5 and finally B50/D3. All the readings were taken once the engine came to an equilibrium condition. Before switching over to next fuel reading, the engine was allowed to run for 10 minutes so that the last test fuel is completely get washed away from the nozzle, fuel pump and fuel filter. The test was repeated three times to verify the output and engine exhaust data. However, the average value is used for further calculation and graphical representation.

3. Results and Discussion

The effects of cetane improver on NOx, CO, SOx emissions of B50-DTBP mixture were systematically investigated. All the pollutant data were controlled within a range of ±5 ppm. Apart from the concentration of pollutants in the exhaust gases, brake specific fuel consumption, brake thermal efficiency and exhaust gas temperature was also measured and recorded. Data obtained at different fuels were compared with the petroleum diesel and B50 (combinations of 50% Soya biodiesel and 50% petroleum diesel).
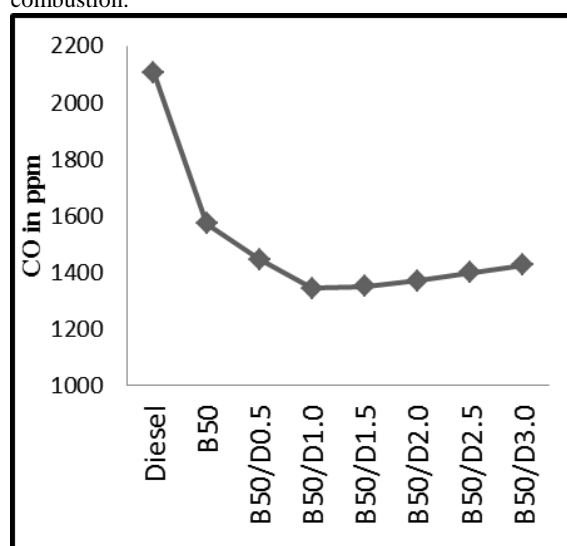
3.1. Effect of DTBP on NOx Emission

It was noted that with the use of B50, the NOx level increases up to 8.45% compared to petroleum diesel. Addition of cetane improver has shown the positive response on reduction of NOx (Figure 1). The critical analysis of Figure 1 indicates that although with the increase of DTBP in B50, NOx concentration is decreased in the tailpipe emission; however, this is not following the uniform trends. The highest decrease of the NOx

concentration (5%) was observed at B50/D1.5 mixture, later it started increasing. It may be because that the additive increases cetane number of the fuel, accelerating ignition. This results in a shorter ignition delay times, high peak in cylinder pressure, temperature, oxygen content [13,14] and responsible for increased NOx emission after 1.5% of DTBP.
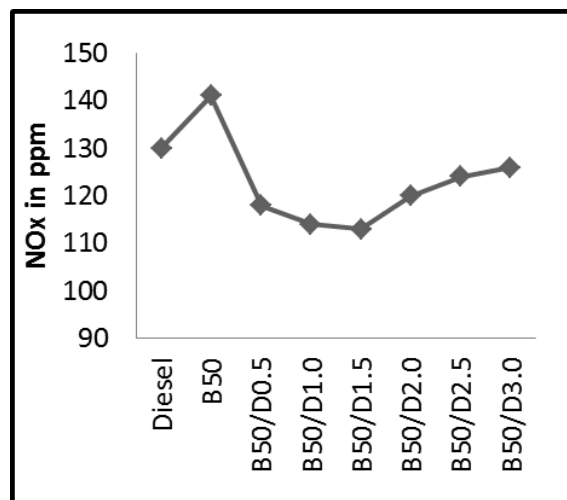
Figure 1. Variations NOx with different fuel

3.2. Effect of DTBP on Carbon Monoxide

It is well proven that the uses of biodiesel in CI engine significantly reduced the CO [4, 7, 10]. B50 reduces the CO concentration in the pollutant about 25% (Figure 2) and addition of DTBT further reduced the CO concentration. This reduction was found highest (>35% as compared to petroleum diesel) at 1% concentration of DTBP in B50. The reduction may be attributed to the chemical structure of the additive ($C_8H_{18}O_2$) having more oxygen in the blended fuel, which might have led to a more complete combustion compared to petroleum diesel combustion.

Figure 2. Variations of CO with different fuel

3.3. Effect of DTBP on Sulphur dioxide

The biodiesel contains a very small amount of sulphur, and the additive used here has no sulphur present in it. Thus, a very small change in SOx emission was observed with different combination of B50 and DTBT (Figure 3).
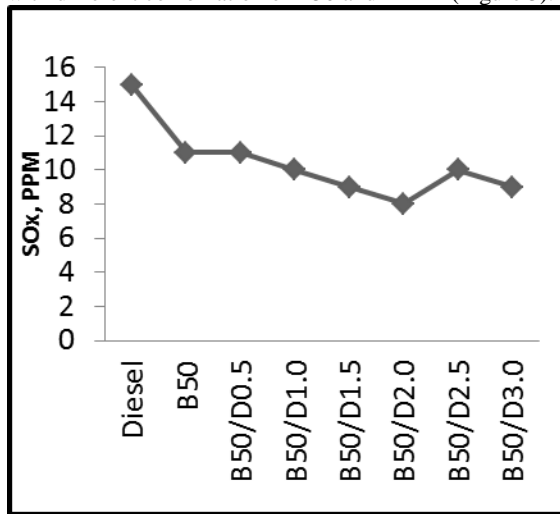

Figure 3. Variation of SOx with different fuel

3.4. Effect of DTBP on Exhaust Gas Temperature

The exhaust gas temperature is the function of combustion temperature and the rate of heat transfer from the tail pipe. Critical analysis of Figure 4 indicates that there is no much effect of DTBT on engine exhaust gas temperature. It varies in the range of 250-300°C (Figure 3). A similar observation was obtained by other researchers while working with biodiesel in CI engine [13, 14,15].
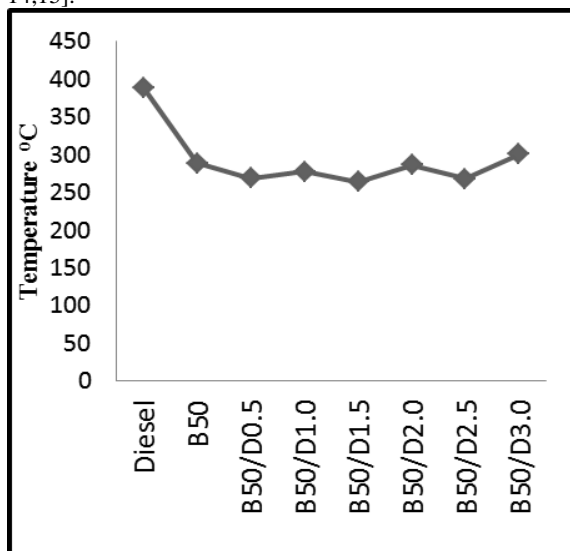

Figure4. Variation of exhaust gas temperature with different fuel

3.5. Effect of DTBP on BSFC and Brake Thermal Efficiency

The biodiesel has a lower calorific value than petroleum diesel. It is because of the lower carbon content and presence of inbuilt oxygen, which results in more BSFC [2,16,17]. Addition of DTBP in B50 shows that BSFC started decreasing with increment of DTBT up to the mixture of B50 and D1.5. At this combination, a higher

brake thermal efficiency was also noted. However, at higher percentage of DTBP, BSFC started increasing (Figure 5). It shows that higher percentage of DTBP might have increased the viscosity of B50 resulted in poor atomization and hence increased the BSFC and started giving poor brake thermal efficiency (Figure 6).
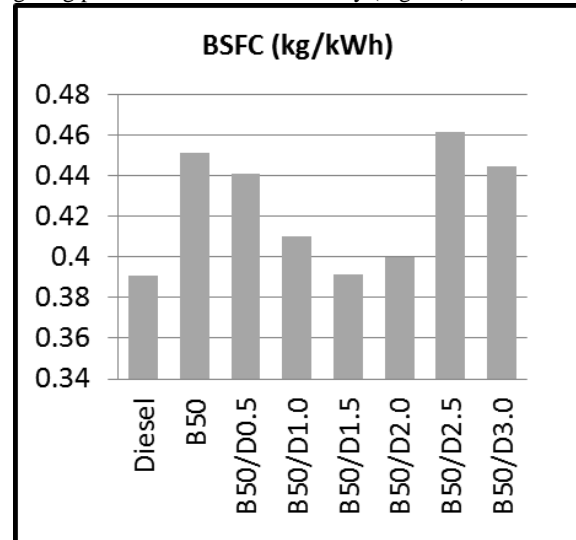

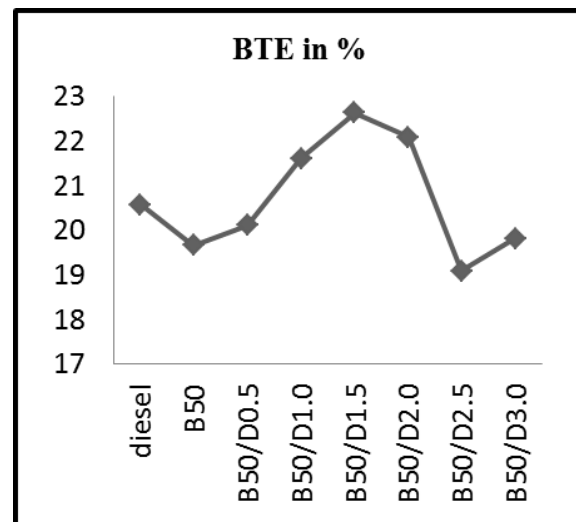**Figure 5**. Variation of BSFC with different fuel

Figure 6. Variation of brake thermal efficiency with different fuel

Since the difference in the NOx concentration at B50/D1 and B50/D1.5 is very small, considering the cost of the additive, 1% mixing of DTBP in B50 is recommended. This study is in line with Nandi *et al.*, whose founding was 0.65% of DTBP will give the best results for B30 [8].

Conclusion

The suitability of the DTBP as a cetane improver additive at higher percentage of biodiesel (50% biodiesel and 50% petroleum diesel) as a CI engine fuel was investigated by looking at the variations of brake specific fuel consumption, brake thermal efficiency, tail pipe emissions such as NOx, SOx, CO and exhaust temperature. It was found that NOx reduced to 5.01% and CO more than 35% at 1% DTBP blending with B50. However, this reduction was 2.32% when compared to

petroleum diesel. Brake thermal efficiency was highest (22.63 %) at 1.5% DTBP and B50 combination among all the tested fuel. However, considering the economic cost of DTBP, 1% addition of DTBP in B50 is recommended.

References

[1] Rao Venkateswara T, G. Prabhakar Rao, and K. Hema Chandra Reddy, "Experimental Investigation of Pongamia, Jatropha and Neem Methyl Esters as Biodiesel on C.I. Engine", Jordan Journal of Mechanical and Industrial Engineering Vol. 2 (2008) No. 2, 117-122.

[2] Singh, R. N. "Investigations on operation of IC engine using producer gas and non-edible plant oils and their esters in duel fuel mode" PhD thesis submitted to Devi Ahilya University, Indore (M P), 2007.

[3] S. K. Jha, S. Femando, S.D. Filip "Flame temperature analysis of biodiesel blends and components. Fuel Vol. 87 (2008) 1982-1988.

[4] U.S. Environmental Protection Agency, "A Comprehensive Analysis of Biodiesel Impacts on Exhaust Emissions: Draft Technical Report", Report No. EPA 420-P02-001, 2002.

[5] C. Fenimore, "Formation of nitric oxide in premixed hydrocarbon flames,'' proc.13th symposium on combustion. The combustion institute, Pittsburgh, PA (1971) 373-380.

[6] R. McCormick, J. Alvarez, and M. Graboski, "NOx solutions for biodiesel," Technical Report No.NREL/SR-510-31465, National Renewable Energy Laboratory, Golden Colorado, 2003.

[7] R. A. Candeia, M.C.D. Silva , J.R. Carvalho Filho , M.G.A. Brasilino , T.C. Bicudo , I.M.G. Santos ,A.G. Souza "Influence of soybean biodiesel content on basic properties of biodiesel–diesel blends", Fuel Vol. 88 (2009) 738–743.

[8] M. Nandi, D. C Jacobs, H. S.; Kesling, F. J. Liotta,; "The Performance of a Peroxide based Cetane improvement Additive in Different Diesels Fuels"; SAE 94201 9, October 1994.

[9] The Environment (Protection) Second Amendment Rules, 2002 (DG Sets) G. S. R. 371(E), [17/5/2002].

[10] Gupta, P.K . Investigations on methyl esters of plant oils as alternative renewable fuel for Compression Ignition engines, unpublished PhD thesis (1994), Dept. of FPM, PAU, Ludhiana (Punjab) India.

[11] M. K. Sangha; P. K. Gupta; V. K. Thaper and S. R. Verma "Storage studies on plant oils and their methyl ester", Agricultural Engineering International Vol. IV (2003) Manuscript 03 005

[12] BIS Code No.13018 "Internal Combustion Engine – method of test for pressure charge engine", 1990.

[13] M.Mofijur, H. H. Masjuki, M. A. Kalam, and M. Shahabuddin , "Experimental study of additive added palm biodiesel in a compression ignition engine", Energy Education Science and Technology Part A: Energy Science and Research Vol. 30 (2013) No. 2, 737-748.

[14] E. Ileri, G. Kocar, "Effects of antioxidant additives on engine performance and exhaust emissions of a diesel engine fuelled with canola oil methyl ester-diesel blend". Energy covers manage Vol. 76 (2012) 145-54.

[15] K. Varatharajan, M. Cheralathan, R. Velraj, "Mitigation of NOx emissions from a jatropha biodiesel fuelled DI diesel engine using antioxidant additives", Fuel 90 (2011) 2721−2725.

[16] M.P. Dorado, E. Ballesteros, J.M. Arnal, J. Gomez and F.J. Lopez, "Exhaust emissions from a diesel engine fueled with transecterified waste olive oil" Fuel B2 (2003) 1311-1315.

[17] Ng Jo-Han, Hoon Kiat Ng and Suyin Ganet "Advances in biodiesel fuel for application in compression ignition engines" Clean Technologies Environmental Policy, Vol. 12(2010) No. 5, 459-493.

Finite Element Analysis of Fully Developed Free Convection Flow Heat and Mass Transfer of a MHD / Micropolar Fluid over a Vertical Channel

Bala Siddulu Malga [*a], Naikoti Kishan[b], V.V Reddy[c], K. Govardhan[a]

[a]Department of Mathematics, GITAM University, Hyderabad, Telangana, India.
[b]Department of Mathematics, University College of Science, O.U, Hyderabad, Telangana, India.
[c]Department of Mathematics, Kamala Nehru Polytechnic College, Hyderabad, Telangana.

Abstract

The present study analyzes the problem of the fully developed natural convection magneto-hydrodynamics micropolar fluid flow of heat and mass transfer in a vertical channel. Asymmetric temperature and convection boundary conditions are applied to the walls of the channel. The cases of double diffusion and Soret-induced connections are both considered. Solutions of the coupled non-linear governing equations are obtained for different values of the buoyancy ratio and various material parameters of the micropolar fluid and magnetic parameters, viscous dissipation. The resulting non-dimensional boundary value problem is solved by the Galerken Finite element method using MATLAB Software. The influence of the governing parameters on the fluid flow as well as heat and solute transfers is demonstrated as significant.

Nomenclature

B	micro-inertia parameter
g	gravitational acceleration
Gr	grashof number
H'	distance between the plates
j	micro inertia per unit mass
K	vortex viscosity parameter
M	magnetic Parameter
N	dimensionless angular velocity
n	dimensionless micro-gyration parameter
R_T	wall temperature
R_S	wall concentration
Ec	Eckert number
Nu	Nusselt Number
C_F	Skin friction coefficient

Greek symbols

μ	dynamic viscosity
φ	buoyancy ratio
ρ	density of fluid
γ	spin-gradient viscosity
κ	vortex viscosity

Subscripts

S	dimensionless Concentration
T	dimensionless temperature
u	dimensionless velocity in x direction
x	dimensionless coordinate axis
y	dimensionless coordinate axis
0	reference state
c	refers to critical conditions

Superscript

$'$	refers to dimensional variable

1. Introduction

The micropolar fluid model introduced by Eringen [1] exhibits some microscopic effects arising from the local structure and micro motion of the fluid elements. Further, the micropolar fluid can sustain couple stresses and include classical Newtonian fluid as a special case. The model of micropolar fluid represents fluids consisting of

---

[*] Corresponding author. email: balumalga@gmail.com

rigid, randomly oriented (or spherical) particles suspended in a viscous medium where the deformation of the particles is ignored. Micropolar fluids have been shown to accurately simulate the flow characteristics of polymeric additives, geomorphological sediments, colloidal suspensions, hematological suspensions, liquid crystals, lubricants, etc. The theory of micropolar fluids, introduced by Eringen [2; 3] in order to deal with the characteristics of fluids with suspended particles, has received a considerable interest in recent years. Also, as demonstrated by Papautsky *et al.* [4], Eringen's model successfully predicts the characteristics of flow in microchannels. An excellent review of the various applications of micropolar fluid mechanics was presented by Ariman *et al.* [5]. The mathematical theory of equations of micropolar fluids and the applications of these fluids in the theory of lubrication and porous media are presented by Lukaszewicz [6]. The heat and mass transfer in micropolar fluids is also important in the context of chemical engineering, aerospace engineering and also industrial manufacturing processes.

The first study of the fully developed free convection of a micropolar fluid in a vertical channel was presented by Chamkha *et al.* [7]. This problem was extended by Kumar et al. [8] to consider the case of a channel with one region filled with micropolar fluid and the other region with a Newtonian fluid. It was found that the effects of the micropolar fluid material parameters suppress the fluid velocity but enhance the microrotation velocity. An analytical solution predicting the characteristics of fluid flow as well as heat and mass transfer was derived. It was reported that an increase of the vortex viscosity parameter tends to decrease the fluid velocity in the vertical channel. The same problem was later reconsidered by Bataineh *et al.* [9]. The problem of the fully developed natural convection heat and mass transfer of a micropolar fluid between porous vertical plates with asymmetric wall temperatures and concentrations was investigated by Abdulaziz *et al.* [10]. However, it is well known that convection, in a binary mixture, can also be induced by Soret effects. For this situation the species gradients result from the imposition of a temperature gradient in an otherwise uniform-concentration mixture. Two kinds of problems have been considered in the literature concerning the convection of a binary mixture filling a horizontal porous layer. The first kind of problems, called double diffusion, considers flows induced by the buoyancy forces resulting from the imposition of both thermal and solutal boundary conditions on the layer. Early investigations on double-diffusive natural convection in porous media primarily focused on the problem of convective instability in a horizontal layer (Nield [11], Taunton *et al.* [12], Poulikakos [13]).

The second kind of problems considers thermal convection in a binary fluid driven by Soret effects. For this situation the species gradients are not due to the imposition of solutal boundary conditions as in the case of double diffusion. Rather, they result from the imposition of a temperature gradient in an otherwise uniform-concentration mixture. Brand and Steinberg [14; 15] investigated the influence of Soret-induced solutal buoyancy forces on the convective instability of a fluid mixture in a porous medium heated isothermally. The first

study of Soret-induced convection was described by Bergman *et al.* [16], while considering natural convection in a cavity filled with a binary fluid. This flow configuration has also been investigated by R. Krishnan *et al.* [17]. As pointed out recently by Rawat *et al.* [18], the study of heat and mass transfer in micropolar fluids is of importance in the fields of chemical engineering, aerospace engineering and also industrial manufacturing effects processes. Sunil *et al.* [19] studied the effect of rotation on double-diffusive convection in a magnetized ferro fluid with internal angular momentum; A. A. Bakr *et al.* [20] studied the double-diffusive convection-radiation interaction on unsteady MHD micropolar fluid flow over a vertical moving porous plate with heat generation and Soret effects. R. A. Mohamed [21]) also analyzed double-diffusive convection-radiation interaction on unsteady MHD flow over a vertical moving porous plate with heat generation and Soret effects, A. Bahloul *et al.* [22] studied double-diffusive and Soret induced convection in a shallow horizontal porous layer. Z. Alloui *et al.* [23] double-diffusive and Soret induced convection of a micropolar fluid in a vertical channel. N. Nithyadevi *et al.* [24] have studied double-diffusive natural convection in a partially heated enclosure with Soret and Dufour effects, Ziya Uddin *et al.* [25] have studied MHD heat and mass transfer free convection flow near the lower stagnation point of an isothermal cylinder imbedded in porous domain with the presence of radiation, A. Pantokratoras [26] has studied the effect of viscous dissipation in natural convection along a heated vertical plate, A. K. H. Kabir *et al.* [27] discovered the effects of viscous dissipation on MHD natural convection flow along a vertical wavy surface with heat generation. Osama Abu-Zeid [28] studied viscous and Joule heating effects over an isothermal cone in saturated porous media. Fully developed natural convection heat and mass transfer of a micropolar fluid in a vertical channel with asymmetric wall temperatures and concentrations was studied by C.Y. Cheng [29]. B. S. Malga *et al.* [30] have studied the finite element analysis for unsteady MHD heat and mass transfer free convection flow of polar fluids past a vertical moving porous plate in a porous medium with heat generation and thermal diffusion. Effect of viscous dissipation in natural convection was studied by Gebhart [31]. The present paper is the extension work of Z. Alloui *et al.* [23] by considering MHD free convection also convection induced by the viscous dissipation effects on fully developed natural convection of heat and mass transfer of a micropolar fluid in a vertical channel.
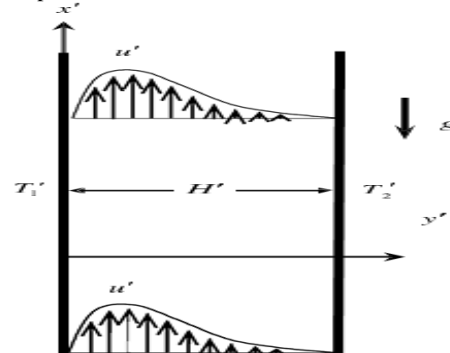

Figure (a). T h e flow configuration and the coordinate system.

2. Mathematical Model

We consider a steady fully developed laminar natural convection flow of a micropolar fluid between two infinite vertical plates (see Fig. (a)). The vertical plates are separated by a distance H′. The convection current is induced by both the temperature and concentration gradients. The flow is assumed to be in the x′ direction, which is taken to be vertically upward along the channel walls, while the y′-axis is normal to the plates. The fluid is assumed to satisfy the Boussinesq approximation, with constant properties except for the density variations in the buoyancy force term.

The density variation with temperature and concentration is described by the state equation

$$\rho = \rho_o \left[1 - \beta'_T (T' - T'_o) - \beta_C (C - C_o) \right]$$

where ρ_o is the fluid mixture density at temperature $T' = T'_o$ and mass fraction $C = C_o$, and $\beta'T$ and βC are the thermal and the concentration expansion coefficients, respectively. In the present investigation the viscous dissipation effects studied and the Dufour effect is neglected since it is well known that the modification of the heat flow due to the concentration gradient is of importance in gases but negligible in liquids. Equations (1)-(4) are Z. Alloui et al. [23]) under these assumptions, the governing equations can be written as:

$$(\mu + \kappa) \frac{d^2 u'}{dy'^2} + \kappa \frac{dN'}{dy'} =$$
$$- \rho_o g \left[\beta'_T (T' - T'_o) - \beta_c (C - C_o) \right] + \sigma B_o^2 u' \tag{1}$$

$$\frac{\gamma}{j} \frac{d^2 N'}{dy'^2} - \frac{\kappa}{j} \left(2N' + \frac{du'}{dy'} \right) = 0 \tag{2}$$

$$\frac{d^2 T'}{dy'^2} + \frac{\upsilon}{\rho_o c_p} \left(\frac{du'}{dy'} \right)^2 = 0 \tag{3}$$

$$\frac{d^2 C'}{dy'^2} = 0 \tag{4}$$

where u' is the velocity component along the x′ direction, and g is the acceleration due to gravity. Further, μ, κ, j, N' and γ are respectively the dynamic viscosity, vortex viscosity, micro-inertia density, angular velocity and spin gradient viscosity. Following Chamkha et al. [7] it is assumed that γ has the form $\gamma = (\mu + \kappa / 2) j$ C_p is the specific heat at constant pressure, ν is the kinematic viscosity $\nu = \dfrac{\mu}{\rho_o}$

The appropriate boundary conditions, applied on the walls of the vertical channel, are:

$$u' = 0, N' = -n \frac{du'}{dy'}, T' = T'_1, (1-a)C + a \frac{dC}{dy'} =$$
$$(1-a)C_1 - a \frac{D'}{D} C_o (1 - C_o) \frac{dT'}{dy'} \quad on \quad y' = 0 \tag{5}$$

$$u' = 0, N' = -n \frac{du'}{dy'}, T' = T'_2, (1-a)C + a \frac{dC}{dy'} =$$
$$(1-a)C_2 - a \frac{D'}{D} C_o (1 - C_o) \frac{dT'}{dy'} \quad on \quad y' = H' \tag{6}$$

where $0 \leq n \leq 1$ is a boundary parameter that indicates the degree to which the microelements are free to rotate near the channel walls. The case n = 0 represents concentrated particle flows in which the microelements close to the wall are unable to rotate S.K. Jena et al. [32]. Finally, according to Peddieson [33] the case n = 1 is applicable to the modeling of turbulent boundary layer flows. D and D' are respectively the molecular diffusion coefficient and the thermodiffusion coefficient.

The governing equations are non-dimensionalized by scaling length by H'

$u' = \dfrac{\mu G_r}{\rho_o H' u}$ is the velocity,

$N' = \dfrac{\mu G_r}{\rho_o H'^2 N}$ is the microrotation,

$G_r = g \rho_o^2 \beta'_T \dfrac{(T_1 - T_o) H'^3}{\mu^2}$ is the Grashof number,

$M = \dfrac{\sigma B_o^2 H'^2}{\mu}$ is the Magnetic parameter,

$T = \dfrac{T' - T'_o}{T'_1 - T'_o}$ is the reduced temperature,

$S = \dfrac{C - C_o}{\Delta C}$ is the reduced concentration,

$\Delta T' = T'_1 - T'_o$ and

$\Delta C = C_1 - C_o$ for double - diffusive convection,

$\Delta C = -C_o (1 - C_o) \Delta T' \dfrac{D'}{D}$ for Soret - driven convection,

$E_c = \dfrac{\mu G_r}{(\rho_o H') \Delta t}$ Eckert number,

$\varphi = \dfrac{\beta_c \Delta C}{\beta'_T \Delta T'}$ is the buoyancy ratio,

$R_T = \dfrac{T'_2 - T'_o}{T'_1 - T'_o}$ is the buoyancy ratio,

$R_S = \dfrac{C_2 - C_o}{C_1 - C_o}$ is the wall concentration ratio,

$K = \dfrac{\kappa}{\mu}$ is the vortex viscosity parameter,

$B = \dfrac{H'^2}{j}$ is the micro - inertia parameter,

the subscript ′ indicates a reference state.

The dimensionless equations governing the present problem then read

$$(1+K)\frac{d^2u}{dy^2} + K\frac{dN}{dy} = -[T+\varphi S] + Mu \qquad (7)$$

$$\left(1+\frac{K}{2}\right)\frac{d^2N}{dy^2} - BK\left(2N+\frac{du}{dy}\right) = 0 \qquad (8)$$

$$\frac{d^2T}{dy^2} + E_c\left(\frac{du}{dy}\right)^2 = 0 \qquad (9)$$

$$\frac{d^2S}{dy^2} = 0 \qquad (10)$$

The corresponding boundary conditions in dimensionless form are

$$u = 0, N = -n\frac{du}{dy}, T = 1,$$

$$(1-a)S + a\frac{dS}{dy} = (1-a) + a\frac{dT}{dy} \ on \quad y = 0 \qquad (11)$$

$$u = 0, N = -n\frac{du}{dy}, T = R_T,$$

$$(1-a)S + a\frac{dS}{dy} = (1-a)R_S + a\frac{dT}{dy} \ on \quad y = 1 \qquad (12)$$

In the present formulation the particular case a = 0 corresponds to double-diffusive convection for which the solutal buoyancy forces are induced by the imposition of a constant concentration such that S = 1 on y = 0 and $S = R_S$ on y = 1. On the other hand, a = 1 corresponds to the case of a binary fluid subject to the Soret effect. For this situation, it follows from Eqs. (11) and (12) that $dS/dy = dT/dy$ on y = 0, 1.

3. Method of Solution

It can be shown that Eqs. (7) - (10), together with the boundary conditions Eqs. (11) - (12) possess the following finite element solution, obtained with the help of the MATLAB software. In order to reduce the above system of differential equations to a system of dimensionless form, we may represent the velocity and microrotation, temperature and concentration by applying the Galerkin finite element method for equation (7) over a typical two-noded linear element $(e), (y_j \le y \le y_k)$ is:

$$u = N.\phi, \ N = [N_j, N_k], \ \phi = \begin{bmatrix} u_j \\ u_k \end{bmatrix},$$

$$N_j = \frac{y_k - y}{l}, \ N_k = \frac{y - y_j}{l}, \ l = y_k - y_j = h$$

$$\int_{y_j}^{y_k} N^T\left[(1+K)\frac{d^2u}{dy^2} + K\frac{dN}{dy} + [T+\varphi S] - Mu\right]dy = 0 \qquad (13)$$

$$\int_{y_j}^{y_k} N^T\left[(1+K)\frac{d^2u}{dy^2} + Mu - R\right]dy = 0$$

$$where \quad R = K\frac{dN}{dy} + (T+\varphi S)$$

The element equation given by

$$\int_{y_j}^{y_k}(1+K)\begin{bmatrix} N'_j N'_j & N'_j N'_k \\ N'_k N'_j & N'_k N'_k \end{bmatrix}\begin{bmatrix} u_j \\ u_j \end{bmatrix}dy + M$$

$$\begin{bmatrix} N_j N_j & N_j N_k \\ N_k N_j & N_k N_k \end{bmatrix}\begin{bmatrix} u_j \\ u_j \end{bmatrix}dy - R\begin{bmatrix} N_j \\ N_k \end{bmatrix}dy = 0$$

$$\int_{y_j}^{y_k} S_M dy = \int_{y_j}^{y_k} R^* dy \qquad (14)$$

$$where \quad S_M = \int_{y_j}^{y_k}(1+K)\begin{bmatrix} N'_j N'_j & N'_j N'_k \\ N'_k N'_j & N'_k N'_k \end{bmatrix}\begin{bmatrix} u_j \\ u_j \end{bmatrix}dy +$$

$$M\begin{bmatrix} N_j N_j & N_j N_k \\ N_k N_j & N_k N_k \end{bmatrix}\begin{bmatrix} u_j \\ u_j \end{bmatrix}dy \quad and \quad R^* = R\begin{bmatrix} N_j \\ N_k \end{bmatrix}dy$$

$$S_M = \frac{(1+K)}{l}\begin{bmatrix} 1 & -1 \\ -1 & 1 \end{bmatrix}\begin{bmatrix} u_j \\ u_j \end{bmatrix} + \frac{Ml}{6}\begin{bmatrix} 1 & 2 \\ 2 & 1 \end{bmatrix}\begin{bmatrix} u_j \\ u_j \end{bmatrix}$$

$$and \quad R^* = R\frac{l}{2}\begin{bmatrix} 1 \\ 1 \end{bmatrix}$$

We write the element equation for the elements $(y_{i-1} \le y \le y_i)$ and $(y_i \le y \le y_{i+1})$. Assembling these element equations, we get

$$\frac{(1+K)}{l}\begin{bmatrix} 1 & -1 & 0 \\ -1 & 2 & -1 \\ 0 & -1 & 1 \end{bmatrix}\begin{bmatrix} u_{i-} \\ u_i \\ u_{i+1} \end{bmatrix} + \qquad (15)$$

$$\frac{Ml}{6}\begin{bmatrix} 2 & 1 & 0 \\ 1 & 4 & 1 \\ 0 & 1 & 2 \end{bmatrix}\begin{bmatrix} u_{i-} \\ u_i \\ u_{i+1} \end{bmatrix} = R\frac{l}{2}\begin{bmatrix} 1 \\ 2 \\ 1 \end{bmatrix}$$

Now put row corresponding to the node i to zero, from equation (15) the difference schemes with l=h is

$$\frac{(1+K)}{h}(-u_{i-1} + 2u_i - u_{i+1}) +$$

$$\frac{Mh}{6}(u_{i-1} + 4u_i + u_{i+1}) = R^* \qquad (16)$$

Using the Cranck-Nicolson method to the equation (16), we obtain:

$$A_1 u_{i-1}^{j+1} + A_2 u_i^{j+1} + A_3 u_{i+1}^{j+1} =$$

$$A_4 u_{i-1}^j + A_5 u_i^j + A_6 u_{i+1}^j + R^* \qquad (17)$$

Similarly, the equations (8), (9) and (10) are becoming as follows:

$$B_1 N_{i-1}^{j+1} + B_2 N_i^{j+1} + B_3 N_{i+1}^{j+1} =$$
$$B_4 N_{i-1}^{j} + B_5 N_i^{j} + B_6 N_{i+1}^{j} + R_1^{*} \qquad (18)$$

$$C_1 T_{i-1}^{j+1} + C_2 T_i^{j+1} + C_3 T_{i+1}^{j+1} =$$
$$C_4 T_{i-1}^{j} + C_5 T_i^{j} + C_6 T_{i+1}^{j} + R_2^{*} \qquad (19)$$

$$D_1 S_{i-1}^{j+1} + D_2 S_i^{j+1} + D_3 S_{i+1}^{j+1} =$$
$$D_4 S_{i-1}^{j} + D_5 S_i^{j} + D_6 S_{i+1}^{j} \qquad (20)$$

$$A_1 = \left(\frac{Mh}{6} - \left(\frac{1+k}{h} \right) \right), \quad A_2 = \left(\frac{Mh}{3} + 2\left(\frac{1+k}{h} \right) \right),$$

$$A_3 = \left(\frac{Mh}{6} - \frac{1+k}{h} \right), \quad A_4 = \left(\left(\frac{1+k}{h} \right) - \frac{Mh}{3} \right),$$

$$A_5 = -\left(\frac{Mh}{3} + 2\left(\frac{1+k}{h} \right) \right), \quad A_6 = \left(\left(\frac{1+k}{h} \right) - \frac{Mh}{6} \right)$$

$$B_1 = \left(\frac{hBK}{3} - \left(\frac{1+\frac{k}{2}}{h} \right) \right), \quad B_2 = \left(\frac{4hBk}{3} + 2\left(\frac{1+\frac{k}{2}}{h} \right) \right),$$

$$B_3 = \left(\frac{hBK}{3} - \frac{1+\frac{k}{2}}{h} \right), \quad B_4 = \left(\left(\frac{1+\frac{k}{2}}{h} \right) - \frac{hBK}{3} \right),$$

$$B_5 = -\left(\frac{4hBK}{3} + 2\left(\frac{1+\frac{k}{2}}{h} \right) \right), \quad B_6 = \left(\left(\frac{1+\frac{k}{2}}{h} \right) - \frac{BKh}{3} \right)$$

$$C_1 = -\frac{1}{h}, \quad C_2 = \frac{2}{h}, C_3 = -\frac{1}{h}, C_4 = \frac{1}{h}, C_5 = -\frac{2}{h}, C_6 = \frac{1}{h}$$

$$D_1 = -\frac{1}{h}, \quad D_2 = \frac{2}{h}, D_3 = -\frac{1}{h}, D_4 = \frac{1}{h}, D_5 = -\frac{2}{h}, D_6 = \frac{1}{h}$$

$$R^{*} = h\left(K\left(\frac{N_{i+1} - N_{i-1}}{h} \right) + T + \varphi S \right),$$

$$R_1^{*} = -hK\left(\frac{u_{i+1} - u_{i-1}}{h} \right), \quad R_2^{*} = -hE_c\left(\frac{u_{i+1} - u_{i-1}}{h} \right)^2$$

Here $r = k / h^2$ where k, h is mesh sizes along y direction and x direction respectively. Index i refers to space and j refers to time. The mesh system consists of $h=0.1$ for velocity profiles and concentration profiles and $k=0.1$ has been considered for computations. In equations (8)-(10), taking i=1(1) n and using initial and boundary conditions (11) and (12), the following system of equation are obtained:

$$A_i X_i = B_i, \quad i = 1,2,3..... \qquad (21)$$

Where Ai's are matrices of order n and Xi and $Bi's$ are column matrices having n-components. The solution of above system of equations are obtained using Thomas algorithm for velocity, angular velocity and temperature. Also, numerical solutions for these equations are obtained by MATLAB program. In order to prove the convergence and stability of Galerkin finite element method, the same MATLAB-Program was run with slightly changed values

of h and k, no significant change was observed in the values of μ, N, T, S

4. Results and Discussion

The numerical computations for the velocity u, angular velocity fields N for various governing parameters the buoyancy ratio φ, vortex viscosity parameter K, dimensionless microgyration n and constant a are illustrated in the graphs. Figure 1 illustrates the influence of vortex viscosity parameter K on the distribution of velocity u and microrotation N for n=0,a=0 and for φ=5 in Fig.1(a) and φ=-5 in Figure1(b). It is observed that with the increasing the value of K the intensity of convective velocity u is reduced as compared to the Newtonian fluid situation (K=0). In fact, it is found that as $K \rightarrow \infty, u \rightarrow 0$. The influence of parameter K on the microrotation N it is noticed that the variation with K of the value of N evaluated at the position half of the channel also presented in the graphs it can be seen that the intensity of N first increases with increase of K, the reverse phenomenon is observed later.

Figure 1(b) shows the results obtained from φ=-5, i.e., when thermal and solutal buoyancy forces are opposing each other for this situation in case of double-diffusive convection indicates that the flow direction is downwards, since the solutal buoyancy forces predominant. The velocity profiles increases with the increase of K are observed from Figure 1(b). It is seen that for $K=0$ when N=0, since no rotation can be occur in the absence of micropolar elements (Newtonian fluid situation). Microrotation N decreases with the increase of K up to half of the channel whereas microrotation N flow direction is now downward and the reverse phenomenon is observed.

The effect of buoyancy ratio φ velocity u, microrotation N exemplified in Figure 2 for the case a=0, n=0, K=5 in the absence of solute concentration effect i.e. when φ=0 the flow is induced solely by the imposed temperature gradients. It is observed from this figure when $\varphi < 0$ the thermal and solutal buoyancy forces act in the same direction and the flow is considered to aided thus the magnitude of the fluid of the fluid velocity and microrotation promoted in the vertical channel on the other hand when $\varphi < 0$ the solutal and buoyancy forces acts in opposite direction as a result the flow direction is now reversed since it is governed by the predominant solutal effects.

Figure 3 depicts the influence of micropolar parameter n velocity u, microrotation N profiles K=5, φ=10 and a=0, it can be seen from this figure, upon increase the value of n, the concentration of the solution becomes weaker such that the particles near the walls are free to rotate, which results in an enhancement of the flow. It is also seen that the velocity u increases with the increase of n.

The effect of magnetic field parameter M on the velocity profiles u and mocrorotation N for K=5, φ=5 when a=0 is shown in Figure 4 (a) and K=5, φ=-5 when a=0 is shown in Figure 4 (b). Here it is observed that the velocity profiles decrease with an increase of M, microrotation profiles increase up to the center of the channel, the reverse phenomenon is observed in the other part of the channel. Figure 4 (b) indicates that the velocity flow

direction is now downward for $\varphi=-5$, since the solute buoyancy forces are free dominant. It can be seen that the velocity profiles u increase with an increase of M, The microrotation N decreases with the increase of M, up to the middle of the channel (flow direction is upward) and it increases with the increase of M, observed in the other part of the channel.
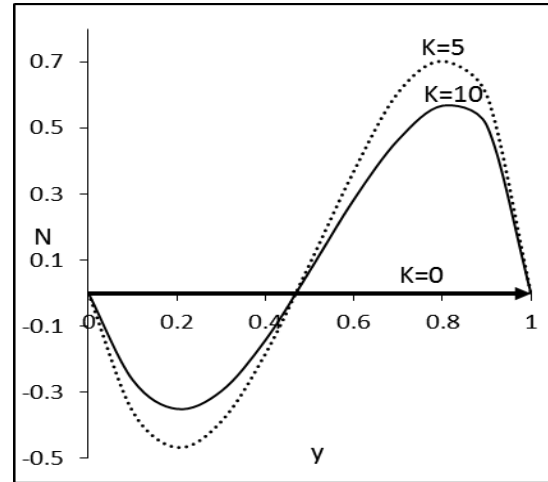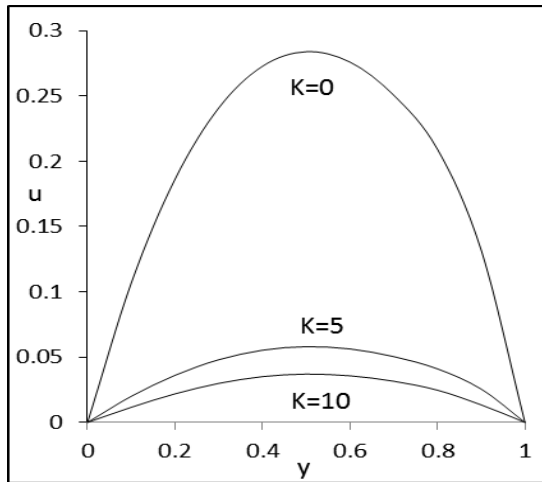
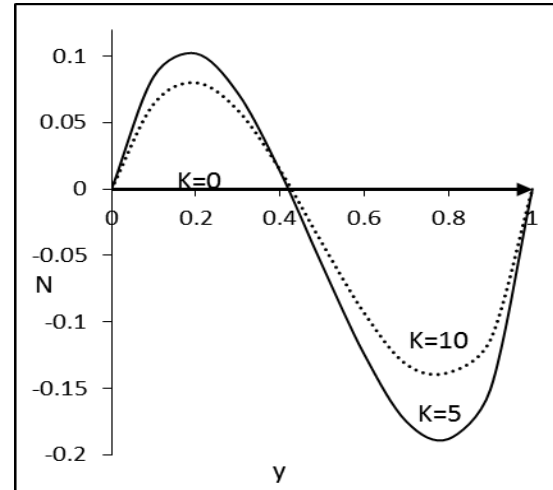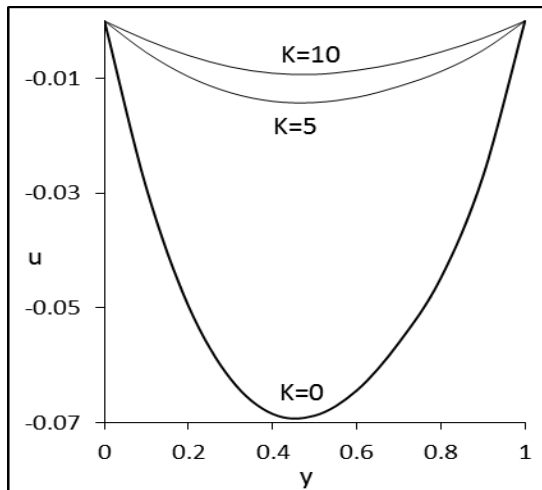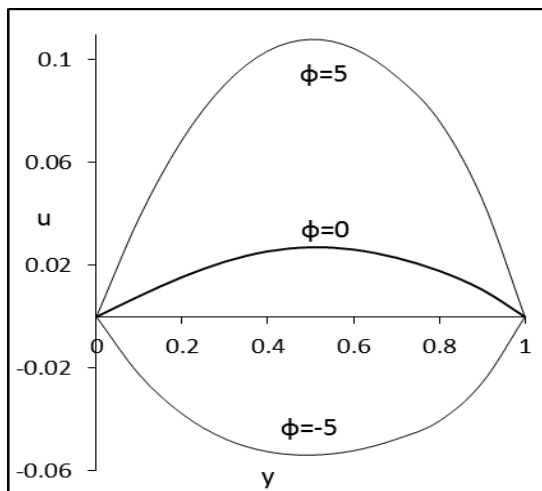**Figure 1(a).** Effect of Parameter *K* on the velocity profiles *u* and the microrotation *N* for *n=0, a=0* and *φ=5*.

Figure 1(b). Effect of Parameter *K* on the velocity profiles *u* and the microrotation *N* for *n=0, a=0* and *φ=-5.*
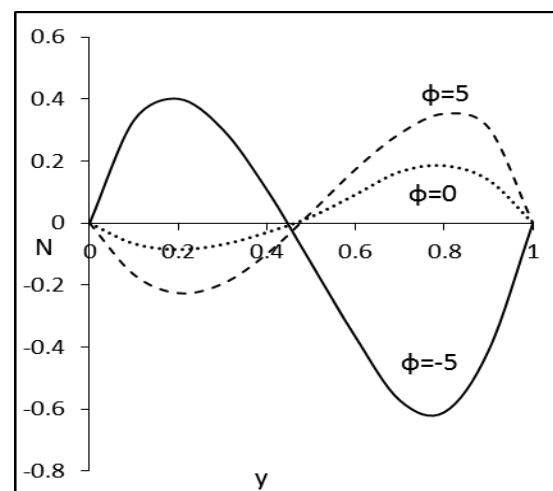
Figure 2. Effects of buoyancy ratio *φ* on the velocity profiles **u** and the microrotation profiles *N* for *K = 5, n = 0* and *a = 0.*
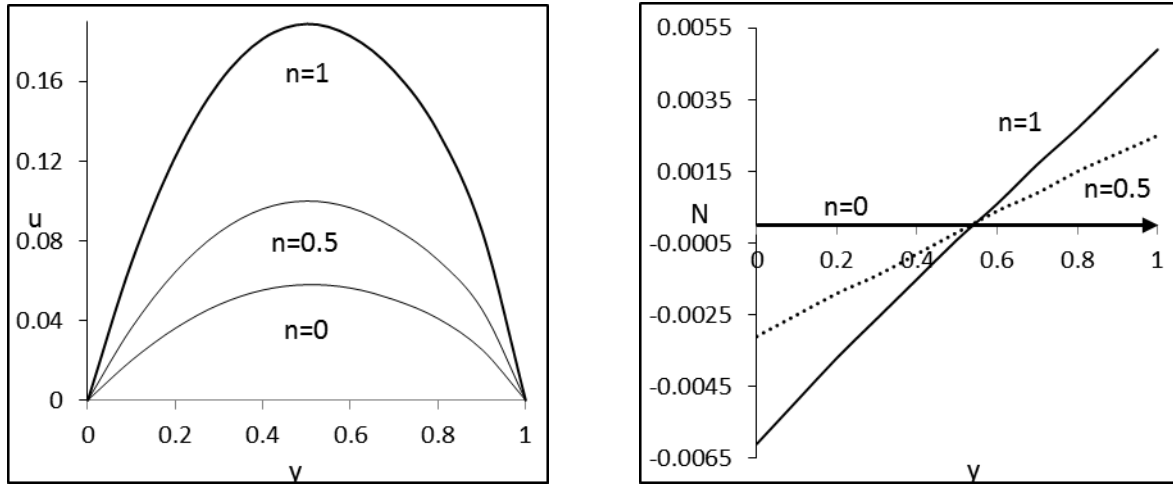
Figure 3. Effects of parameter *n* on the velocity profiles *u* and the microrotation profiles *N* for *K =5, φ = 10* and *a = 0*.
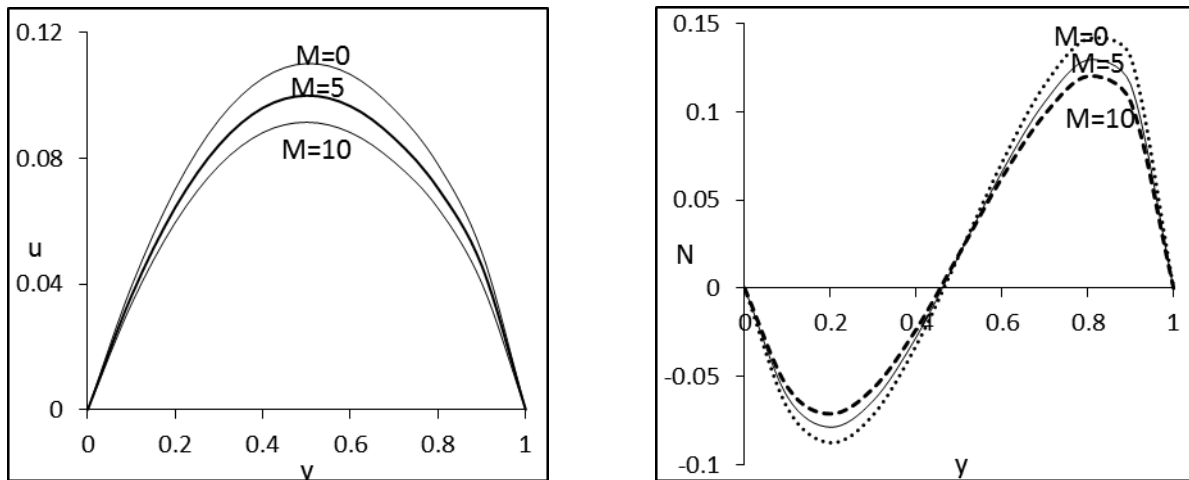

Figure 4(a). Effects of parameter *M* on the velocity profiles *u* and the microrotation profiles *N* for *K =5, φ=5* and *a=0*.
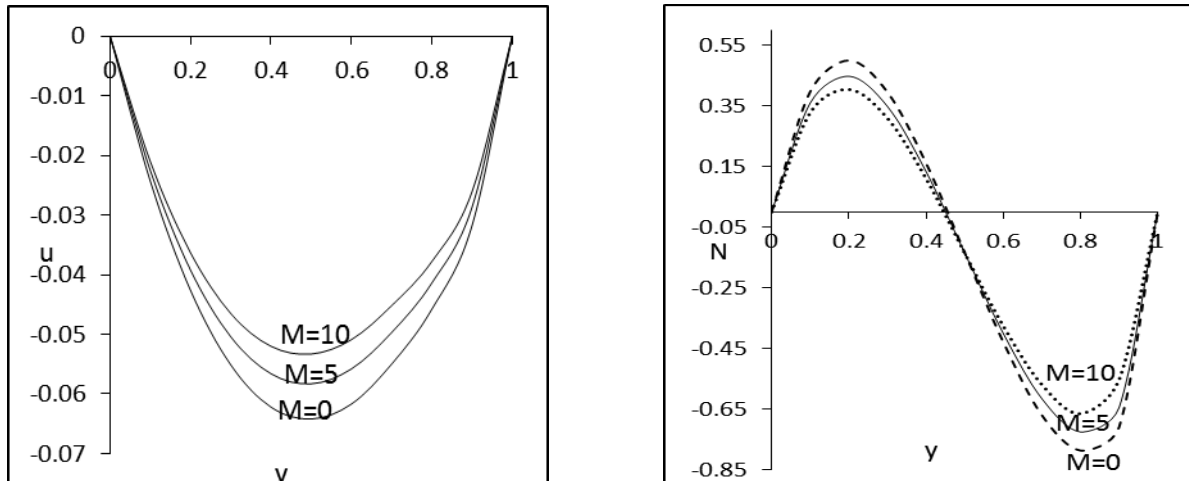

Figure 4(b). Effects of parameter *M* on the velocity profiles *u* and the microrotation profiles *N* for *K =5, φ=-5* and *a=0*.

Figures 5-10 show that the velocity profiles u and microrotation N for different values of flow parameter when *a=1*. The effect of magnetic parameter M on the velocity profiles u and mocrorotation N for *K=5, φ=5* is shown in Figure 5 (a) and *K=5, φ=-5* is shown in Figure 5 (b), it remains the same when compared with *a=0* in the present case *a=1*. The effect of vortex viscosity parameter K, on the velocity profiles u and microrotation N are shown in Figure 6 for both *φ=5* and *φ=-5* in the case of *a=1, n=0*, the effect of K is the same in both cases *a=0*

and *a=1*, whereas in the present case (*a=1*) for *φ=-5* from Figure 6 (b) it indicates that the flow direction is upward in the present case, whereas it is downward in case *a=0*. It is also noticed that the effect of K decreases the velocity profiles u, the microrotation N decreases up to half of the channel and decreases the other part of the channel, as observed with the effect of K; the reverse phenomenon is also observed in the present case (*a=1*) when compared to *a=0*.

The buoyancy ratio parameter φ effect on the velocity profiles u and microrotation N are shown in Figure 7. It is clear that the velocity profiles u increase with the increase of φ from 0 to 10, whereas they decrease from 0 to -10. However, up on increasing φ, considerably the flow pattern depends on the sign of the parameter up or down in the halves of the channel. It can also be seen that the microrotation profiles N decrease with the increase of φ from 0 to 10 and increase with the decrease of φ from 0 to -10, in the first half of the channel, as indicated from the Figure7, and the reverse phenomenon is observed in the other half of the channel.

Figure 8 illustrates the influence of micro-gyration parameter n on velocity u and microrotation N for $φ=10$, $K=5$, $a=1$. It is noticed that the velocity u increases with the increase of n. In the present case for $a=1$, the results indicate the intensity of convective flow u and that of the angular velocity N are minimum for $n = 0$. This particular value of n represents the case where the concentration of the microelements is sufficiently large that the particles close to the walls are unable to rotate. Upon increasing the value of n, the concentration of the solution becomes weaker such that the particles near the walls are free to rotate. Thus, as n is augmented the microrotation term is augmented, which induces an enhancement of the flow.

Figures 9 (a) & (b) illustrate the volume flow rate Q with the buoyancy ration parameter φ, when $K=1.5$, for the various values of micro-gyration parameter n at $a=0$ and $a=1$ for the case of double-diffusive convection it is observed that when both the thermal and solutal buoyancy forces are aiding ($\phi > 0$), the flow direction is upward (Q > 0). The reverse is true (Q < 0) when both the thermal and solutal buoyancy forces are opposing $(\phi < 0)$. On the other hand, for the case of soret induced convection, the flow rate is found to be independent of the buoyancy ratio ϕ. This follows the fact that, for this situation, the quantity of the solute between the two vertical plates remains constant. The Soret effect acts merely to redistribute the concentration in the system, giving rise to local increase or decrease of the local velocity. However, the global flow rate remains constant. Also, as discussed above, upon increasing the value of n the intensity of the velocity field (and thus of the flow rate Q) is enhanced.

The dimensionless total rate, E, at which heat is added to the fluid, is plotted in Figure 10 (a) and (b) as a function of the buoyancy ratio ϕ and the micro-gyration parameter n, for the case $K = 1.5$. Figure 10 (a) shows that, in the case of double diffusive convection, for ($\phi > 0$), increasing ϕ results in an augmentation of the strength of the convective motion such that E increases. For $(\phi < 0)$, the results are similar but, since the flow direction is now downward, the value of E is negative. On the other hand, the results obtained for soret-induced convection, Figure 10 (b), are quite different. For this situation, the velocity profiles (not presented here) indicate that for $(\phi >> 0)$ the flow is upward near the left hotter wall and downward near the right colder one. Thus, the total rate E, at which heat is added to the fluid, is promoted upon increasing ϕ as a result of the increase of the flow intensity near the hotter wall.
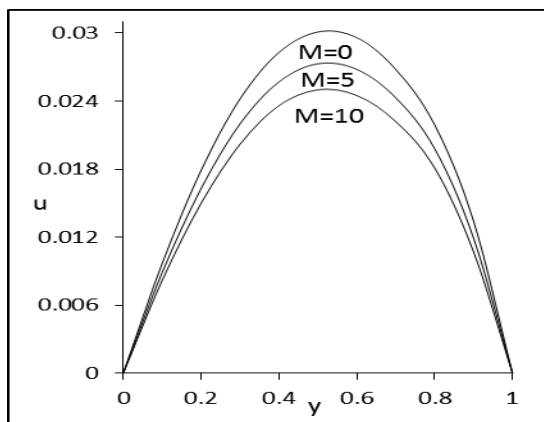

Figure 5(b). Effects of parameter *M* on the velocity profiles *u* and the microrotation profiles *N* for *K =5, φ=-5* and *a=1.*
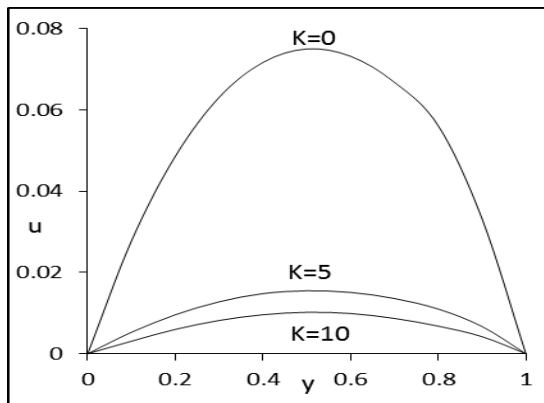

Figure 6(a): Effect of Parameter *K* on the velocity profiles *u* and the microrotation *N* for *n=0, a=1* and *φ=5.*
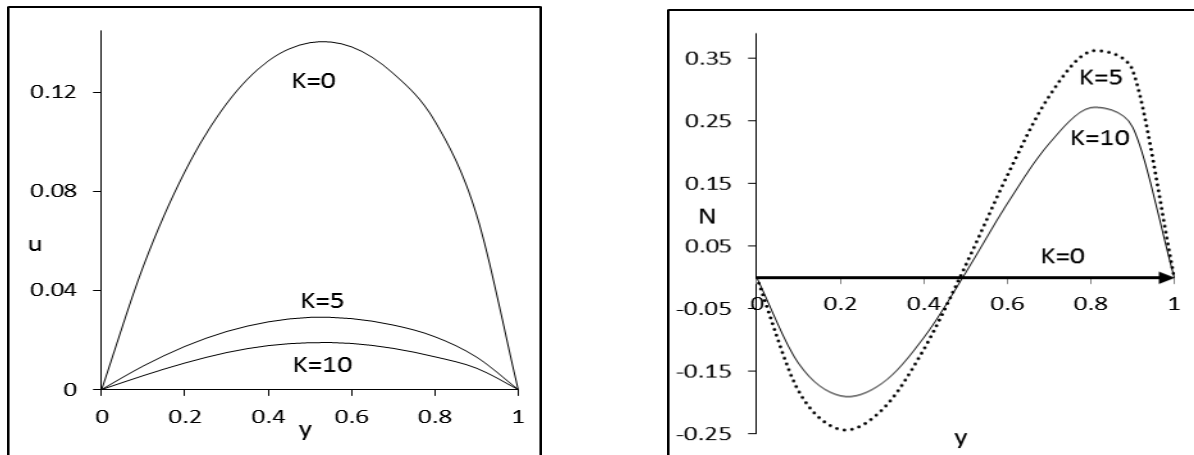
Figure 6(b): Effect of Parameter *K* on the velocity profiles *u* and the microrotation *N* for *n=0, a=1* and *φ=-5*.
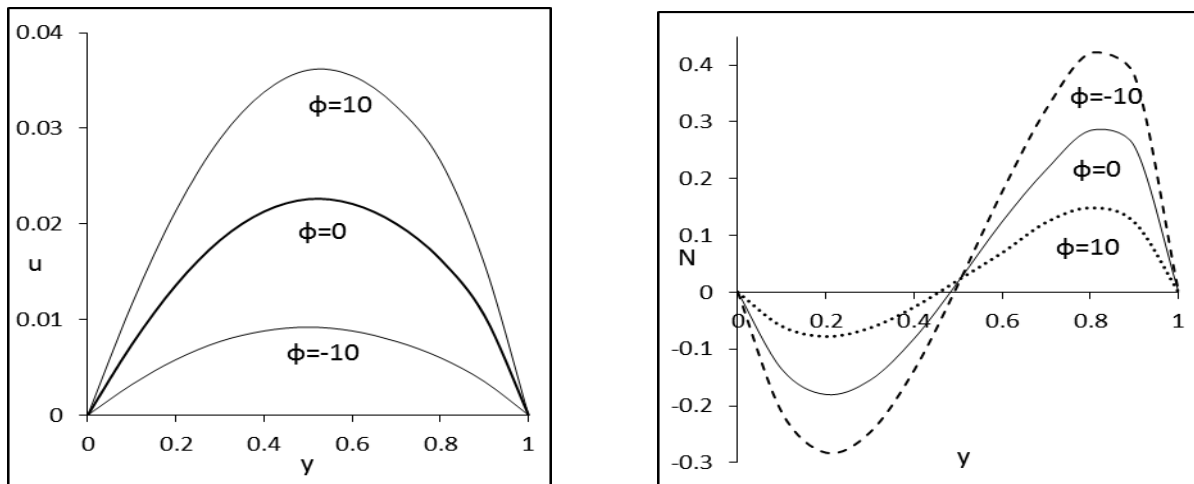

Figure 7. Effects of buoyancy ratio *φ* on the velocity profiles *u* and the microrotation profiles *N* for *K = 5, n = 0* and *a = 1*.
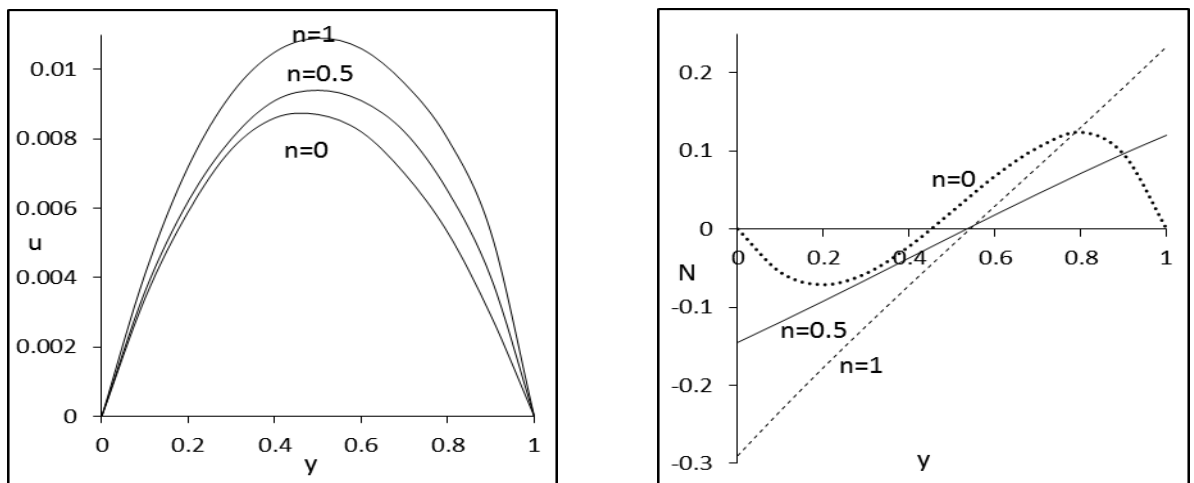

Figure 8. Effects of parameter *n* on the velocity profiles *u* and the microrotation profiles *N* for *K=5, φ=10* and *a = 1*.
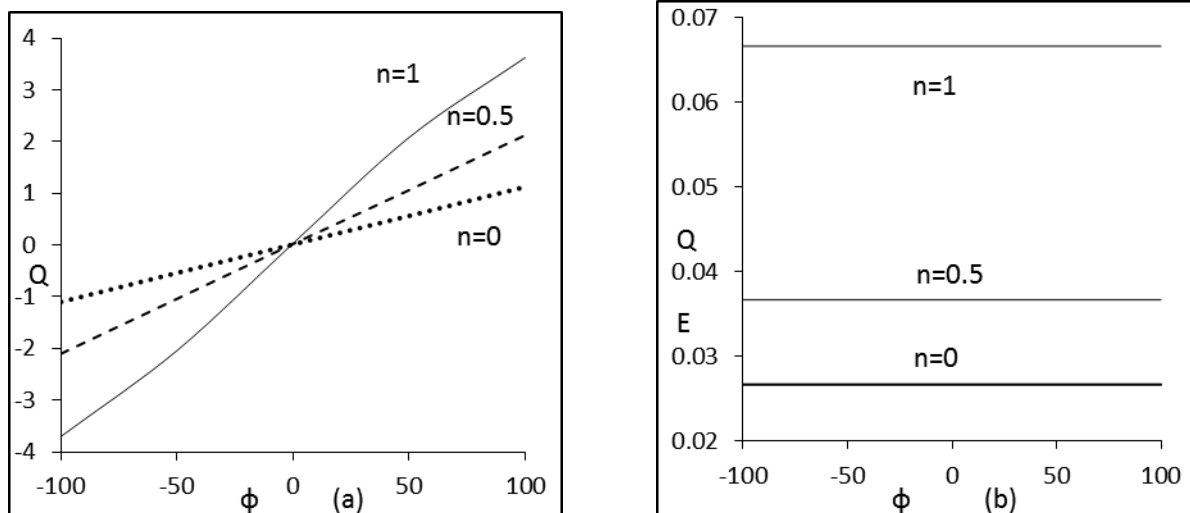
Figure 9. Effects of buoyancy ratio φ and parameter *n* on the volume flow rate *Q* for *K = 1.5, (a) a = 0, (b) a = 1.*
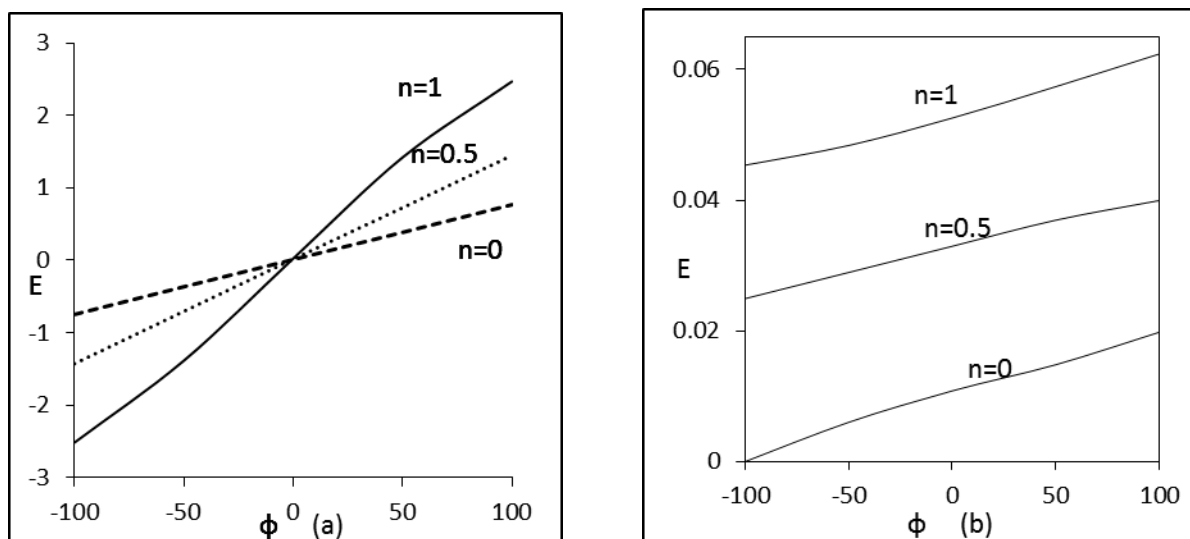

Figure 10. Effects of buoyancy ratio φ and parameter *n* on the total rate at which heat is added to the fluid, *E*, for *K = 1.5, a = 0, (b) a = 1.*

Let's now consider the buoyancy ratio. The dimensionless total rate, Φ, at which species are added to the fluid, is depicted in Figure 11 as a function of ϕ and the micro-gyration parameter n, for the case *K = 1.5*. The Soret-induced convection, represented by a dotted line, indicates that $\Phi = 0$ independently of n. This is expected since, for this situation, the solid boundaries are impermeable to concentration. The Soret effect is merely to redistribute the originally uniform concentration within the system. However, for double diffusion, the solid lines indicate that increasing ϕ, i.e., increasing the strength of the convective flow, results in an enhancement of the rate of mass transfer through the system. These results are similar to those reported by Z. Alloui *et al.* [23]. Also, it is observed from Figure 11 that, for a given value of ϕ, Φ decreases as the value of n is reduced toward *n = 0*. As already mentioned, a decrease of n corresponds to an increase of the concentration of the solution such that the particles close to the solid boundaries are unable to rotate. This results in a decrease of the flow rate and thus a decrease of Φ. The volume flow rate, Q, and total rate at which heat is added to the fluid, E, are plotted in Figure 12 as a function of K for $\phi = 2$ and *n = 0*. Here again, the results obtained for double-diffusive convection and Soret-

induced convection are qualitatively similar. In the limit $K \rightarrow 0$ both Q and E tend asymptotically to constant values corresponding to the Newtonian fluid situation. On the other hand, in the limit $K \rightarrow \infty$, both Q and E become negligible, due to the increase of the vortex viscosity.

It is seen from the Figure 13 for the values of magnetic parameter *M = 0, 5, 10*, the velocity decreases up to the position of *y=0*. At the position of *y=5*, velocity becomes constant, that is, velocity profiles meet at a point and then cross the side and increasing with magnetic parameter *M*. This is because of the velocity profiles, with lower peak values for higher values of magnetic parameter *M*, tend to decrease comparatively slower along y-direction than velocity profiles with higher peak values for lower values of magnetic parameter *M*. We may conclude that for increasing values in *M*; the Lorentz force, which opposes the flow, there is a fall in velocity maximum due to the retarding effect of the magnetic force in the region. As a result, the momentum boundary layer thickness becomes larger and the separation of the boundary layer will occur earlier. Here, it is observed that the increase in the viscous dissipation (Ec) decreases the velocity.

It is also observed from Figure 14 that as the viscous dissipation parameter (Ec) increases, the temperature profiles increase. The increase in the viscous dissipation cools the fluid. The temperature profile for various values of the viscous dissipation parameter (Ec) while the other parameters are kept constant. It is found that the increase in viscous dissipation parameter (Ec) leads to a corresponding increase in the temperature profile. It is also seen that the temperature decreases at a certain portion of the channel and then increases, this could be due to the dissipation effect and the harmonic pressure term.

It is known that the viscous dissipation produces heat due to a drag between the fluid particles and this extra heat causes an increase of the initial fluid temperature (see Figure 14). This increase of temperature causes an increase of the buoyant force. The increase of the buoyant force causes an increase of the fluid velocity. The bigger fluid velocities cause a bigger drag between the fluid particles and consequently bigger viscous heating of the fluid. The new increase of fluid temperature influences the buoyant force and this procedure goes on. There is a continuous interaction between the viscous heating and the buoyant

force. This mechanism produces different results in the upward and downward flow. In the upward flow, where the fluid is warmer than the ambient, the extra viscous heat is added to the initial heat (the warm fluid becomes warmer) and the fluid velocity increases. In the downward flow, the fluid is cooler than the ambient and the viscous heating causes an increase in the initial fluid temperature (the cold fluid becomes warmer).

In many material processing applications, such as extrusion hot rolling, drawing and continuing costing, materials continuously move a channel. In such industrial applications, it is of great importance to encounter the heat transfer from the moving boundary to the surrounding fluid and vice versa. However, the moving boundaries deform the fluid velocity profiles and shear the fluid layer near the boundary resulting in local changes in velocity gradient thus the Eckert number effects may not be neglected in heat transfer analysis, associated with moving boundaries. The thermal energy generated due to Eckert number is significant near the wall, which alters the heat transfer rates following the changes in the temperature profiles.
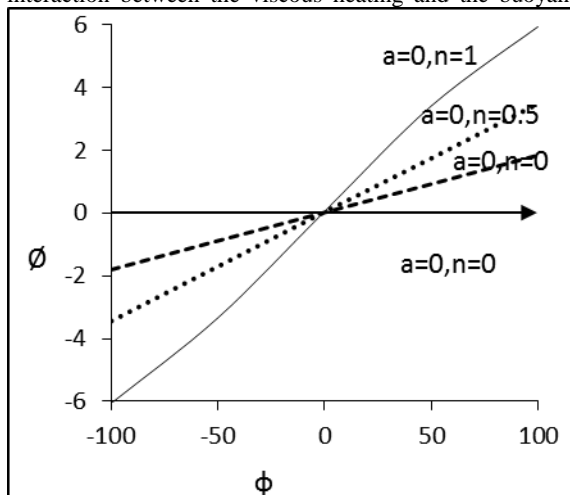

Figure 11. Effects of parameter K on the volume flow rate Q total rate at which heat is added to the fluid for $\varphi = 2$ and $n = 0$.
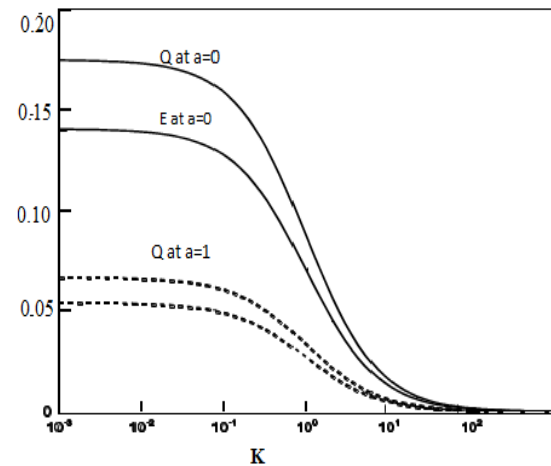

Figure 12. Effects of parameter K on the volume flow rate Q and on the total rate at which heat is added to the fluid for $\varphi = 2$ and $n=0$
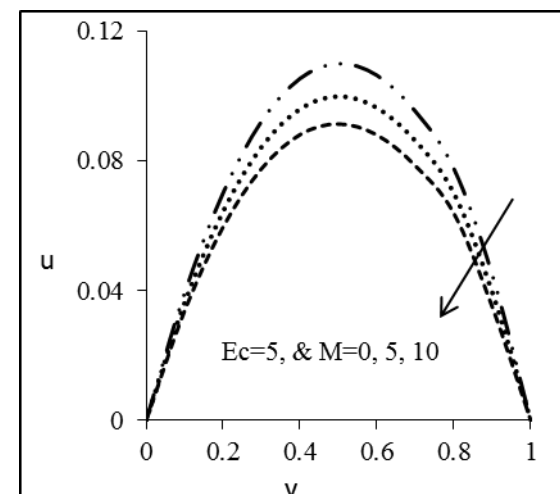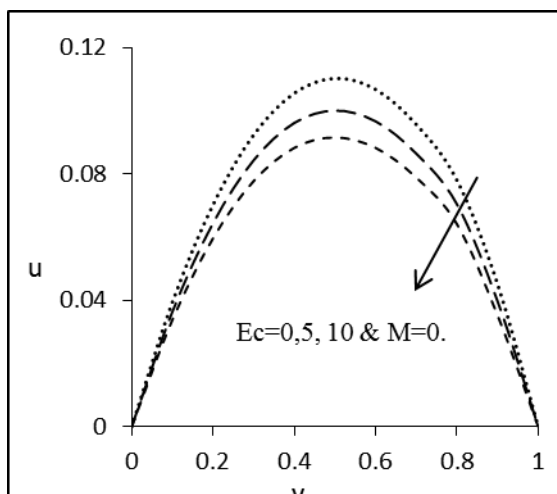

Figure 13. Effects of Viscous dissipation (Ec) on the Velocity Profiles u
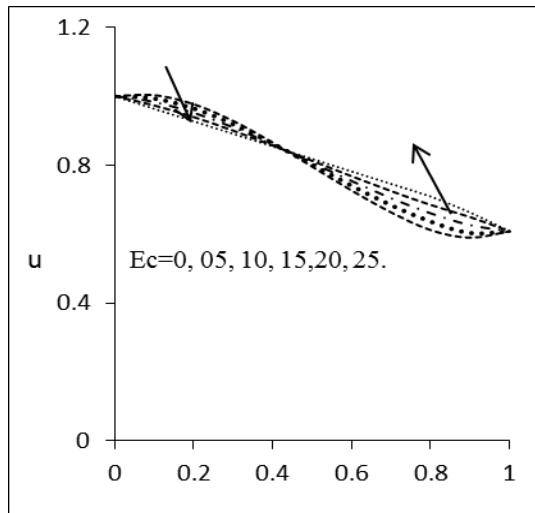
Figure 14. Effects of Viscous dissipation(**Ec**) on the Temperature Profiles **T**

Table. 1 presents a comparison between the numerical, analytical and present solution for $K=1.5$, $B = 1$, $\varphi = 2$, $R_T = 0.6$, $R_S=0.3$, $n = 0$ and $a = 0$. It must be mentioned that in the case of $a = 0$ and $n = 0$ the present results are similar to those reported by Z. Alloui *et al.* [23]. There is a good agreement with the previous author's results.

Table 1. Presents a comparison between the numerical, analytical and present solution for $K = 1.5$, $B = 1$, $\varphi = 2$, $R_T = 0.6$, $R_S = 0.3$, $n = 0$ and $a = 0$.

Profiles	Analytical	Numerical Analytical	Present
u	1.06092	1.06092	1.05925
N	0.14075	0.14075	0.14078

Skin Friction (Shear stress) and Nusselt number (Rate of Heat Transfer)

$$\text{Nusselt number (rate of heat transfer)} = \frac{H'}{\kappa(T_1 - T_o)} = \frac{dT}{dy}\bigg|_{y=0}$$

$$\text{Skin friction (Shear stress)} = \frac{2\tau_w}{\rho_o u^2} = \frac{du}{dy}\bigg|_{y=0}$$

The profiles for skin friction and the rate of heat transfer with viscous dissipation (Ec) parameter are shown graphically in Figure 15, depicting the distribution of the skin friction with the variation of material parameter, magnetic parameter and viscous dissipation parameter. It is clear from the figure that for assisting flow skin friction decreases with the increase of material parameter and magnetic parameter, while a reverse pattern is observed for opposing flow. The rate of heat transfer increases with an increase in viscous dissipation (Ec) parameter. Thus, fast cooling of the plate can be achieved by increasing a/c. It can also be obtained by increasing the material parameter, magnetic field parameter for the opposing flow while for assisting flow, fast cooling of the plate can also be achieved by decreasing the material parameter or magnetic parameter.
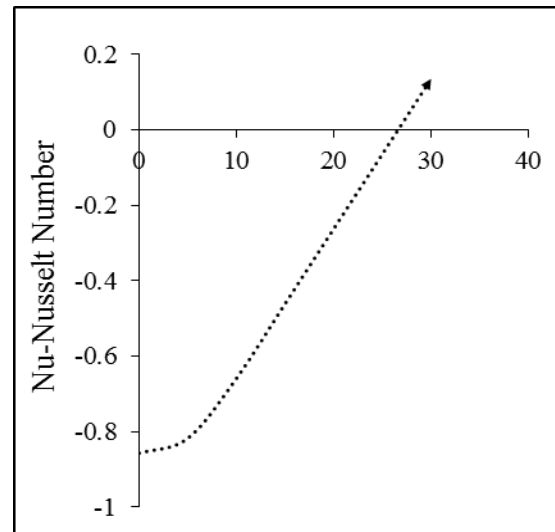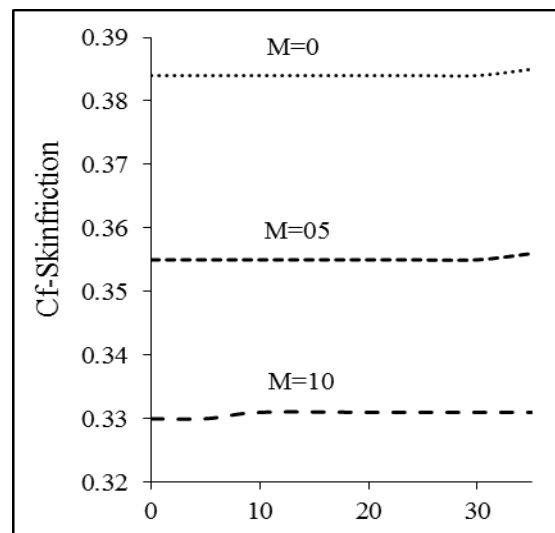

Fig. 15(a). Ec-Viscous dissipation

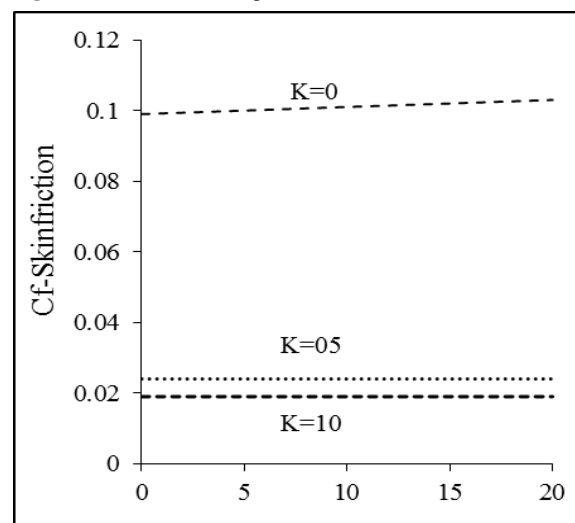**Fig. 15(b).** Ec-Viscous dissipation

Fig. 15(c). Ec-Viscous dissipation

Conclusions

In this paper we have studied fully developed free convection flow heat and mass transfer of a MHD/ micropolar fluid over a vertical channel. The cases of fully developed convection and viscous dispassion effect are investigated. Asymmetric wall temperatures and concentrations are considered.

- The closed form solution proposed in this paper, for fully developed flow, is found to be in excellent agreement with a numerical solution of the time dependent form of the governing equations. Thus, in the range of the governing parameters considered in this study, the solution is steady.

- In general, it is found that upon increasing the vortex viscosity parameter K, the fluid velocity is inhibited. The influence of micro-gyration parameter n, which characterizes the boundary conditions applied on rotation of the microelements near the solid boundaries, on the velocity u and microrotation N profiles is found to be significant. Thus, as n is augmented, the microrotation term is promoted, which induces enhancement of flow velocities.

- The effect of the buoyancy ratio φ on the velocity profiles u and microrotation profiles N is also found to be important. The flow direction in the channel depends strongly on the sign of this parameter. The results presented in this paper illustrate the difference between double diffusion [13] and Soret-induced convection.

- For instance, the rate of flow Q within the channel is found to be independent of the buoyancy ratio φ. This is not the case for double-diffusive convection where Q is observed to depend considerably upon φ. Also the results indicate that, for given values of φ and n, the influence of K on u and N is higher for a = 0 than a = 1. A similar trend is observed for the effect of φ on u and N, for fixed values of K and n.

- The total rate at which heat is added to the fluid is found to be considerably higher for double diffusion than Soret convection. Finally, it must be mentioned that in the case of a = 0 and n = 0 the present results are similar to those reported by Chen [34]. As regards the Soret-induced convection, this flow configuration does not seem, to the best of authors' knowledge, to have been investigated previously.

- For the values of magnetic parameter M = 0, 5, 10, the velocity decreasing up to the position of y=0. At the position of y=4.5 velocity becomes constant that is velocity profiles meet at a point and then cross the side and increasing with magnetic parameter M. It is also found that increase in viscous dissipation parameter (Ec) leads to a corresponding increase in the velocity. It is also seen that the velocity decreases at a certain portion of the channel and then increases; this could be due to the dissipation effect.

- It is found that the increase in viscous dissipation parameter (Ec) leads to a corresponding increase in the temperature profile. It is also seen that the temperature decreases at a certain portion of the channel and then increases; this could be due to the dissipation effect and the harmonic pressure term.

- The Eckert number (Ec) is the ratio of kinetic energy of the flow to the boundary layer enthalpy difference. The effect of Eckert number (Ec) on flow field is to increase the energy, yielding a greater fluid temperature and as a consequence greater buoyancy forces, the increasing on the buoyancy forces due to an increase in the dissipation parameter hence the temperature.

References

[1] A.C. Eringen, "Theory of micropolar fluids, Journal of Mathematics Mechanics", Vol.16, 1966, 1-18.

[2] A.C. Eringen, 'Nonlinear theory of simple micro-elastic solids", International Journal of Engineering Science, Vol.2, 1964, 189–203.

[3] A.C. Eringen, "Theory of thermomicropolar fluids", Journal of Mathematical Analysis and Applications, Vol.38, 1972, 480-496.

[4] I. Papautsky, J. Brazzle, T. Ameel, A.B. Frazier, "Laminar fluid behavior in microchannels using micropolar fluid theory", Sensors Actuators Vol.73, 1999, 101–108.

[5] T. Ariman, M.A. Turk, N.D. Sylvester, "Applications to microcontinuum fluid mechanics a review", International Journal of Science, Vol.12, 1974, 273–293.

[6] G. Lukaszewicz, Micropolar Fluids, "Theory and Applications", Birkhauser, Basel, 1999.

[7] A.J. Chamkha, T. Grosan, I. Pop, "Fully developed free convection of a micropolar fluid in a vertical channel", International Communications of Heat Mass Transfer, Vol.29, 2002, 1119–1127.

[8] J.P. Kumar, J.C. Umavathi, Ali J. Chamkha, I. Pop, "Fully-developed free convection of micropolar and viscous fluids in a vertical channel", Applied Mathematical Modelling, Vol.34, 2010, 1175-1186.

[9] A.S. Bataineh, M.S.M. Noorani, I. Hashim, "Solutions of fully developed free convection of micropolar fluid in a vertical channel by homotopy analysis method", International Journal of Numerical Methods Fluids, Vol.60, 2009, 779–789.

[10] O. Abdulaziz, I. Hashim, "Fully developed free convection heat mass transfer of a micropolar fluid between porous vertical plates", Numerical Heat Transfer Part A-applications, Vol.55, 2009, 270–288.

[11] Nield, D. A, "The thermohaline Rayleigh-Jeffrey's problem", Journal of Fluid Mech, Vol. 29, 1967, 545– 558.

[12] Taunton, J. W., Lightfoot, E. N. & Green. T., "Thermohaline instability and salt fingers in a porous medium", Phys. Fluids, Vol.15, 1972, 748–753.

[13] Poulikakos. D., "Double diffusive convection in a horizontal sparcely packed porous layer", International ommunications of Heat Mass Transfer, Vol.13, 1986, 587–598.

[14] Brand. H. R, Steinberg. V., "Convective instabilities in binary mixtures in a porous medium", Physica A, Vol.119, 1983a, 327–338.

[15] Brand. H. R., Steinberg. V., "Nonlinear effects in the convective instability of a binary mixture in a porous medium near threshold", Physics Letters A, Vol.93A, 1983b, 333–336.

[16] T.L. Bergman, R. Srinivasan, "Numerical simulation of Soret-induced double diffusion in an initially uniform concentration binary fluid", International Journal of Heat Mass Transfer, Vol.32, 1989, 679– 687.

[17] R. Krishnan, "A numerical study of the instability of double-diffusive convection in a square enclosure with horizontal temperature and concentration gradients, heat transfer in convective flows in HTD" ASME National Heat Transfer Conference, Philadelphia, Vol.107, 1989, 357–368.

[18] S. Rawat, R. Bhargava, "Finite element study of natural convection heat and mass transfer in a micropolar fluid-saturated porous regime with Soret/Dufour effect", International Journal of Appl.Math. Mech. Vol.5, 2009, 58–71.

[19] Sunil, P. Chand, A. Mahajan and P. Sharma, "Effect of Rotation on Double-Diffusive Convection in a Magnetized Ferro fluid with Internal Angular Momentum", Journal of Applied Fluid Mechanics, Vol. 4(4), 2011, 43-52.

[20] A. A. Bakr, Z. A. S. Raizahb, "Double-Diffusive Convection-Radiation Interaction on Unsteady MHD Micropolar Fluid Flow over a Vertical Moving Porous Plate with Heat Generation and Soret Effects", Journal of Engineering and Technology, 2012, 19-29.

[21] R. A. Mohamed, "Double-Diffusive Convection-Radiation Interaction on Unsteady MHD Flow over a Vertical Moving Porous Plate with Heat Generation and Soret Effects", Applied Mathematical Sciences, Vol.3, 2009, 629-651.

[22] A. Bahloul, N. Boutana and p. Vasseur, "Double-diffusive and Soret-induced convection in a shallow horizontal porous layer", Journal Fluid Mech, Vol. 491, 2003, 325–352.

[23] Z. Alloui, H. Beji, P. Vasseur, "Double-diffusive and Soret-induced convection of a micropolar fluid in a vertical channel", Computers and Mathematics with Applications Vol.62, 2011, 725-736.

[24] N. Nithyadevi, Ruey-Jen Yang, "Double diffusive natural convection in a partially heated enclosure with Soret and Dufour effects", International Journal of Heat and Fluid Flow Vol.30, 2009, 902–910

[25] Ziya Uddin, Manoj Kumar, "MHD Heat and Mass Transfer Free Convection Flow Near the Lower Stagnation Point of an Isothermal Cylinder Imbedded in Porous Domain with the Presence of Radiation", Jordan Journal of Mechanical and Industrial Engineering, Vol. 5(2), 2011, 133 – 138.

[26] A. Pantokratoras, "Effect of viscous dissipation in natural convection along a heated vertical plate", Applied Mathematical Modelling Vol. 29, 2005, 553–564.

[27] A. K. H. Kabir1, M. A. Alim, L. S. Andallah, "Effects of Viscous Dissipation on MHD Natural Convection Flow along a Vertical Wavy Surface with Heat Generation, American Journal of Computational Mathematics, Vol.3, 2013, 91-98.

[28] Osama Abu-Zeid , H. M. Duwairi, Rebhi A. Damseh, "Viscous and Joule Heating Effects over an Isothermal Cone in Saturated Porous Media, Jordan Journal of Mechanical and Industrial Engineering, Vol.1 (2), 2007, 113-118.

[29] C.Y. Cheng, Fully developed natural convection heat and mass transfer of a micropolar fluid in a vertical channel with asymmetric wall temperatures and concentrations, Int. Commun. Heat Mass Transfer 33, 2006, 627–635.

[30] B. S.Malga, N.Kishan, "Finite element analysis for unsteady MHD heat and mass transfer free convection flow of polar fluids past a vertical moving porous plate in a porous medium with heat generation and thermal diffusion", Journal of Naval Architecture and Marine Engineering Vol.11, 2014, 69-82.

[31] B.Gebhart, "Effect of viscous dissipation in natural convection" Journal of fluid Mechanics, Vol.14 (2), 1962, 225-232.

[32] S.K. Jena, M.N. Mathur, "Similarity solutions for laminar free convection flow of a thermomicropolar fluid past a nonisothermal vertical plate", International Journal of Engrg. Science, Vol.19, 1981, 1431-1439.

[33] J. Peddieson, "An application of the micropolar fluid model to the calculation of a turbulent shear flow", International Journal of Engineering Science, Vol.10, 1972, 23-32.

Reliability Modelling of a Computer System with Priority to H/W Repair over Replacement of H/W and Up-gradation of S/W Subject to MOT and MRT

Ashish Kumar[*a] , S.C.Malik[b]

aDepartment of Mathematics, Manipal University, Jaipur-303007, Rajasthan (India)

bDepartment of Statistics, M.D. University, Rohtak-124001, Haryana (India)

Abstract

In the present paper, some reliability measures of a computer system of two cold standby identical units are obtained using a semi-Markov process and a regenerative point technique. For this purpose, a reliability model is proposed by considering independent h/w and s/w failure. Initially, one unit is operative and another is kept as spare in cold standby. A single server is provided to conduct preventive maintenance, repair, replacement and up-gradation of the components upon their failure. Then, a maximum operation time system undergoes preventive maintenance, directly from normal mode. If the repair of the h/w is not possible by the server up to a pre-specific time, it is replaced by a new one with some replacement time. However, only up-gradation of the software by a new one is made whenever s/w fails to execute the desired function properly. Priority to h/w repair is given over h/w replacement and s/w up-gradation. The failure time distribution of the h/w and s/w follows a negative exponential while the distributions of preventive maintenance, repair, up-gradation and replacement time are taken as arbitrary with different probability density functions. To depict the importance of the study, graphs are drawn for a particular case with fixed values of other parameters and costs.

Nomenclature

E	The set of regenerative states
NO	The unit is operative and in normal mode
Cs	The unit is cold standby
a/b	Probability that the system has hardware / software failure
λ_1/λ_2	Constant hardware / software failure rate
α_0	Maximum Operation Time
β_0	Maximum Repair Time.
Pm/PM	The unit is under preventive Maintenance/ under preventive maintenance continuously from previous state
WPm/WPM	The unit is waiting for preventive Maintenance/ waiting for preventive maintenance from previous state
HFur/HFUR	The unit is failed due to hardware and is under repair / under repair continuously from previous state

HFurp/HFURP	The unit is failed due to hardware and is under replacement / under replacement continuously from previous state
HFwr / HFWR	The unit is failed due to hardware and is waiting for repair/ waiting for repair continuously from previous state
SFurp/SFURP	The unit is failed due to the software and is under up-gradation/ under up-gradation continuously from previous state
SFwrp/SFWRP	The unit is failed due to the software and is waiting for up-gradation / waiting for up-gradation continuously from previous state
h(t) / H(t)	pdf / cdf of up-gradation time of unit due to software
g(t) / G(t)	pdf / cdf of repair time of the hardware
m(t)/ M(t)	pdf / cdf of replacement time of the hardware
f(t) / F(t)	pdf / cdf of the time for PM of the unit
pdf / cdf	Probability density function/ Cumulative density function

---

[*] Corresponding author. e-mail: ashishbarak2020@gmail.com.

$q_{ij}(t)/$ $Q_{ij}(t)$	pdf / cdf of passage time from regenerative state i to a regenerative state j or to a failed state j without visiting any other regenerative state in (0, t]
$q_{ij.kr}$ (t)/$Q_{ij.kr}(t)$	pdf/cdf of direct transition time from regenerative state i to a regenerative state j or to a failed state j visiting state k, r once in (0, t]
$\mu_i(t)$	Probability that the system up initially in state $S_i \in E$ is up at time t without visiting to any regenerative state
$W_i(t)$	Probability that the server is busy in the state Si upto time 't' without making any transition to any other regenerative state or returning to the same state via one or more non-regenerative states.
m_{ij}	Contribution to mean sojourn time (μ_i) in state Si when system transit directly to state Sj so that $\mu_i = \sum_j m_{ij}$ and $m_{ij} = \int t dQ_{ij}(t) = -q_{ij}^{*}{}'(0)$
Ⓢ/©	Symbol for Laplace-Stieltjes convolution/Laplace convolution
~ / *	Symbol for Laplace Steiltjes Transform (LST) / Laplace Transform (LT)

1. Introduction

In our modern society, there is an increased reliance on computer systems due to the rise of technology in everyday life. These systems control everything from banking to telecommunications, to nuclear power plants, to air traffic. Their failure can be catastrophic. Therefore, ensuring the reliability and performance of such systems has become a growing need for engineers and academicians. Currently, redundancy is one of the best methods of improving the reliability of any operating system. During the past few years, some reliability models of computer systems with independent h/w and s/w failures have been suggested by some researchers, including Malik and Anand [1] and Malik and Kumar [3].

Also, it is a well known fact that preventive maintenance can slow down the deterioration process of a computer system and restore the system as new. Thus, the method of preventive maintenance can be used to improve the reliability and the profit of the system. The concept of preventive maintenance was used by Malik and Nandal [2] while discussing a cold standby system with a maximum operation time. Also, it sometimes becomes necessary to give priority to repairing one unit over the repair activities of another unit, not only to reduce the down time but also to minimize the operating cost. Malik *et al.* [4,5] analyzed stochastically a computer system with priority to h/w

repair over s/w replacement. Kumar *et al.* [6] developed a stochastic model for a computer system using the concept of s/w up-gradation over h/w repair activities. Furthermore, the reliability and availability of a system can be increased by making a replacement of the failed component by a new one in case the repair time is too long. Recently, Kumar *et al.* [4,5] proposed a reliability model for a computer system with preventive maintenance and repair subject to maximum operation and repair times.

In light of the above facts and practical utility, here is a reliability model proposed taking into account the independent h/w and s/w failure. Initially, one unit is operative and the other is kept as spare in cold standby. A single server is provided to conduct preventive maintenance, repair, up-gradation and a replacement of the components upon their failure. After that, a maximum operation time system undergoes preventive maintenance directly from the normal mode. If the repair of the h/w is not possible by the server up to a pre-specific time, it is replaced by a new one with some replacement time. However, only up-gradation of the software by new one is made whenever s/w fails to execute the desired function properly. Priority to h/w repair is given over h/w replacement and s/w up-gradation. The failure time h/w and s/w follows exponential distribution while the distributions of preventive maintenance, repair, up-gradation and replacement time are taken as arbitrary with different probability density functions. Various system effectiveness measures, such as mean time to system failure, availability, busy period of the server due to preventive maintenance, busy period of the server due to repair, busy period of the server due to hardware replacement, busy period of the server due to software up-gradation, expected number of software up-gradations, expected number of hardware replacement and expected number of visits of the server are derived by using semi-Markov process and regenerative point technique. All random variables are statistically independent and uncorrelated. Switch devices are perfect. The graphical study of the results for a particular case has also been made to highlight the importance of the results.

2. Transition Probabilities and Mean Sojourn Times

Simple probabilistic considerations yield the following expressions by taking A $= a\lambda_1 + b\lambda_2 + \alpha_0$, B$= a\lambda_1 + b\lambda_2 + \alpha_0 + \beta_0$ for the non-zero elements

$$p_{ij} = Q_{ij}(\infty) = \int_0^\infty q_{ij}(t)dt \quad \text{as} \tag{1}$$

$$p_{16} = \frac{a\lambda_1}{a\lambda_1 + b\lambda_2 + \alpha_0} [\,1 - f^*(a\lambda_1 + b\lambda_2 + \alpha_0)] = p_{12.6},$$

$$p_{02} = \frac{a\lambda_1}{a\lambda_1 + b\lambda_2 + \alpha_0},$$

$$p_{18} = \frac{b\lambda_2}{a\lambda_1 + b\lambda_2 + \alpha_0} [\,1 - f^*(a\lambda_1 + b\lambda_2 + \alpha_0)] = p_{13.8},$$

$$p_{01} = \frac{\alpha_0}{a\lambda_1 + b\lambda_2 + \alpha_0},$$

$$p_{1.13} = \frac{\alpha_0}{a\lambda_1 + b\lambda_2 + \alpha_0} [\,1 - f^*(a\lambda_1 + b\lambda_2 + \alpha_0)] = p_{11.13},$$

$$p_{03} = \frac{b\lambda_2}{a\lambda_1 + b\lambda_2 + \alpha_0},$$

$$p_{24} = \frac{\beta_0}{a\lambda_1 + b\lambda_2 + \alpha_0 + \beta_0} [\,1 - g^*(a\lambda_1 + b\lambda_2 + \alpha_0 + \beta_0)],$$

$$p_{10} = f^*(a\lambda_1 + b\lambda_2 + \alpha_0),$$

$$p_{25} = \frac{\alpha_0}{a\lambda_1 + b\lambda_2 + \alpha_0 + \beta_0}[1 - g^*(a\lambda_1 + b\lambda_2 + \alpha_0 + \beta_0)], \qquad p_{20} = g^*(a\lambda_1 + b\lambda_2 + \alpha_0 + \beta_0),$$

$$p_{2.11} = \frac{b\lambda_2}{a\lambda_1 + b\lambda_2 + \alpha_0 + \beta_0}[1 - g^*(a\lambda_1 + b\lambda_2 + \alpha_0 + \beta_0)], \qquad p_{30} = h^*(a\lambda_1 + b\lambda_2 + \alpha_0),$$

$$p_{2.12} = \frac{a\lambda_1}{a\lambda_1 + b\lambda_2 + \alpha_0 + \beta_0}[1 - g^*(a\lambda_1 + b\lambda_2 + \alpha_0 + \beta_0)], \qquad p_{40} = m^*(a\lambda_1 + b\lambda_2 + \alpha_0),$$

$$p_{37} = \frac{a\lambda_1}{a\lambda_1 + b\lambda_2 + \alpha_0}[1 - h^*(a\lambda_1 + b\lambda_2 + \alpha_0)], \qquad p_{51} = g^*(\beta_0),\ p_{5,16} = 1 - g^*(\beta_0),$$

$$p_{39} = \frac{\alpha_0}{a\lambda_1 + b\lambda_2 + \alpha_0}[1 - h^*(a\lambda_1 + b\lambda_2 + \alpha_0)] = p_{3,1.9}, \qquad p_{62} = f^*(0),\quad p_{73} = g^*(0),$$

$$p_{3,10} = \frac{b\lambda_2}{a\lambda_1 + b\lambda_2 + \alpha_0}[1 - h^*(a\lambda_1 + b\lambda_2 + \alpha_0)] = p_{33.10}, \qquad p_{83} = f^*(0),\ p_{93} = f^*(0),$$

$$p_{4.17} = \frac{\alpha_0}{a\lambda_1 + b\lambda_2 + \alpha_0}[1 - m^*(a\lambda_1 + b\lambda_2 + \alpha_0)] = p_{4,1.17}, \qquad p_{10.3} = h^*(0),\quad p_{11.3} = g^*(\beta_0),$$

$$p_{4.18} = \frac{b\lambda_2}{a\lambda_1 + b\lambda_2 + \alpha_0}[1 - m^*(a\lambda_1 + b\lambda_2 + \alpha_0)] = p_{43.18}, \qquad p_{11.14} = 1 - g^*(\beta_0),\ p_{14.3} = m^*(0),$$

$$p_{4.19} = \frac{a\lambda_1}{a\lambda_1 + b\lambda_2 + \alpha_0}[1 - m^*(a\lambda_1 + b\lambda_2 + \alpha_0)], \qquad p_{15.2} = m^*(0),\ p_{16.1} = m^*(0),$$

$$p_{21.5} = \frac{\alpha_0}{a\lambda_1 + b\lambda_2 + \alpha_0 + \beta_0}[1 - g^*(a\lambda_1 + b\lambda_2 + \alpha_0 + \beta_0)]\, g^*(\beta_0), \qquad p_{12.2} = g^*(\beta_0),\ p_{13.1} = f^*(0),$$

$$p_{21.16,5} = \frac{\alpha_0}{a\lambda_1 + b\lambda_2 + \alpha_0 + \beta_0}[1 - g^*(a\lambda_1 + b\lambda_2 + \alpha_0 + \beta_0)][1 - g^*(\beta_0)], \quad p_{17.1} = m^*(0),$$

$$p_{23.11} = \frac{b\lambda_2}{a\lambda_1 + b\lambda_2 + \alpha_0 + \beta_0}[1 - g^*(a\lambda_1 + b\lambda_2 + \alpha_0 + \beta_0)][g^*(\beta_0)], \qquad p_{18.3} = m^*(0),$$

$$p_{23.11,14} = \frac{b\lambda_2}{a\lambda_1 + b\lambda_2 + \alpha_0 + \beta_0}[1 - g^*(a\lambda_1 + b\lambda_2 + \alpha_0 + \beta_0)][1 - g^*(\beta_0)], \quad p_{19.4} = g^*(0),$$

$$p_{22.12} = \frac{a\lambda_1}{a\lambda_1 + b\lambda_2 + \alpha_0 + \beta_0}[1 - g^*(a\lambda_1 + b\lambda_2 + \alpha_0 + \beta_0)]\, g^*(\beta_0), \qquad p_{12.15} = 1 - g^*(\beta_0),$$

$$p_{22.12,15} = \frac{a\lambda_1}{a\lambda_1 + b\lambda_2 + \alpha_0 + \beta_0}[1 - g^*(a\lambda_1 + b\lambda_2 + \alpha_0 + \beta_0)][1 - g^*(\beta_0)] \tag{2}$$

It can be easily verified that

$$p_{01} + p_{02} + p_{03} = p_{10} + p_{16} + p_{18} + p_{1.13} = 1$$

$$p_{20} + p_{24} + p_{25} + p_{2,11} + p_{2.12} = p_{30} + p_{37} + p_{39} + p_{3.10} = 1$$

$$p_{40} + p_{4.17} + p_{4.18} + p_{4.19} = p_{5.1} + p_{5.16} = p_{62} = p_{73} = p_{83} = p_{91} = 1$$

$$p_{10.3} = p_{11.3} + p_{11.14} = p_{12.2} + p_{12.15} = p_{13.1} = p_{14.1} = p_{15.2} = 1 \tag{3}$$

$$p_{16.1} = p_{17.1} = p_{18.3} = p_{19.4} = p_{10} + p_{12.6} + p_{11.13} + p_{13.8} = 1$$

$$p_{20} + p_{24} + p_{21.5} + p_{21,16.5} + p_{23,11} + p_{23.11,14} + p_{22,12} + p_{22.12,15} = 1$$

$$p_{30} + p_{31.9} + p_{32.7} + p_{33.10} = p_{40} + p_{41.17} + p_{42.19} + p_{43.18} = 1$$

The mean sojourn times (μ_i) is the state S_i are

$$\mu_0 = \frac{1}{(a\lambda_1 + b\lambda_2 + \alpha_0)} , \qquad \mu_1 = \frac{1}{(a\lambda_1 + b\lambda_2 + \alpha_0 + \alpha)} ,$$

$$\mu_2 = \frac{1}{a\lambda_1 + b\lambda_2 + \alpha_0 + \theta + \beta_0} , \qquad \mu_3 = \frac{1}{a\lambda_1 + b\lambda_2 + \alpha_0 + \beta} ,$$

$$\mu_3' = \frac{\beta^2 + a\lambda_1\beta + (b\lambda_2 + \alpha_0)(a\lambda_1 + b\lambda_2 + \alpha_0)}{\beta(a\lambda_1 + b\lambda_2 + \alpha_0 + \theta + \beta_0)^2} , \qquad \mu_4 = \frac{1}{a\lambda_1 + b\lambda_2 + \alpha_0 + \gamma} , \qquad (4)$$

$$\mu_4' = \frac{\gamma^2 + a\lambda_1\gamma + (b\lambda_2 + \alpha_0)(a\lambda_1 + b\lambda_2 + \alpha_0)}{\gamma(a\lambda_1 + b\lambda_2 + \alpha_0 + \theta + \beta_0)^2} , \qquad \mu_1' = \frac{1}{\alpha} , \qquad \mu_{19} = \frac{1}{\theta} ,$$

$$\mu_2' = \frac{(\beta_0 + \theta)}{(B + \theta)^2} + \frac{(A)\{-\theta^2\gamma(\theta + \beta_0)^2 + \gamma\theta(B) + \beta_0(\beta_0 + \theta)(\theta + B)(B)}{\gamma(\theta + B)^2(\theta + \beta_0)^2(B)} ,$$

$$\mu_7 = \frac{1}{\theta}$$

3. Reliability and Mean Time to System Failure (MTSF)

Let $\phi_i(t)$ be the c.d.f of first passage time from the regenerative state i to a failed state. Regarding the failed state as absorbing state, we have the following recursive relation for $\phi_i(t)$:

$$\phi_i(t) = \sum_j Q_{i,j}(t) \circledS \phi_j(t) + \sum_k Q_{i,k}(t) \qquad (5)$$

Where j is an un-failed regenerative state to which the given regenerative state i can transit and k is a failed state to which the state i can transit directly.

Taking LT of the above relation (5) and solving for $\tilde{\phi}_0(s)$.

We have

$$R^*(s) = \frac{1 - \tilde{\phi}_0(s)}{s} \qquad (6)$$

The reliability of the system model can be obtained by taking Laplace inverse transform of (7). The mean time to system failure (MTSF) is given by

$$\text{MTSF} = \lim_{s \to o} \frac{1 - \tilde{\phi}_0(s)}{s} = \frac{N_1}{D_1} \qquad (7)$$

Where
$$N_1 = \mu_0 + p_{01}\mu_1 + p_{02}\mu_2 + p_{03}\mu_3 + p_{24}p_{02}\mu_4$$
And $D_1 = 1 - p_{01}p_{10} - p_{02}p_{20} - p_{03}p_{30} - p_{02}p_{24}p_{40}$

4. Steady State Availability

Let $A_i(t)$ be the probability that the system is in up-state at instant 't' given that the system entered regenerative state i at t = 0. The recursive relations for $A_i(t)$ are given as

$$A_i(t) = M_i(t) + \sum_j q_{i,j}^{(n)}(t) \copyright A_j(t) \qquad (8)$$

where j is any successive regenerative state to which the regenerative state i can transit through n transitions. $M_i(t)$ is the probability that the system is up initially in state $S_i \in E$ is up at time t without visiting to any other regenerative state, we have

$$M_0(t) = e^{-(a\lambda_1 + b\lambda_2 + \alpha_0)t} ,$$
$$M_1(t) = e^{-(a\lambda_1 + b\lambda_2 + \alpha_0)t} \overline{F(t)} ,$$
$$M_2(t) = e^{-(a\lambda_1 + b\lambda_2 + \alpha_0 + \beta_0)t} \overline{G(t)} \qquad (9)$$
$$M_3(t) = e^{-(a\lambda_1 + b\lambda_2 + \alpha_0)t} \overline{H(t)} ,$$
$$M_4(t) = e^{-(a\lambda_1 + b\lambda_2 + \alpha_0)t} \overline{M(t)}$$

Taking LT of the above relations (8) and solving for $A_0^*(s)$, the steady state availability is given by

$$A_0(\infty) = \lim_{s \to 0} s A_0^*(s) = \frac{N_2}{D_2}, \quad \text{Where} \tag{10}$$

$N_2 = (-p_{24})\{\mu_0 \{p_{12.6}[p_{43.18}p_{31.9}+p_{41.17}(1-p_{33.10}-p_{37}p_{73})]\}- \mu_1 [p_{02}\{p_{43.18}p_{31.9}+(1-p_{33.10}-p_{37}p_{73})p_{41.17}\}]+ \mu_3 [-p_{01} p_{43.18} p_{12.6+} p_{03} p_{41.17} p_{12.6}- p_{02}\{p_{43.18}(1-p_{11.13})+p_{41.17}p_{13.8}\}]+\mu_4 [p_{01}(1-p_{33.10}-p_{37}p_{73})p_{12.6}+p_{02}\{(1-p_{11.13})(1-p_{33.10}-p_{37}p_{73})-p_{13.8}p_{31.9}\}+p_{03}p_{31.9}p_{12.6}]\}+(1-p_{4.19}p_{19.4})\{\mu_0 [(1_-p_{11.13})(1-p_{33.10}-p_{37}p_{73})(1-p_{22.12}-p_{22.12.15})-p_{12.6}\{(1-p_{33.10}-p_{37}p_{73})(p_{21.5}+p_{21.5,16})+(p_{23.11}+p_{23.11.14})p_{31.9}\}-p_{13.8}(1-p_{22.12}-p_{22.12.15})p_{31.9}]+\mu_1[p_{01}[(1-p_{33.10}-p_{37}p_{73})(1-p_{22.12}-p_{22.12.15})+p_{02}\{(1-p_{33.10}-p_{37}p_{73})(p_{21.5}+p_{21.5,16})+(p_{23.11}+p_{23.11.14})p_{31.9}\}+p_{03}(1-p_{22.12}-p_{22.12.15})p_{31.9}]+\mu_2[p_{01}\{(1-p_{33.10}-p_{37}p_{73})p_{12.6}+p_{02}\{(1-p_{11.13})(1-p_{33.10}-p_{37}p_{73})-p_{13.8}p_{31.9}\}+p_{03}p_{31.9}p_{12.6}]+\mu_3[p_{01}[p_{13.8}(1-p_{22.12}-p_{22.12.15})+(p_{23.11}+p_{23.11.14})p_{12.6}]+p_{02}\{(p_{21.5}+p_{21.5,16})p_{13.8}+(1-p_{11.13})(p_{23.11}+p_{23.11.14})\}+p_{03}\{-p_{12.6}(p_{21.5}+p_{21.5,16})+(1-p_{22.12}-p_{22.12.15})(1-p_{11.13})\}]\}$

And

$D_2 =(-p_{24})\{\mu_0 \{p_{12.6}[p_{43.18}p_{31.9}+p_{41.17}(1-p_{33.10}-p_{37}p_{73})]\}- \mu_1' [p_{02}\{p_{43.18}p_{31.9}+(1-p_{33.10}-p_{37}p_{73})p_{41.17}\}]+ (\mu_3'+p_{37}\mu_7)[-p_{01} p_{43.18} p_{12.6+} p_{03} p_{41.17} p_{12.6}- p_{02}\{p_{43.18}(1-p_{11.13})+p_{41.17}p_{13.8}\}]+(\mu_4'+p_{4.19}\mu_{19})[p_{01}(1-p_{33.10}-p_{37}p_{73})p_{12.6}+p_{02}\{(1_-p_{11.13})(1-p_{33.10}-p_{37}p_{73})-p_{13.8}p_{31.9}\}+p_{03}p_{31.9}p_{12.6}]\}+(1-p_{4.19}p_{19.4})\{\mu_0 [(1-p_{11.13})(1-p_{33.10}-p_{37}p_{73})(1-p_{22.12}-p_{22.12.15})-p_{12.6}\{(1-p_{33.10}-p_{37}p_{73})(p_{21.5}+p_{21.5,16})+(p_{23.11}+p_{23.11.14})p_{31.9}\}-p_{13.8}(1-p_{22.12}-p_{22.12.15})p_{31.9}]+\mu_1'[p_{01}[(1-p_{33.10}-p_{37}p_{73})(1-p_{22.12}-p_{22.12.15})+p_{02}\{(1-p_{33.10}-p_{37}p_{73})(p_{21.5}+p_{21.5,16})+(p_{23.11}+p_{23.11.14})p_{31.9}\}+p_{03}(1-p_{22.12}-p_{22.12.15})p_{31.9}]+\mu_2'[p_{01}\{(1-p_{33.10}-p_{37}p_{73})p_{12.6}+p_{02}\{(1-p_{11.13})(1-p_{33.10}-p_{37}p_{73})-p_{13.8}p_{31.9}\}+p_{03}p_{31.9}p_{12.6}]+(\mu_3'+p_{37}\mu_7)[p_{01}[p_{13.8}(1-p_{22.12}-p_{22.12.15})+(p_{23.11}+p_{23.11.14})p_{12.6}]+p_{02}\{(p_{21.5}+p_{21.5,16})p_{13.8}+(1-p_{11.13})(p_{23.11}+p_{23.11.14})\}+p_{03}\{-p_{12.6}(p_{21.5}+p_{21.5,16})+(1-p_{22.12}-p_{22.12.15})(1-p_{11.13})\}]\}$

5. Busy Period Analysis for Server

5.1. Due to Preventive Maintenance (PM)

Let $B_i^P(t)$ be the probability that the server is busy in the preventive maintenance of the unit at an instant 't' given that the system entered state i at t = 0. The recursive relations $B_i^P(t)$ for are as follows:

$$B_i^p(t) = W_i(t) + \sum_j q_{i,j}^{(n)}(t) \copyright B_j^p(t) \tag{12}$$

Where j is any successive regenerative state to which the regenerative state i can transit through n transitions. $W_1(t)$ is the probability that the server is busy in state S_i due to the preventive maintenance up to time t without making any transition to any other regenerative state or returning to the same via one or more non-regenerative states and so

$$W_1 = e^{-(a\lambda_1 + b\lambda_2 + \alpha_0)t}\overline{F}(t) + (\alpha_0 e^{-(a\lambda_1 + b\lambda_2 + \alpha_0)t}\copyright 1)\overline{F}(t) + (a\lambda_1 e^{-(a\lambda_1 + b\lambda_2 + \alpha_0)t})\overline{F}(t) + (b\lambda_2 e^{-(a\lambda_1 + b\lambda_2 + \alpha_0)t}\copyright 1)\overline{F}(t)$$

5.2. Due to Hardware Failure

Let $B_i^R(t)$ be the probability that the server is busy in repairing the unit due to hardware failure at an instant 't' given that the system entered state i at t = 0. The recursive relations for $B_i^R(t)$ are as follows:

$$B_i^R(t) = W_i(t) + \sum_j q_{i,j}^{(n)}(t) \copyright B_j^R(t) \tag{13}$$

where j is any successive regenerative state to which the regenerative state i can transit through n transitions. $W_2(t)$ is the probability that the server is busy in state S_i due to hardware failure up to time t without making any transition to any other regenerative state or returning to the same via one or more non-regenerative states and so

$$W_2 = e^{-(a\lambda_1 + b\lambda_2 + \alpha_0)t}\overline{G}(t) + (\alpha_0 e^{-(a\lambda_1 + b\lambda_2 + \alpha_0)t}\copyright 1)\overline{G}(t) + (a\lambda_1 e^{-(a\lambda_1 + b\lambda_2 + \alpha_0)t})\overline{G}(t) + (b\lambda_2 e^{-(a\lambda_1 + b\lambda_2 + \alpha_0)t}\copyright 1)\overline{G}(t)$$

5.3. Due to Up-Gradation of the Software

Let $B_i^S(t)$ be the probability that the server is busy due to up-gradation of the software at an instant 't' given that the system entered the regenerative state i at t = 0. We have the following recursive relations for $B_i^S(t)$:

$$B_i^S(t) = W_i(t) + \sum_j q_{i,j}^{(n)}(t) \copyright B_j^S(t) \tag{14}$$

Where j is any successive regenerative state to which the regenerative state i can transit through n transitions. $W_3(t)$ is the probability that the server is busy in state S_i due to up-gradation of the software up to time t without making any transition to any other regenerative state or returning to the same via one or more non-regenerative states and so

$$W_3 = e^{-(a\lambda_1 + b\lambda_2 + \alpha_0)t}\overline{H}(t) + (\alpha_0 e^{-(a\lambda_1 + b\lambda_2 + \alpha_0)t}\copyright 1)\overline{H}(t) + (a\lambda_1 e^{-(a\lambda_1 + b\lambda_2 + \alpha_0)t})\overline{H}(t) + (b\lambda_2 e^{-(a\lambda_1 + b\lambda_2 + \alpha_0)t}\copyright 1)\overline{H}(t)$$

5.4. Due to Hardware Replacement

Let $B_i^{HRp}(t)$ be the probability that the server is busy in replacement of the unit due to hardware failure at an instant 't' given that the system entered state i at t = 0. The recursive relations for $B_i^{HRp}(t)$ are as follows:

$$B_i^{HRp}(t) = W_i(t) + \sum_j q_{i,j}^{(n)}(t) \copyright B_j^{HRp}(t) \tag{15}$$

Where j is any successive regenerative state to which the regenerative state i can transit through n transitions. $W_4(t)$ is the probability that the server is busy in state S_i due to hardware failure up to time t without making any transition to any other regenerative state or returning to the same via one or more non-regenerative states and so

$$W_4 = e^{-(a\lambda_1 + b\lambda_2 + \alpha_0)t}\overline{M}(t) + (\alpha_0 e^{-(a\lambda_1 + b\lambda_2 + \alpha_0)t}\copyright 1)\overline{M}(t) + (a\lambda_1 e^{-(a\lambda_1 + b\lambda_2 + \alpha_0)t})\overline{M}(t) + (b\lambda_2 e^{-(a\lambda_1 + b\lambda_2 + \alpha_0)t}\copyright 1)\overline{M}(t)$$

Taking the LT of the above relations (12) to (15), and solving for $B_0^{*^H}$ (s) and $B_0^{*^S}$ (s), the time for which server is busy due to repair and replacements, respectively, is given by

$$B_0^H = \lim_{s \to 0} s B_0^{*H}(s) = \frac{N_3^H}{D_2} \qquad\qquad B_0^R = \lim_{s \to 0} s B_0^{*R}(S) = \frac{N_S^R}{D_2} \qquad (16)$$

$$B_0^S = \lim_{s \to 0} s B_0^{*S}(s) = \frac{N_3^S}{D_2} \qquad\qquad B_0^{HRp} = \lim_{s \to 0} s B_0^{*HRp}(S) = \frac{N_S^{HRp}}{D_2}$$

$$\begin{aligned}
N_3^P = {}& W_1^*(0)\{p_{24}p_{02}[p_{31.9}p_{43.18} + p_{41.17}(1\text{-}p_{33.10} - p_{37}p_{73})]\} + \\
& (1 - p_{4.19}p_{19.4})[p_{01}(1 - p_{33.10} - p_{37}p_{73})(1 - p_{22.12} - p_{22.12,15}) + \\
& p_{02}\{(p_{23.11} + p_{23.11,14})p_{31.9} + (1 - p_{33.10} - p_{37}p_{73})(p_{21.5} + p_{21.5.15})\} \\
& + p_{03}\{(1 - p_{22.12} - p_{22.12,15})p_{31.9}\}]
\end{aligned}$$

$$\begin{aligned}
N_3^R = {}& p_{24}[W_7^*(0)p_{37}[p_{01}p_{12.6}p_{43.18} - p_{41.17}p_{03}p_{12.6} + p_{02}\{(1-p_{11.13})p_{43.18} \\
& + p_{41.17}p_{13.8}\}] + W_{19}^*(0)p_{4.19}\{p_{01}(1 - p_{33.10} - p_{37}p_{73})p_{12.6} + p_{02} \\
& \{(1_-p_{11.13})(1 - p_{33.10} - p_{37}p_{73}) - p_{13.8}p_{31.9}\} + p_{03}p_{31.9}p_{12.6}\}] \\
& + (1 - p_{4.19}p_{19.4})[W_2^*(0)\{p_{01}(1 - p_{33.10} - p_{37}p_{73})p_{12.6} + p_{02} \\
& \{(1-p_{11.13})(1 - p_{33.10} - p_{37}p_{73}) - p_{13.8}p_{31.9}\} + p_{03}p_{31.9}p_{12.6}\} \\
& + W_7^*(0)p_{37}[p_{01}[p_{13.8}(1 - p_{22.12} - p_{22.12,15}) + (p_{23.11} + p_{23.11,14}) \\
& p_{12.6}] + p_{02}\{(1 - p_{11.13})(p_{23.11} + p_{23.11,14}) + p_{13.8}(p_{21.5} + p_{21.5.15})\} + \\
& p_{03}\{(1 - p_{22.12} - p_{22.12,15})(1 - p_{11.13}) - p_{12.6}(p_{21.5} + p_{21.5.15})\}]
\end{aligned}$$

$$\begin{aligned}
N_3^S = {}& W_3^*(0)[p_{24}\{p_{01}p_{43.18}p_{12.6} - p_{03}p_{41.17}p_{12.6} + p_{02}\{(1-p_{11.13})p_{43.18} + p_{41.17}p_{13.8}\}] + \\
& (1 - p_{4.19}p_{19.4})\{p_{01}[p_{13.8}(1 - p_{22.12} - p_{22.12,15}) + (p_{23.11} + p_{23.11,14}) \\
& p_{12.6}] + p_{02}\{(1 - p_{11.13})(p_{23.11} + p_{23.11,14}) + p_{13.8}(p_{21.5} + p_{21.5.15})\} + \\
& p_{03}\{(1 - p_{22.12} - p_{22.12,15})(1 - p_{11.13}) - p_{12.6}(p_{21.5} + p_{21.5.15})\}]
\end{aligned}$$

$$\begin{aligned}
N_3^{HRp} = {}& W_4^* p_{24}[p_{01}(1 - p_{33.10} - p_{37}p_{73})p_{12.6} + p_{02}\{(1 - p_{33.10} - p_{37}p_{73})(1 - p_{11.13}) - p_{13.8}p_{31.9})\} \\
& + p_{03}p_{12.6}p_{31.9}] \text{ and D2 is already mentioned.}
\end{aligned}$$

6. Expected Number of H/W Replacements and S/W Up-Gradations

6.1. Due to Hardware Failure

Let $R_i^H(t)$ be the expected number of replacements of the failed hardware components by the server in (0, t] given that the system entered the regenerative state i at t = 0. The recursive relations for $R_i^H(t)$ are given as

$$R_i^H(t) = \sum_j q_{i,j}^{(n)}(t) \circledS \left[\delta_j + R_j^H(t) \right] \qquad (17)$$

Where j is any regenerative state to which the given regenerative state i transits and $\delta j = 1$, if j is the regenerative state where the server does the job afresh, otherwise $\delta j = 0$.

6.2. Due to Software Failure

Let $R_i^S(t)$ be the expected number of up-gradations of the failed software by the server in (0, t] given that the system entered the regenerative state i at t = 0. The recursive relations for $R_i^S(t)$ are given as

$$R_i^S(t) = \sum_j q_{i,j}^{(n)}(t) \circledS \left[\delta_j + R_j^S(t) \right] \qquad (18)$$

Where j is any regenerative state to which the given regenerative state i transits and $\delta j = 1$, if j is the regenerative state where the server does job afresh, otherwise $\delta j = 0$. Taking LT of the relations (17) and (18), and solving for $\tilde{R}_0^H(s)$ and $\tilde{R}_0^S(s)$. The expected numbers of replacements per unit time to the hardware and software failures are respectively given by

$$R_0^H(\infty) = \lim_{s \to 0} s \tilde{R}_0^H(s) = \frac{N_4^H}{D_2}$$

and $\qquad\qquad\qquad\qquad\qquad\qquad (19)$

$$R_0^S(\infty) = \lim_{s \to 0} s \tilde{R}_0^S(s) = \frac{N_4^S}{D_2}$$

Where D$_2$ is already mentioned.

$$N_4^H = (p_{40} + p_{41.17} + p_{43.18})(p_{24})\{p_{01}(1 - p_{33.10} - p_{37}p_{73})p_{12.6} + p_{02}$$
$$[(1 - p_{11.13})(1 - p_{33.10} - p_{37}p_{73}) - p_{31.9}p_{13.8}] + p_{03}p_{31.9}p_{12.6}\}$$
$$+ (p_{22.12,15} + p_{21.5,16} + p_{23.11,14})(1 - p_{19.4}p_{4.19})\{p_{01}(1 - p_{33.10} - p_{37}p_{73})p_{12.6} + p_{02}$$
$$[(1 - p_{11.13})(1 - p_{33.10} - p_{37}p_{73}) - p_{31.9}p_{13.8}] + p_{03}p_{31.9}p_{12.6}\}$$

$$N_4^S = (p_{30} + p_{33.10} + p_{31.9})[(p_{24})\{[p_{01}p_{43.18}p_{12.6} - p_{03}p_{41.17}p_{12.6} + p_{02}\{(1-p_{11.13})p_{43.18} - p_{41.17}p_{13.8}\}]$$
$$+ (1 - p_{19.4}p_{4.19})\{p_{01}[p_{13.8}(1 - p_{22.12} - p_{22.12,15}) + (p_{23.11} + p_{23.11,14})$$
$$p_{12.6}] + p_{02}\{(1 - p_{11.13})(p_{23.11} + p_{23.11,14}) + p_{13.8}(p_{21.5} + p_{21.5,16})\}$$
$$+ p_{03}\{(1 - p_{22.12} - p_{22.12,15})(1 - p_{11.13}) - p_{12.6}(p_{21.5} + p_{21.5,16})\}]]$$

7. Expected Number of Visits by the Server

Let $N_i(t)$ be the expected number of visits by the server in (0, t] given that the system entered the regenerative state i at t = 0. The recursive relations for $N_i(t)$ are given as

$$N_i(t) = \sum_j q_{i,j}^{(n)}(t) \circledS [\delta_j + N_j(t)] \qquad (20)$$

Where j is any regenerative state to which the given regenerative state i transits and $\delta j = 1$, if j is the regenerative state where the server does the job afresh, otherwise $\delta j = 0$. Taking LT of the relation (20) and solving for $\tilde{N}_0(s)$. The expected number of visit per unit time by the server are given by

$$N_0(\infty) = \lim_{s \to 0} s\tilde{N}_0(s) = \frac{N_5}{D_2}, \text{ where} \qquad (21)$$

$N_5 = (-p_{24}) p_{12.6}\{ p_{43.18}p_{31.9} + (1 - p_{33.10})p_{41.17}\} + (1 - p_{4.19}p_{19.4})$
$[(1 - p_{11.13}) (1 - p_{33.10} - p_{37}p_{73}) (1 - p_{22.12} - p_{22.12.15}) - p_{12.6} \{$
$(p_{21.5} + p_{21.5.16})(1 - p_{33.10} - p_{37}p_{73}) + p_{31.9} (p_{23.11} + p_{23.11,14}) \} -$
$p_{13.8}p_{31.9} (1 - p_{22.12} - p_{22.12.15})]$

8. Profit Analysis

The profit incurred to the system model in a steady state can be obtained as

$$P = K_0 A_0 - K_1 B_0^P - K_2 B_0^R - K_3 B_0^S -$$
$$K_4 B_0^{HRp} - K_5 R_0^H - K_6 R_0^S - K_7 N_0 \qquad (22)$$

K_0 = Revenue per unit up-time of the system
K_1 = Cost per unit time for which server is busy due preventive maintenance
K_2 = Cost per unit time for which server is busy due to hardware failure
K_3 = Cost per unit replacement of the failed software component
K_4 = Cost per unit replacement of the failed hardware component
K_5 = Cost per unit replacement of the failed hardware
K_6 = Cost per unit replacement of the failed software
K_7 = Cost per unit visit by the server

9. Conclusion

In the present study, the numerical results considering a particular case $g(t) = \theta e^{-\theta t}$, $h(t) = \beta e^{-\beta t}$, $f(t) = \alpha e^{-\alpha t}$ and $m(t) = \gamma e^{-\gamma t}$ are obtained for some of the reliability measures of a computer system of two identical units with h/w and s/w components. The graphs of the mean time of the system failure (MTSF), the availability and the profit are drawn with respect to preventive maintenance rate (α) for fixed values of other parameters including a=.7 and b=.3 as shown, respectively, in Figure 2, 3 and 4. These figures reveal that MTSF, availability and profit increase with the increase of the preventive maintenance rate (α), h/w repair rate (θ) and by interchanging the values of a and b, i.e., a=.3 and b=.7 . But the values of these measures decrease with the increase of the maximum operation time (α$_0$) and maximum repair time (β$_0$). Thus, on the basis on the results obtained for a particular case, it is suggested that the reliability and profit of a system in which the chances of h/w failure are high can be improved by

- By taking one more computer system in cold standby.
- By performing preventive maintenance after a maximum operation time.
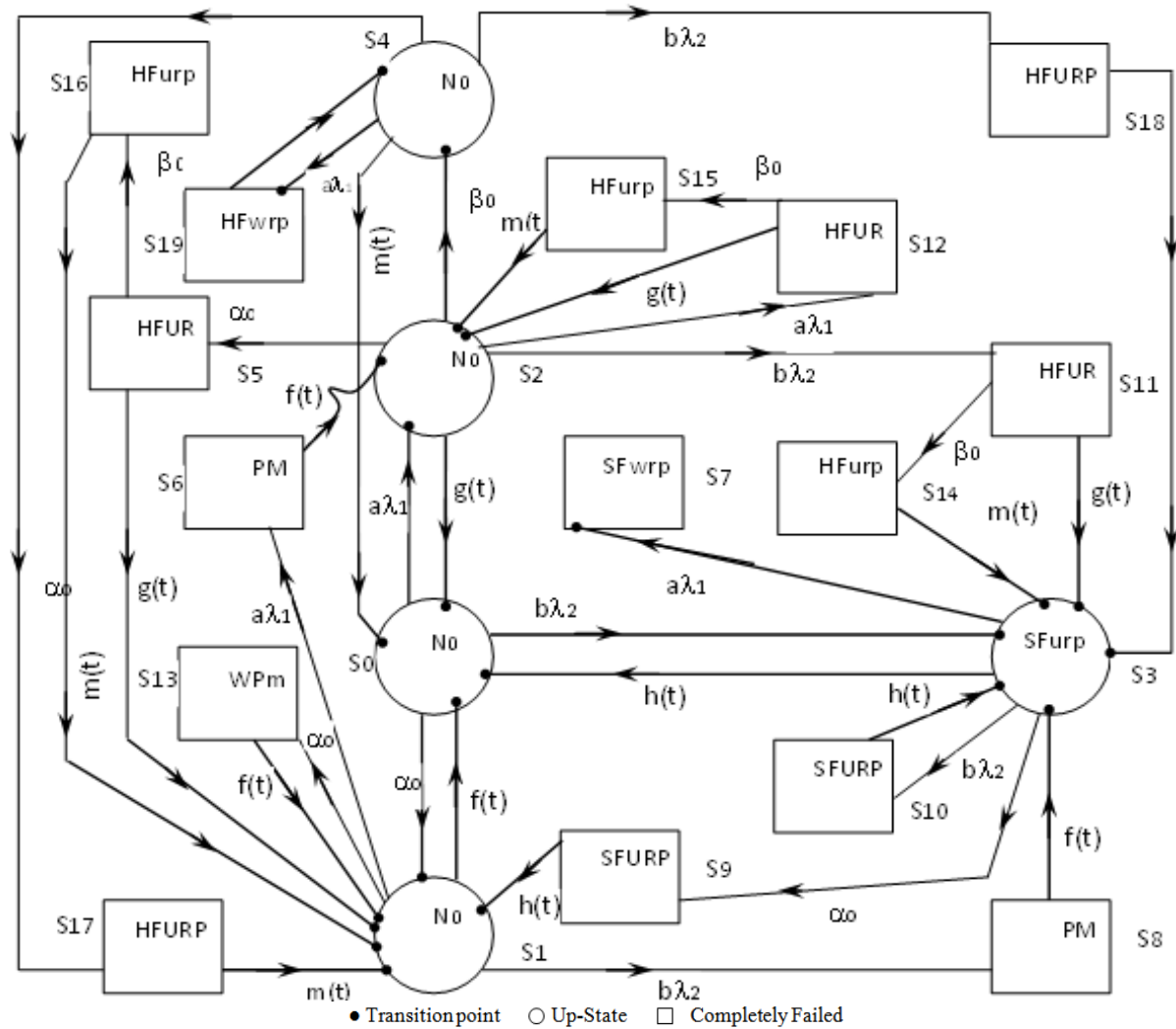- By making replacement of the outdated s/w by new one immediately.
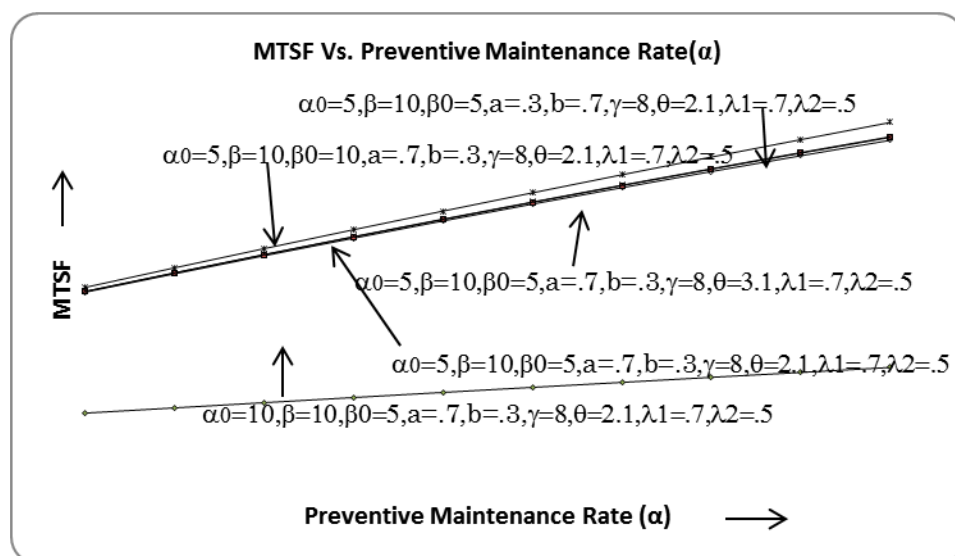
Figure 1: State transition diagram

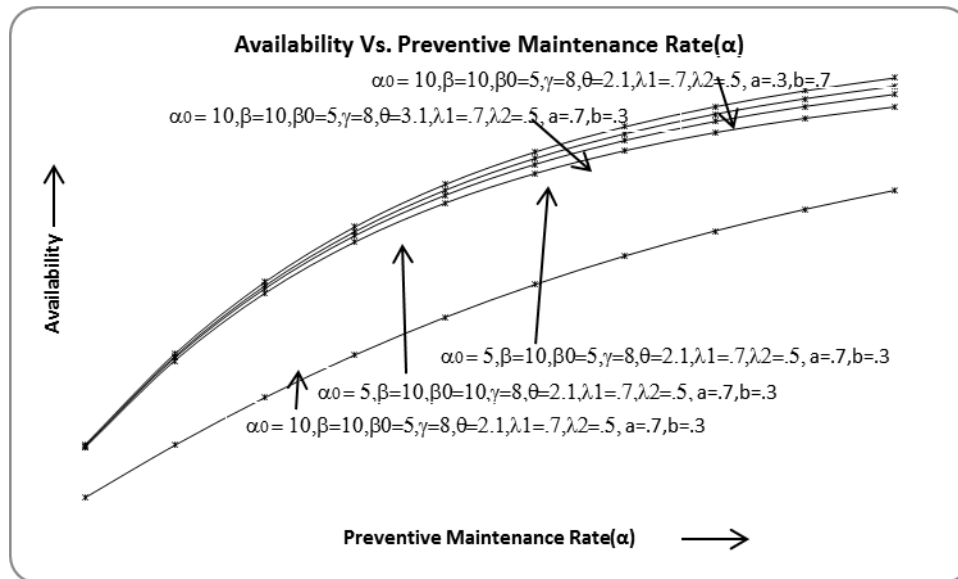**Figure 2**. MTSF Vs. Preventive Maintenace Rate

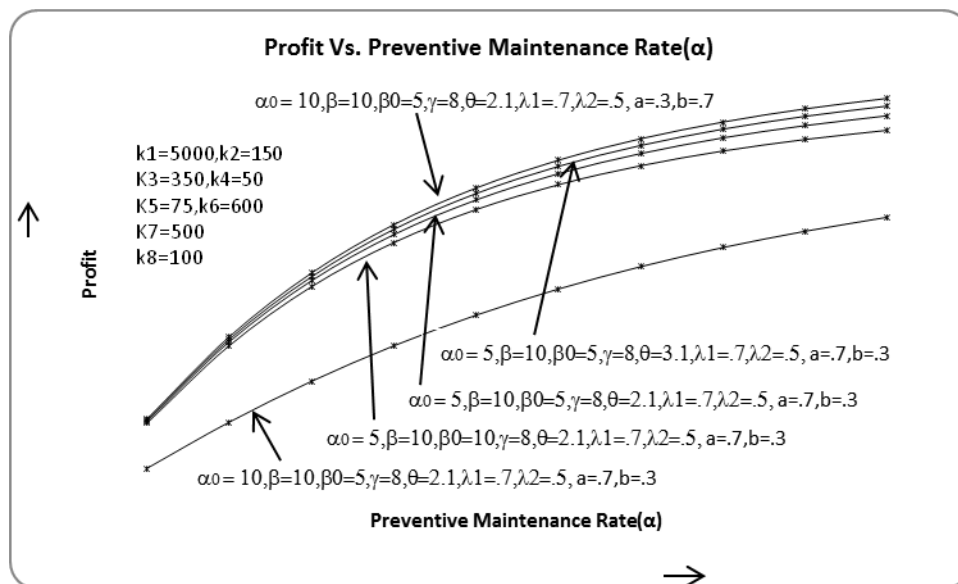**Figure 3.** Availability Vs. Preventive Maintenace Rate

Figure 4. Profit Vs. Preventive Maintenance Rate

References

[1] Malik, S. C. and Jyoti Anand: Reliability and Economic Analysis of a Computer System with Independent Hardware and Software Failures, Bulletin of Pure and Applied Sciences. E (Math. & Stat.),Vol.29 (2010) No. 1, pp.141-153.

[2] Malik, S. C. and P. Nandal: Cost- Analysis of Stochastic Models with Priority to Repair Over Preventive Maintenance Subject to Maximum Operation Time, Edited Book, Learning Manual on Modeling, Optimization and Their Applications, Excel India Publishers(2010) pp.165-178.

[3] Malik, S. C. and Kumar, Ashish: Profit Analysis of a Computer System with Priority to Software Replacement over Hardware Repair Subject to Maximum Operation and Repair Times, International Journal of Engineering Science & Technology, Vol.3 (2011) No. 10, pp. 7452- 7468.

[4] Sureria ,J.K., Malik,S.C. and Anand, Jyoti: Cost-Benefit Analysis of a Computer System with Priority to s/w Replacement over h/w Repair, Applied Mathematical Sciences,Vol.6 (2012) No. 75, pp.3723-3734.

[5] Kumar, A. , Malik, S.C. and Barak, M.S.   : Reliability Modeling of a Computer System with Independent H/W and S/W Failures Subject to Maximum Operation and Repair Times, International Journal of Mathematical Achieves, Vol.3 (2012) No. 7, pp.2622-2630.

[6] Kumar,A., Anand, J. and Malik, S.C: Stochastic Modeling of a computer system with priority to up-gradation of software over h/w repair activities, International Journal of Agricultural and Statistical Sciences, Vol. 9 (2013) No.1, pp.117-126

Integration of Statistical and Engineering Process Control for Quality Improvement

(A Case Study: Chemical Industry - National Chlorine Industries)

Karim M. Aljebory[a*], Mohammed Alshebeb [b]

[a] *Electrical Engineering Department, Faculty of Engineering, Isra University, Amman-Jordan*
[b] *MSc graduate student PME engineering, Faculty of Engineering, Isra University, Amman-Jordan*

Abstract

The quality of product in industrial process can be improved by on-line monitoring, regulating and correcting actions. There are two approaches addressing this problem: (1) Statistical Process Control (SPC), which focuses on identifying assignable causes that can be removed, leads to permanent process improvement or reduction in variability; and (2) Engineering Process Control (EPC), based on adjusting the process variables to get less deviation from target (often called feedback adjustment). Feedback adjustment regulates the process to account for sources of variability that cannot be removed by the SPC approach.

Integrating SPC/EPC is a very effective way in quality control, since features from both SPC and EPC could give a complementary performance. This work introduces a framework that integrates SPC and EPC in one methodology; SPC control limits for critical key variables are developed depending on information from the historical reference of past successful processes. While the EPC algorithm is derived of a progressive set of knowledge-based rules. The approach is applied to data collected from chlorine industry, as a case study. This is poorly automated, subject to several disturbances, monitored by measuring the feed brine solution concentration and the acidity index of samples from the ferric brine treatment tank. The experimental results proved that, when the production process is affected by certain disruptions, the process engineers have a decision making tool, by on-line monitoring and regulating the process key variables. Furthermore, by implementing proper adjustment strategies, the stability of the process can be better maintained, and significant economic benefits will be achieved.

1. Introduction

Product quality is becoming the most critical objective in various industries. So, innovative monitoring and control techniques of the process operations are strongly needed in the process control field. Generally, batch processes exhibit some batch-to-batch variation arising from such things as deviations of the process variables from their specified trajectories, errors in the charging of the recipe of materials, and disturbances arising from variations in impurities. These abnormal conditions can lead to the production of at least one batch or a whole sequence of batches with poor-quality product if the problem is not detected and remedied. Most industrial batch processes are run without any effective form of real-time, on-line monitoring to ensure that the batch is progressing in a manner that will lead to a high-quality product or to detect and indicate faults that can be corrected prior to the completion of the batch or can be corrected in subsequent batches.

Statistical Process Control (SPC) and Engineering Process Control (EPC) are two techniques that are used for improving process productivity and product quality by reducing the variability of process from target while keeping it stable and under control. SPC, a widely used technique, is an effective monitoring technique as far as the process variables can be stated by independently observed statistical variables whose values fall in the vicinity of deterministic values. On the contrary, EPC is a continuous procedure that adjusts the process manipulatable variable in order to keep the output on set point or target [14].

---

* Corresponding author. e-mail: karim.aljebory@iu.edu.jo.

Most of the literature on integrated SPC and EPC systems is focused on continuous process mainly with Algorithmic SPC. The integrated SPC/EPC systems in batch process control have not received the same degree of attention. There are numerous related studies in production process control, the first attempts to integrate EPC and SPC appeared long time ago, with the work of Barnard [7] in 1959. Using the machine-tool case study, the author demonstrated that automatic control and statistical control can be used in parallel. Box and Kramer [4] proposed the idea of using feedback control to compensate disturbances estimated by statistical forecasting, while SPC was deployed to monitor the process output after the adjustment in order to detect an assignable cause which cannot be compensated by the controller. Montgomery *et al.* [15] supported the claim that SPC can detect an assignable cause from the output rapidly, while EPC can effectively keep a process on target. Hoerl and Snee [8] proposed the term statistical engineering, defined as the study of how to best use statistical concepts, methods and tools, and integrated them with information technology and other relevant sciences to generate improved results. Box and Luceno [5] suggested using EPC activities as process adjustment and to SPC activities as process monitoring. While the two approaches have been applied independently in different areas for decades, the relationship between them has not yet been clearly explored. Nembhard and Mastrangelo [17] stated that a shift in this process can occur as the result of assignable causes (e.g., machine shutdown, or changes in raw materials, equipment or products) and during the transient state (production startup), which results in abundant loss in the process. The transient phase is induced by the dynamic behavior of the process, which causes the output to lag behind input before reaching a steady state. The dynamic behavior of processes can be modeled by deploying continuous state space equations (control theory). The integration between SPC and APC provides the opportunity to perform an adjustment, which can significantly decrease the transient-period as well as the variation of processes. Vander Wiel *et al.* [25] proposed the Algorithmic Statistical Process Control (ASPC) as a method of reducing predictable variation; ASPC employs both feedback and feed forward control, and then monitors the system to detect and remove the assignable causes of disturbances. Hunter [9] and Montgomery and Mastrangelo [17] reported that the Exponentially Weighted Moving Average (EWMA) approach is equivalent to the Proportional-Integral-Differential (PID) control technique. However, MacGregor [12] contended that the EWMA approach and PID control differ substantially. Tucker [24] also argued that control rules will compensate for assignable variation if assignable cause variation could be predictable; when assignable cause variation is unpredictable, a search for assignable causes must be made. Alwan and Roberts [1] and Montgomery and Mastrangelo [17] have all recommended that whenever observations are autocorrelated, an appropriate time series model should be fitted to these observations and control charts then applied to the residuals of the model. Montgomery *et al.* [15] examined the benefits of combining SPC and EPC techniques. Their simulations demonstrated the superiority of integrated use of SPC and EPC to the use of EPC alone. But while their simulations employed the Shewhart, CUSUM and EWMA control charts. From this short review of literature, we conclude that none of the studies was found to be dynamic on-line model to integrate SPC/EPC in chlorine process industry for quality improvements.

This paper considers three research areas: batch processes monitoring and control, integration of SPC and EPC, and case study: Chlorine production industry (Chemical Industry- National Chlorine Industries). The objectives of this study are: (a) to detail a literature review of SPC/EPC integration, (b) to establish an integrated SPC/EPC methodology for a batch process, and (c) to investigate the proposed approach with an application of the analysis and monitoring of an industrial batch Chlorine production. The remainder of the article is organized as follows. Sections 2-4 illustrate the theoretical background and derivation of the basic relations from literature for integrated SPC/EPC systems. Following this, Section 5 and 6 describe the proposed integrated SPC/EPC approach control scheme and the results of adopting it in Chlorine production. Finally, Section 7 presents the concluding remarks and future work.

2. Statistical Process Control (SPC)

The SPC is a binary view of the state of a process, i.e., whether it is running satisfactorily or not. As developed by Shewhart [21], the two states are classified as having a common cause of variations, from the management point of view, this kind is inherent in the process and difficult to eliminate or assign special cause of variations, should be identified and removed at the root.

Basics: Let x be a sample statistic that measures some quality characteristic of interest, and suppose that the mean of x is μ_x and the standard deviation of x is σ_x. Then the center line and control limits become:

$$UCL = \mu_x + L\sigma_x$$
$$CL = \mu_x \tag{1}$$
$$LCL = \mu_x - L\sigma_x$$

where L is the "distance" of the control limits from the center line, expressed in standard deviation unit, (a common choice is $L=3$). Dr. Walter A. Shewhart first proposed this general theory of control charts.

2.1. Control Charts for Individual Measurements

The control chart for individuals uses the moving range of successive observations to estimate the process variability. The moving range at time t is defined as $MR_t = | X_t - X_{t-1} |$. Letting $\overline{MR}$ be the average of the moving ranges, an estimate of σ is

$$\hat{\sigma} = \frac{\overline{MR}}{d_2} = \frac{\overline{MR}}{1.128} \tag{2}$$

d_2 is constant that depends on the size of the sample, values of d_2 for sample sizes ($2 \leq n \leq 25$) are given in (Montgomery,2013), noting that($d_2 = 1.128$) when two consecutive observations are used to calculate a moving range ($n = 2$). Then the control chart for individual measurements is:

$$UCL = \mu_x + 3\frac{\overline{MR}}{d_2}$$

$$CL = \mu_x \qquad (3)$$

$$LCL = \mu_x - 3\frac{\overline{MR}}{d_2}$$

2.2. The Cumulative Sum Control Chart (CUSUM)

CUSUM chart was developed by Page (1954). This technique plots the cumulative sums of deviations of the sample values of a quality characteristic from a target value against time. The tabular CUSUM works by accumulating derivations from μ_o that are above target with one statistic C^+ and accumulating derivations from μ_o that are below target with another statistic C^- The statistics C^+ and C^- are called one-sided upper and lower CUSUM, respectively. They are computed as follows:

$$C_t^+ = \max\left[0, x_t - (\mu_o + K) + C_{t-1}^+\right] \qquad (4)$$

$$C_t^- = \max\left[0, (\mu_o - K) - x_t + C_{t-1}^-\right] \qquad (5)$$

And the starting values are $C_o^+ = C_0^- = 0$.

In equations (4) and (5), K is called the reference value and it is often chosen about halfway between the target μ_o and the out of control value of the mean μ_1 that we are interested in detecting quickly, using (K=0.5) usually provide a good results. Note that C_t^+ and C_t^- accumulate deviations from the target value μ_o that are greater than K, with both quantities reset to zero on becoming negative. If either C_t^+ or C_t^- exceeds the decision interval H, the process is considered to be out of control, a reasonable value for H is five times the process standard deviation σ and (Montgomery, 2013) [16].

2.3. The Exponentially Weighted Moving Average Control Chart (EWMA)

The EWMA control chart was introduced by Roberts [20, 3]. The performance of the EWMA control chart is approximately equivalent to that of the CUSUM control chart, and in some ways it is easier to set up and operate. As with the CUSUM, the EWMA is typically used with individual observations, EWMA technique has been widely used in order to monitor the process mean, since it weighs the average of all past and present observations. In the EWMA, the predicted value of process mean at z_t time t, is defined as

$$z_t = \lambda x_t + (1-\lambda) z_{t-1} \qquad (6)$$

where ($0 < \lambda \leq 1$) is a constant factor, and x_t is the observed value of process mean at time t, the starting value required with the first sample at ($t = 1$) is the process target, so that ($z_o = \mu_o$).

The EWMA control chart would be constructed by plotting z_t versus the sample number or time (t). The center line and control limits for the EWMA control chart are as follows:

$$UCL = \mu_o + L\sigma\sqrt{\frac{\lambda}{(2-\lambda)}\left[1-(1-\lambda)^{2t}\right]} \qquad (7)$$

$$CL = \mu_o$$

$$LCL = \mu_o - L\sigma\sqrt{\frac{\lambda}{(2-\lambda)}\left[1-(1-\lambda)^{2t}\right]} \qquad (8)$$

In equations (7) and (8) above, the factor L is the width of the control limits.

3. Engineering Process Control (EPC)

Engineering Process Control (EPC) is a popular strategy for process optimization and improvement. It describes the manufacturing process as an input–output system where the input variables (recipes) can be manipulated (or adjusted) to counteract the uncontrollable disturbances to maintain the process target. The output of the process can be measurements of the final product or critical in-process variables that need to be controlled.

3.1. Process Control by Feedback Adjustment: Integral Control

Let the process output characteristic of interest at time period t is y_t, and we wish to keep y_t as close as possible to a target T. This process has a manipulatable variable x, and a change in x will produce all of its effect on y within one period, that is,

$$y_t - T = gx_t \qquad (9)$$

where g is a constant called the process gain that relates the magnitude of a change in x_t to a change in y_t. Now, if no adjustment is made, the process drifts away from the target according to a disturbance N_{t+1}

$$y_{t+1} - T = N_{t+1} \qquad (10)$$

Suppose that the disturbance can be predicted adequately using EWMA which is shown in Section 2.3.

$$\hat{N}_{t+1} = \hat{N}_t + \lambda\left(N_t - \hat{N}_t\right) = \hat{N}_t + \lambda e_t \qquad (11)$$

where $e_t = (N_t - \hat{N}_t)$ is the prediction error at time period t and ($0 < \lambda \leq 1$) is the weighting factor for the EWMA. Therefore, the adjustment to be made to the manipulatable variable at time period t

$$x_t - x_{t-1} = -\frac{\lambda}{g}(y_t - T) = -\frac{\lambda}{g}e_t \qquad (12)$$

The actual **set point** for the manipulatable variable at the end of period t is simply the sum of all the adjustments through time t, or

$$x_t = \sum_{j=1}^{t}(x_j - x_{j-1}) = -\frac{\lambda}{g}\sum_{j=1}^{t}e_j \qquad (13)$$

This type of process adjustment scheme is called **integral control (I).** It is a pure feedback control scheme that sets the level of the manipulatable variable equal to a weighted sum of all current and previous process deviations from target.

3.2. The Adjustment Chart

The feedback adjustment scheme based on integral control (Section 3.1) can be implemented so that the adjustments are made automatically. This involves some combination of sensors or measuring devices, a logic device or computer, and actuators to make the adjustments of the variable x. When EPC adjustment is implemented in this manner, it is often called Automatic Process Control (APC).

In many processes, feedback adjustments can be made manually by observing the current output deviation from target, compute the amount of adjustment to apply using equation (12), and then bring x_t to its new set point. When adjustments are made manually, a variation called the manual adjustment chart is very useful.

3.3. Bounded Adjustment Chart

The adjustment procedures in Sections (3.1) and (3.2) are very straightforward to implement, but they require an adjustment to be made to the process after each observation. In feedback adjustment applications, in chemical and process industries, this is not a serious issue because the major cost is the cost of being off target, and the adjustments themselves are made with either no or very little cost. Indeed, they are often made automatically.

There are several ways to do this. One of these ways is the bounded adjustment chart, a variation of the procedure (Section 3.2) in which an adjustment will be made only in periods for which the EWMA forecast is outside one of the bounds given by ($\pm L$). The boundary value L is usually determined from engineering judgment, taking the costs of being off target and the cost of making the adjustment into account. Montgomery [16] proposed the following relation to estimate $\hat{\sigma}_{EWMA}$.

$$\hat{\sigma}_{EWMA} = \sqrt{\frac{\lambda}{2-\lambda}} \hat{\sigma}_{unadjusted\_process} \qquad (14)$$

Note that, if the standard deviation of the unadjusted process is known, so the standard deviation of EWMA is approximately. Noting that we often use control limits on a EWMA that are slightly less than three-sigma.

4. Integration of SPC/EPC Methods

SPC and EPC are two complementary strategies developed for quality improvement. There is a corresponding relationship between them through prediction. EWMA predictor, which corresponds to the integral (I) control, is one of the most frequently used prediction methods in business and industry, mainly because of its simplicity and efficiency. Wei Jiang and John V. Farr [27] proposed four categories of ongoing research and application of the two quality-control approaches as shown in Figure 1:

- If a process is not correlated, there is no need to employ EPC schemes. Traditional SPC control charts should be used for identifying assignable cause variations.
- When data are correlated, the possibility of employing EPC scheme should be examined. SPC control charts are invoked to monitor auto correlated processes if no feasible EPC controller exists.
- If appropriate controller is available, EPC control scheme can be employed to compensate the auto correlated disturbance. However, no single EPC controller can compensate all kinds of variations.
- To identify and understand the cause of process changes, a unified control framework should be applied to regulate a process using feedback control, while using the diagnostic capability of SPC to detect sudden shift disturbances to the process.

The integration of SPC/EPC looks for the best opportunities of quality improvement by integrating/ combining the strengths of SPC and EPC in various levels of control that may be incorporated into a manufacturing system. According to literature review there are four types of integration, conventional SPC, algorithmic SPC, Active SPC, and Run-to-Run.

5. The Proposed SPC/EPC Integration Approach

Based on the theoretical development of SPC/EPC integration approaches, we construct an integrated approach guideline so as to fill up the gap and implement SPC/EPC integration into practice. The theoretical and practical concerns that we have discovered will be incorporated in this guideline. As shown in Figure 2 the proposed SPC/EPC integration approach is conducted in three phases; off-line monitoring, on-line measuring and detecting, and integrating SPC/EPC phase.

6. Case Study

A real case from a chlorine industry has been studied. In this section, we will discuss the application of the proposed approach to data collected from this process. This industrial process is poorly automated, subject to several disturbances. We used the method of feedback integral adjustment to show how this technique can be easily implemented in process where there is a manipulatable variable that affects the process output.
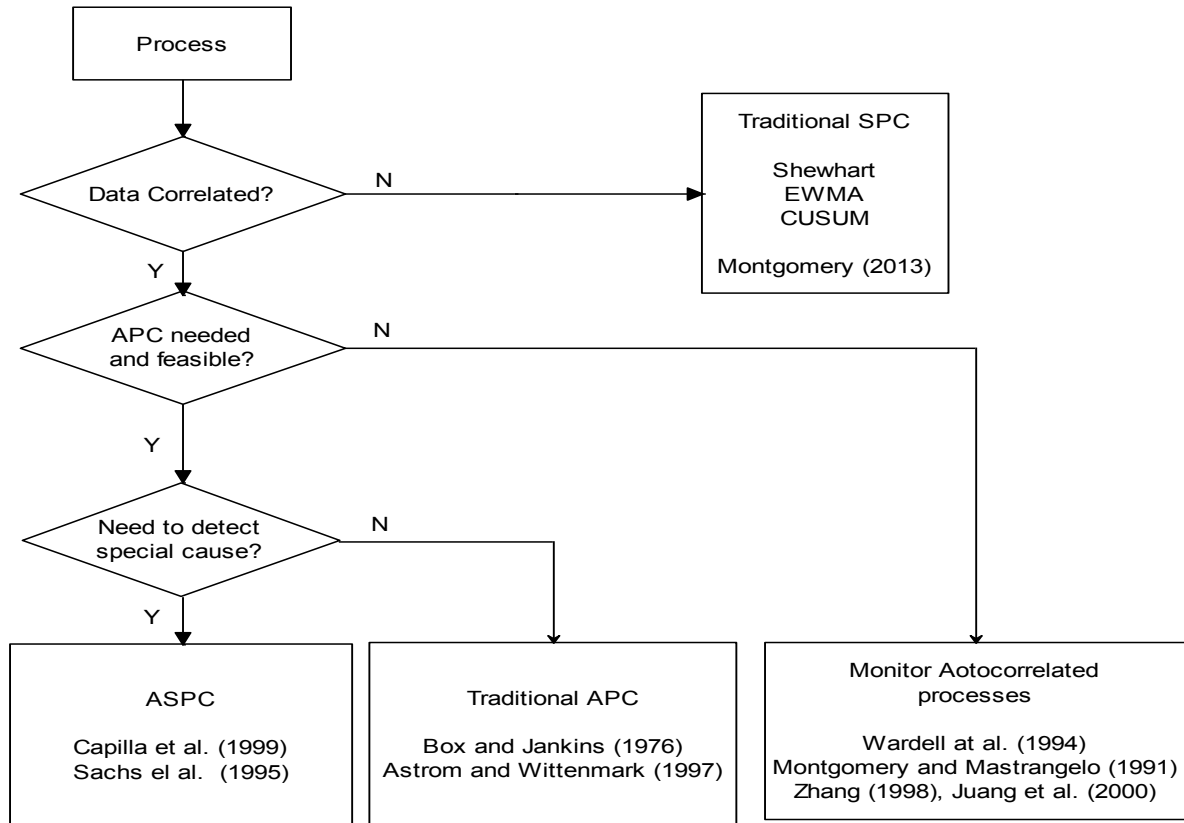
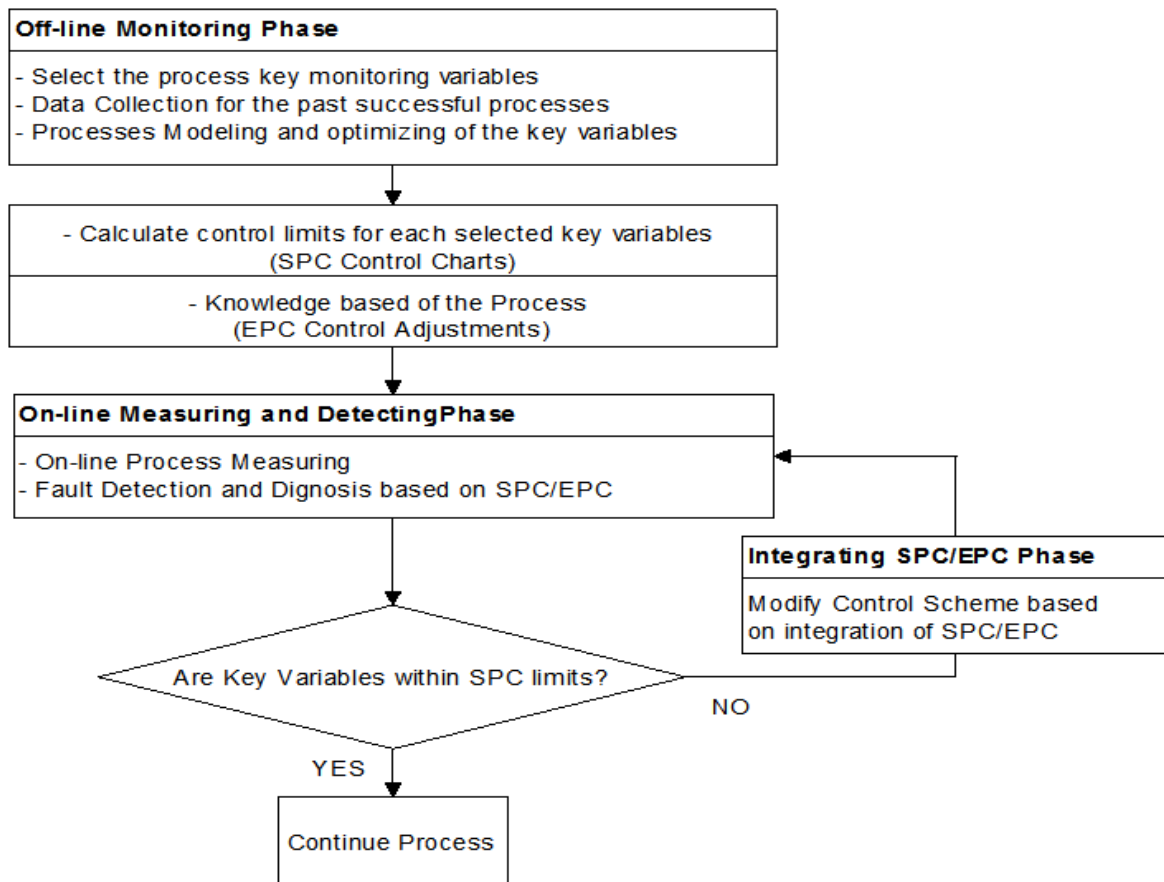**Figure 1**. Control scheme select of SPC and EPC methods

Figure 2. The Guiding flowchart for the proposed SPC/EPC integration approach

Case Briefing

The case for practical study is a process from a chlorine factory, as depicted in Figure 3. Chlorine is produced by passing an electric current through a solution of brine (salt dissolved in water). This process is called electrolysis. There are three main technologies of producing chlorine: (1) the membrane cell process, nowadays most widely used in Europe, (2) the mercury cell process, being phased out worldwide because of the toxic character of mercury, and (3) the diaphragm cell process. Our study was conducted in a factory using membrane process to produce chlorine products, so that we will focus only on this process.

The two electric connection points of each chlorine production cell, the anode and the cathode, are separated by an ion-exchange membrane. Only sodium ions and a little water pass through the membrane. The brine is de-chlorinated and re-circulated. Solid salt is usually needed to re-saturate the brine. After purification by precipitation-filtration, the brine is further purified with an ion-exchanger. The caustic solution leaves the cell with about 30% concentration and, at a later stage in the process, is usually concentrated to 50%.

6.1. Off-line Monitoring Phase

The first step in the real case study is process analysis, which is called off-line monitoring. The purpose of the process analysis is: (1) to understand the entire process, including the critical relations between the quality requirements and the performance metrics of both input and output conditions, and (2) the selection of key variables that could reduce inefficiencies in the process.

Select the Process Critical Monitoring Variables

For demonstration, we selected only one production line from the process. In this production line, sodium hypochlorite (NaOCl) is the output that required to achieve a certain target specification value of about (11-12) %. Based on consultations, we define critical-to-quality input key variables, in the selected production line. The key variables, at different process time, were used to determine the advance and the final product quality. These variables are feed brine solution concentration (NaCl) and acidity index (pH) in ferric brine treatment tank as shown in Figure 3. Variable monitoring is done each one hour sampling times. Figure 4 shows the fluctuation of selected key variables with time.
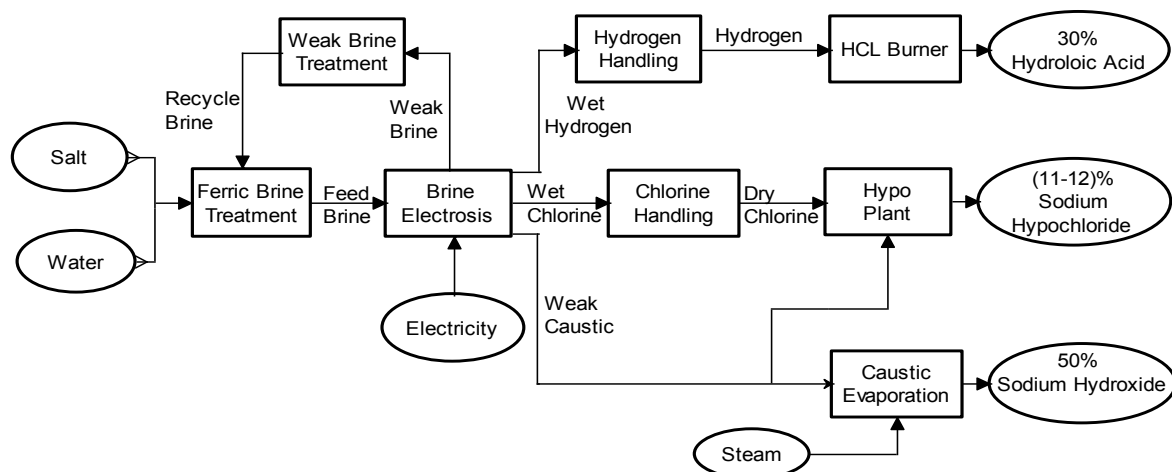

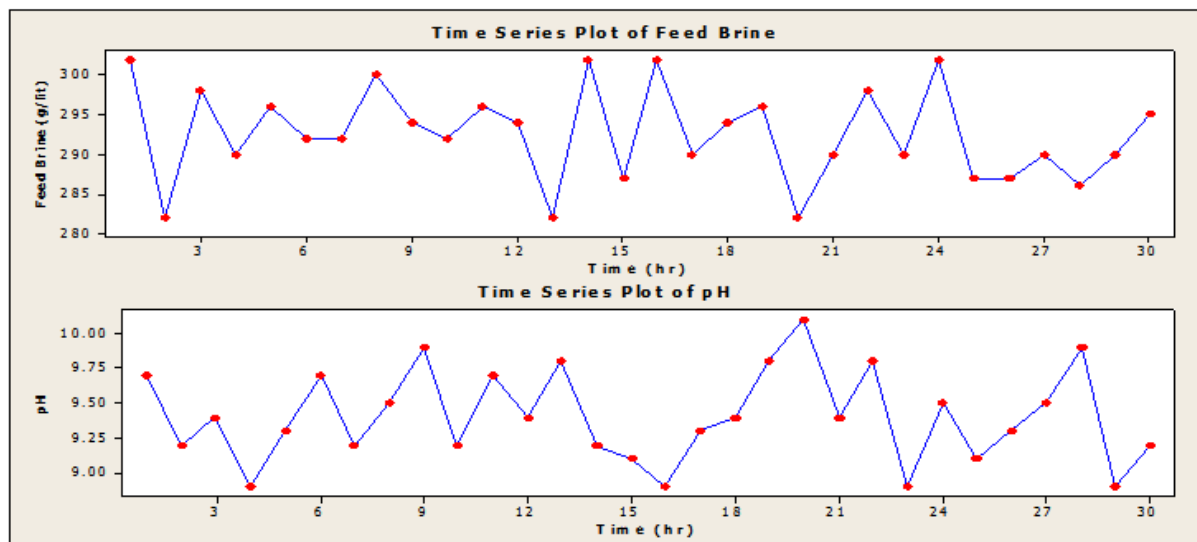**Figure 3**. Factory Process Activity Flowchart

Figure 4. Feed Brine concentration and Acidity Index fluctuations with time

Quality measurements are only available off-line; the operating procedure for a process progress through a nominal recipe, which is subject to several online adjustments made by the factory personnel depending on the actual progression of the process, as it is monitored by the quality measurements.

Data Collection of the Past Successful Processes

Based on the analysis of historical database using Minitab program and interviews with technical experts of the factory, four inputs key variables were selected as critical to monitor the process and one final output. The variables selection is based on historical production reports. These variables are: the value of *NaCl* measured at times 800, 1600 and 2200 hours during production day denoted by *NaCl 800*, *NaCl 1600* and *NaCl 2200*, respectively, and the value of *pH* measured at time 00 which denoted by *pH 00*. Each one of these critical variables is selected from past thirty successful processes. These key variables and final product output of *NaOCl* Sodium were presented in Table 1.

Processes Modelling and optimizing

In this phase, the selected key variables are modelled in order to apply SPC tools, the standard assumptions that are usually cited in justifying the use of control charts are that the data generated by the process when in control are normal (i.e., the data have a normal probability density function) and independent of observations (i.e., value is not influenced by its past value and will not affect future values) distributed with mean μ and standard deviation σ.

The test of normality and the test of independence of each selected key variable are applied as shown in Figure 5; this figure approved standard assumptions, that the data generated by the process are in control, are normally distributed and independent. In order to predict *NaOCl* for a new process, we used Minitab to model the output of *NaOCl* as a linear regression with the four selected input key variables. The use of Minitab confirmed the following equation with a regression square (R-Sq) coefficient equal to 84%.

$$NaOCl = 28.2 - 0.0192\,NaCl800 - 0.0281\,NaCl1600 \\ + 0.00034\,NaCl2200 - 0.325\,pH00 \tag{15}$$

Table 1. Measurements of key critical variables for thirty successful processes

| Exp.	NaCl 800 (g/lit)	NaCl 1600 (g/lit)	NaCl 2200 (g/lit)	pH 00	NaOCl
1	275	295	293	9.3	11.66
2	304	287	285	8.7	11.63
3	300	294	306	9.4	11.15
4	292	294	298	9.2	11.19
5	300	287	296	9.2	11.41
6	295	297	300	9.8	11.0
7	287	291	300	9.3	11.56
8	293	296	306	9.4	11.27
9	295	296	293	9.2	11.15
10	291	291	300	9.5	11.41
11	295	287	298	9.4	11.51
12	313	291	302	9.4	11.0
13	300	292	295	8.9	11.41
14	294	294	289	9.2	11.29
15	315	289	297	9.6	11.0
16	287	288	278	9.9	11.41
17	283	288	290	9.3	11.78
18	279	295	290	9.2	11.72
19	306	297	302	9	11.09
20	312	297	304	9.7	11.29
21	284	290	290	8.8	11.92
22	298	297	295	9.4	11.09
23	286	297	298	9.3	11.48
24	276	298	302	8.7	11.75
25	297	303	301	9.4	11.05
26	289	292	305	9.3	11.48
27	285	291	296	8.7	11.85
28	314	290	290	9.4	11.05
29	295	299	300	9.2	11.09
30	279	286	293	9	12
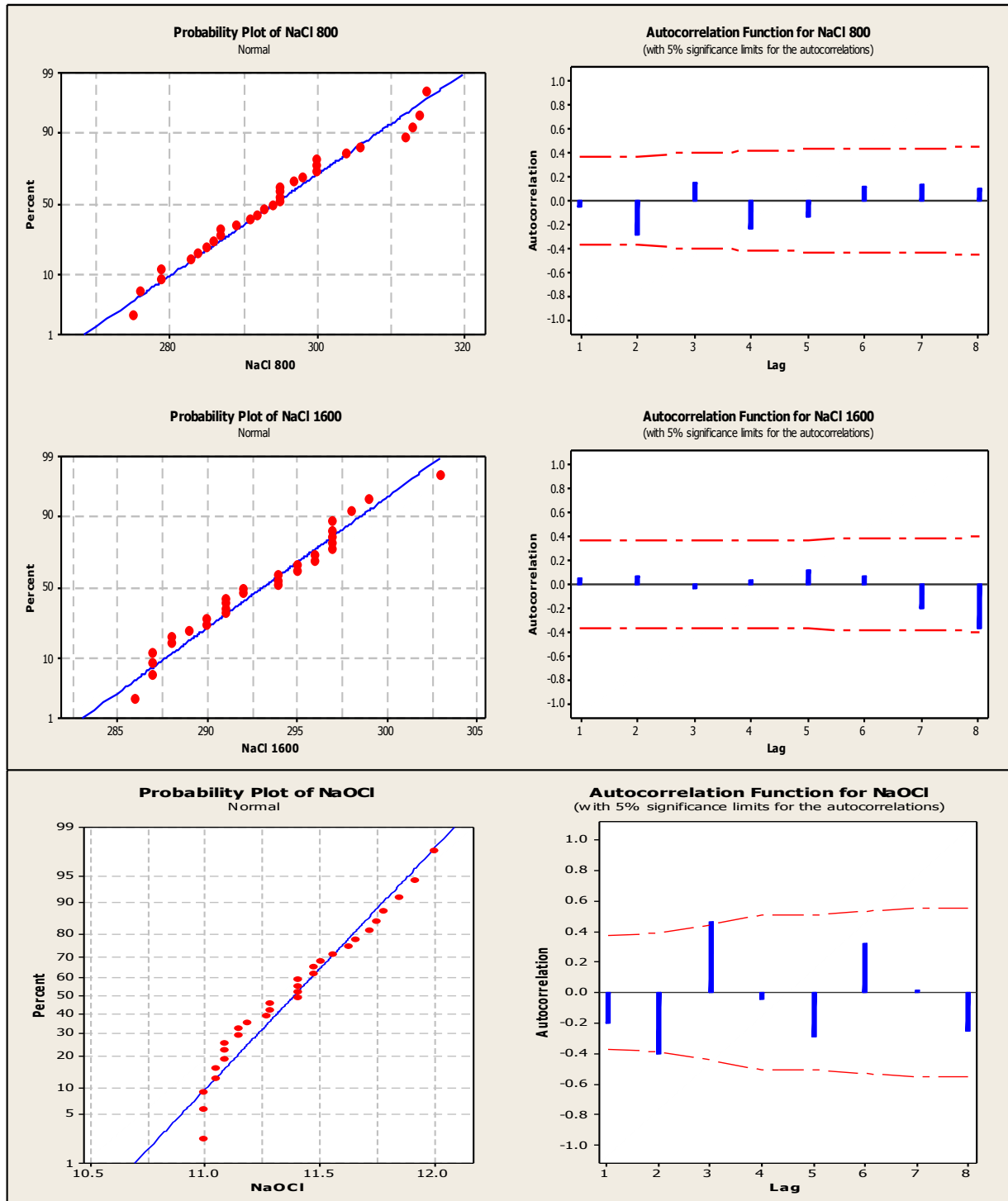
Figure 5. Normal Probability and Autocorrelation (independent) tests for key variables
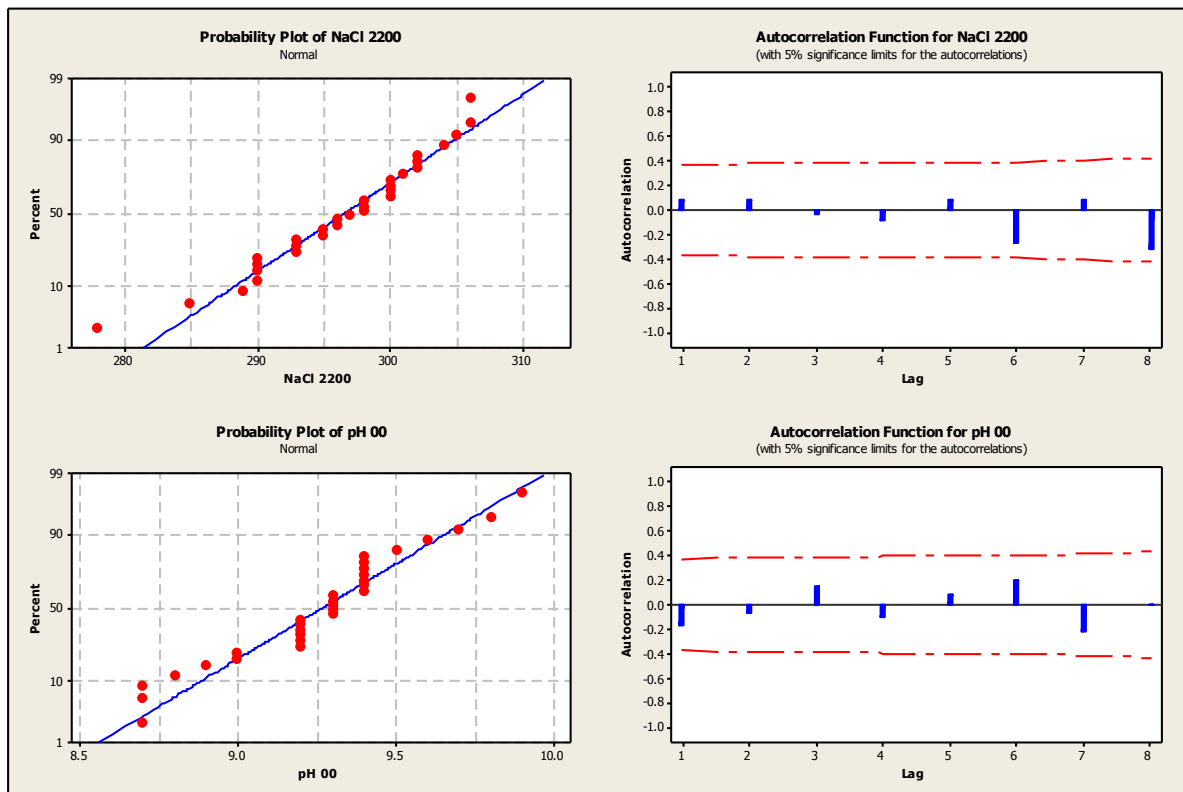
Figure 5. (continue) Normal Probability and Autocorrelation (independent) tests for key var

6.2. On-line Measuring and Detecting Phase

The key to a successful operation is efficient on-line process monitoring, which enables the early warning of process disturbances, process malfunctions or faults. Where early detection of such problems is followed by the location of their source, the efficiency and consistency of production can be significantly improved. Schemes for process monitoring, fault detection and diagnosis can then be used as intelligent supervisory process systems, which can support process operators and engineers in dealing with process deviations and identifying the root cause of these deviations. These schemes are based upon process models built from factory data.

On-line Process Measuring

After verifying the test of normality and the test of independence, the control charts of each selected variable are applied as shown in Figure 6. To monitor the new process, it is necessary to measure the four selected key variables and place the point in the corresponding control chart in Figure 6. These values are also used to predict the *NaOCl* as indicated in equation (15).

Fault Detection and Diagnosis Based on SPC and EPC

For reasons of simplicity, only a few regulations of EPC were presented in the flow chart of Figure 7. For each control chart of Figure 6, two cases arise, exceeding the upper or lower Control Limits. The production control procedure of a new process should be done in accordance with the flow chart shown in Figure 7; the process should proceed normally if there is no assignable cause alert; otherwise corrective control action should be taken to remove the assignable cause. Moreover, the production manager can predict the final quality output of *NaOCl* by using equation (15).

6.3. Integrated SPC/EPC Phase

This phase will provide the factory process engineer a good toll to regulate or adjust the added salt as instructed by flow chart of Figure 7 in order to maintain feed brine with SPC limits.

Noting that factory process engineers explained for us the fact that maintaining the feed brine concentration in the main tank as close as possible to the target specification values of (295 *g/lit*) will improve the final products quality and extend membrane cells life, so that we will focus in this phase to comply with this fact by applying an integral control approach.

In order to apply the integral control approach, we will need a process model, with the note that, for purposes of simplicity, we will apply this approach in ferric brine treatment tank only. The process model is based on flow chart of Figure 3, including the input variables: the recycle brine, water, actual brine concentration in tank, and the amount of the salt added to main tank. The output variable is the feed brine concentration.
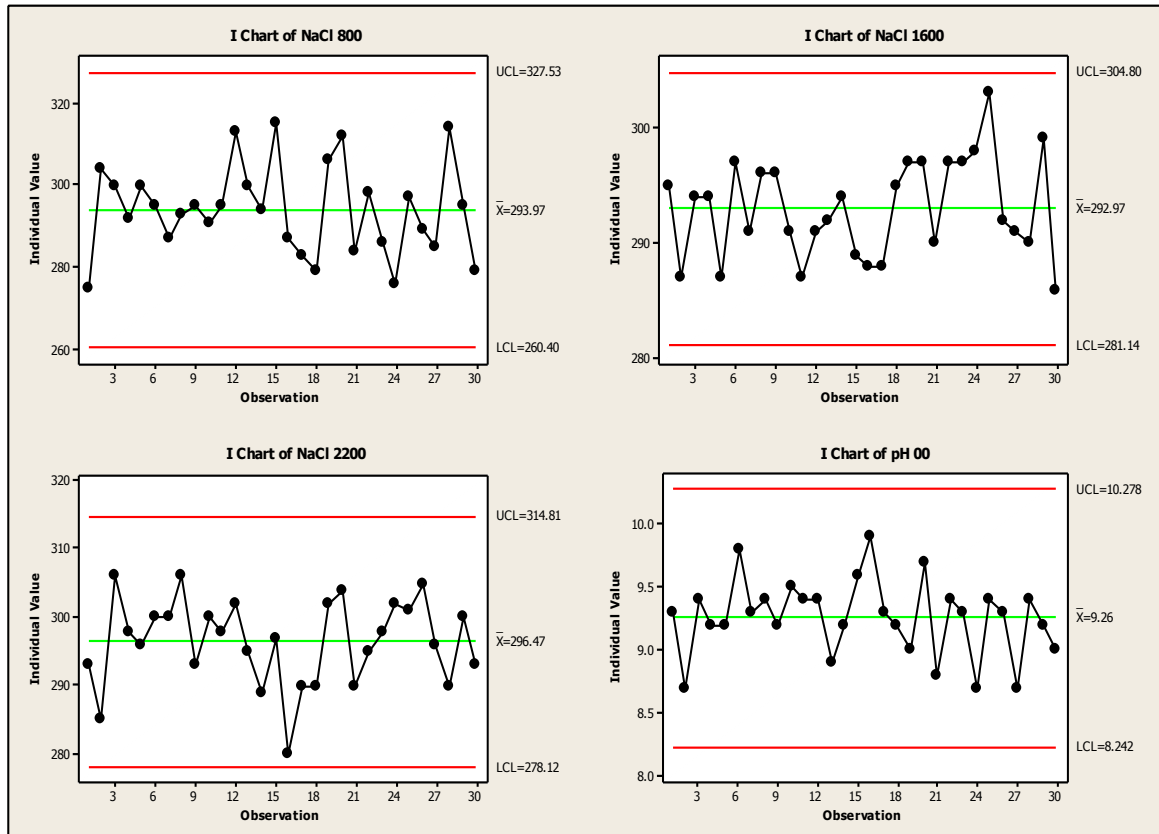
Figure 6. Individual Control Charts for Key Variables
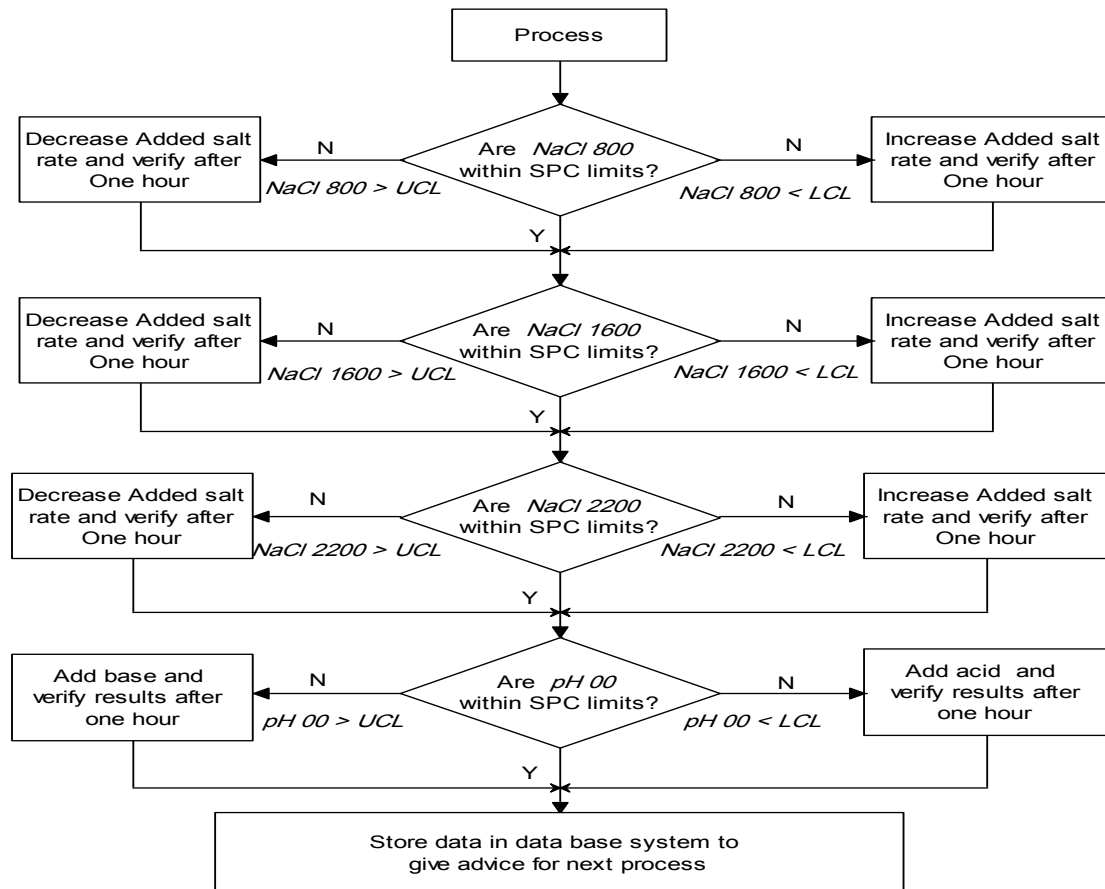

Figure 7. Flow chart for EPC regulations according to SPC charts

We tried to find theoretical equation to compute the value of brine solution concentration in main tank which denoted by $NaCl_{comp}$ (i.e., considering the recycle brine denoted by $NaCl_{recy}$ added now denoted by $NaCl_{added}$ and the actual brine concentration value now in main tank denoted by $NaCl_{sol}$). Equation 16 below is an approximation to calculate $NaCl_{comp}$ after one hour, all measures in litres ($1\ m^3 = 1000$ litres) and grams.

$$NaCl_{comp} = \frac{\left(m1 * NaCl_{recy} + NaCl_{added} + m3 * NaCl_{sol}\right)}{\left(m1 + m2 + m3\right)} \quad (16)$$

Where $m1$ is the volume of recycle brine flowing in during one hr, $m2$ is the volume of water flowing in during one hr and $m3$ is the main tank capacity.

Equation (16) was derived, because we need to establish a relationship between feed brine in main tank y_t (output) vs. computed brine x (input) , this relationship is required to apply feedback adjustment control which explained in section (3). The scatter plot & linear regression for y_t vs. x is shown in figure 8.

Statisticians explained that R-Sq must be at least 0.70 for the regression line to be considered as meaningful. By using Minitab, the R-Sq value of the regression line was 84.3% as shown below in equation (17).

$$y_t = 40.2 + 0.864x \quad (17)$$

where y_t represents feed brine solution concentration and x is computed brine solution from equation 16, hence, the process Gain (g) = 0.864. It is desired to maintain feed brine solution y_t close as possible to the target specifications value ($T = 295$ *g/lit*), this can be done by controlling added salt (Kg) through predication of computed salt that required to maintain feed brine within limits. Table 2 column 2 shows 30 observations on the number of unadjusted process data taken every one hour, note that, despite best efforts to bring the process into a state of statistical control, the data tends to wander away from the target.

Individuals and moving range control charts are shown in figure 9, indicating the lack of statistical stability in the process. The actual sample average and standard deviation of feed brine concentration for these 30 observations is (288.8 *g/lit*) and (13.94) respectively, note that these values obtained by using Minitab.

An EWMA or CUSUM control chart on the output deviation from target would generally detect the assignable cause more quickly than individual moving range chart. We will forecast the disturbances with an EWMA having ($\lambda = 0.4$) as suggested by Hunter (1989), who showed that using this value produce nearly identical weights for current and previous observations as do the Western Electric rules. Figure 10 is a EWMA, and it signals the assignable cause at observation ($t = 3$).

We will use the bounded adjustment chart procedure illustrated in Section 3.3 in which an adjustment will be made only in periods for which the EWMA forecast is outside one of the bounds given by $\pm L$. The boundary value L is usually determined from engineering judgment, taking the costs of being off target and the cost of making the adjustment into account. But we will use equation (14) to set upper and lower boundary limits, the upper limit ($+L = 302$ *g/lit*) and lower limit ($–L=288$ *g/lit*). This means that we will only make an adjustment to the process when the EWMA exceeds these two limits.
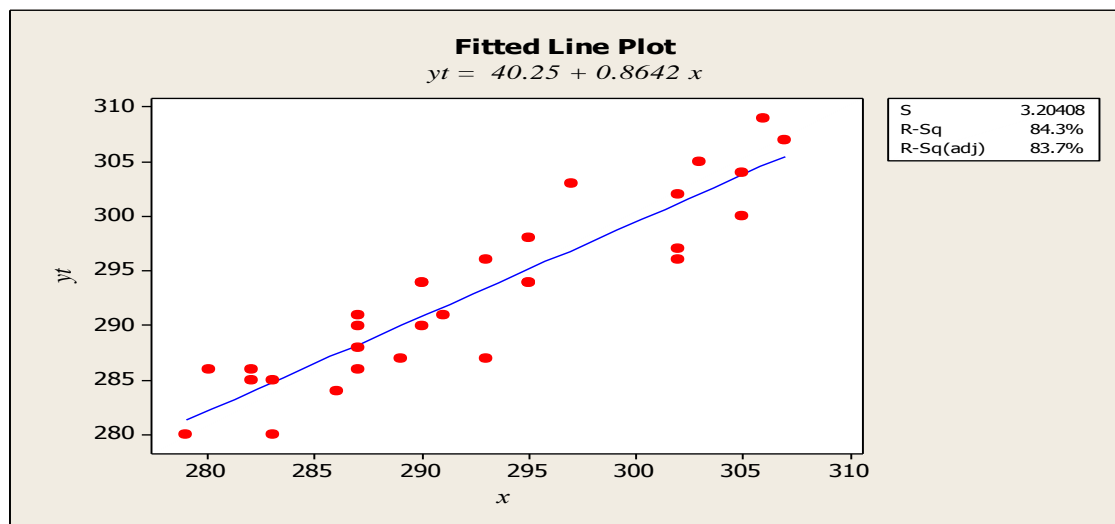

Figure 8. Fitted plot of Feed Brine with Computed Brine

Table 2. Process Data for the Boundary Adjustment Chart

Time (hr)	Original Process Output	Adjusted Process Output	EWMA	Adjustment	Cumulative Adjustment or Set point
1	296	296	296	0	0
2	305	305	300	0	0
3	316	316	306	-9.7	-9.7
4	307	297.3	296	0	-9.7
5	301	291.3	294	0	-9.7
6	305	295.3	295	0	-9.7
7	291	281.3	289	0	-9.7
8	295	285.3	288	4.5	-5.2
9	312	306.8	300	0	-5.2
10	280	274.8	290	0	-5.2
11	310	304.8	296	0	-5.2
12	294	288.8	293	0	-5.2
13	299	293.8	293	0	-5.2
14	282	276.8	287	8.4	3.2
15	301	304.2	299	0	3.2
16	286	289.2	295	0	3.2
17	292	295.2	295	0	3.2
18	272	275.2	287	9.2	12.4
19	281	293.4	294	0	12.4
20	287	299.4	296	0	12.4
21	279	291.4	294	0	12.4
22	285	297.4	296	0	12.4
23	277	289.4	293	0	12.4
24	273	285.4	290	0	12.4
25	268	280.4	286	6.8	19.1
26	276	295.1	295	0	19.1
27	270	289.1	293	0	19.1
28	272	291.1	292	0	19.1
29	275	294.1	293	0	19.1
30	278	297.1	295	0	19.1

To evaluate the effect of the suggested controller and the integrated control method, the study chooses to compare some statistical parameters such as adjusted and unadjusted process average, variance, standard deviation, number of adjustments during process and the mean of the squared error or the performance measure (PM), the formula for PM is:

$$PM = \frac{1}{n}\sum_{t=1}^{n}\left(y_t - T\right)^2 \qquad (18)$$

where n is the number of observations in this study ; y_t is the output of quality characteristics or feed brine solution; T is the target value, the smaller value of PM is the better.

Based on theoretical background given in this study and data collected from this process, we created a simple program to do required calculations; program outputs are

shown in columns (3-6) of table 2. We will use computed brine as manipulatable variable in this process, and the relationship between the output and this variable as indicated in equation16. The computations for the EWMA are given in table 2 column 4, the EWMA is started off at target, and the first observation in which it exceeds upper limit is at observation ($t=3$). The output deviation from target in observation 3 is (316 *g/lit*), so the adjustment would be calculated as usual in integral control. That is, we would change the manipulatable variable from its previous setting in observation 3 by ($-9.7g/lit$). The full effect of this adjustment then would be felt in the next observation, 4. The EWMA would be reset to target value at the end of observation 3 and the forecasting procedure started afresh. The next adjustment occurs in observation 8, where (+4.5 *g/lit*) of adjustment are made. The last column records the cumulative effect of all adjustments. Note that only five adjustments are made over the 30 observations.

The results of the original unadjusted output variable, the adjusted output, and EWMA forecasts are shown in Figure 11. The variability in the adjusted output around the target has been reduced considerably. The new average is closer to target, variance is smaller, standard deviation is improved by nearly 30% and performance measure is relatively better.

In order to further investigate the integrated SPC/EPC control system based on feedback boundary adjustment model, we conduct more calculations based on different values of λ as shown in table 3, as a conclusion from this table that the best performance for this process occurred when (λ=0.5) because its provide better process average, variance, standard deviation, number of adjustments and PM.

5. Conclusions

Various schemes of integration between SPC and EPC had been proposed in literature, with a view to complement each other's shortcomings. The two classes of methods can be linked and integrated in a unified quality control framework. While intensive work has been focused on developing various efficient and robust EPC controllers, we emphasize the crucial task of monitoring auto correlated processes and EPC systems. In this paper, a scheme of integration was evaluated. The results proved that joint monitoring of EPC regulated processes' outputs, using SPC leads to the earliest detection of assignable causes.

The case study demonstrates the effectiveness of the EPC/SPC integration, since process engineers are now able to use a decision-making tool when the production process is affected by certain disruptions, with obvious consequences on product quality, productivity and competitiveness.

The approach that we proposed does not require continuous adjustments on the process. Therefore, it is suitable for process control when the process is subject to infrequent random shocks. The number of adjustments can be justified by comparing the cost and the benefit of the adjustment. This method requires much less computation effort and is easy to be implemented on the manufacturing floor.
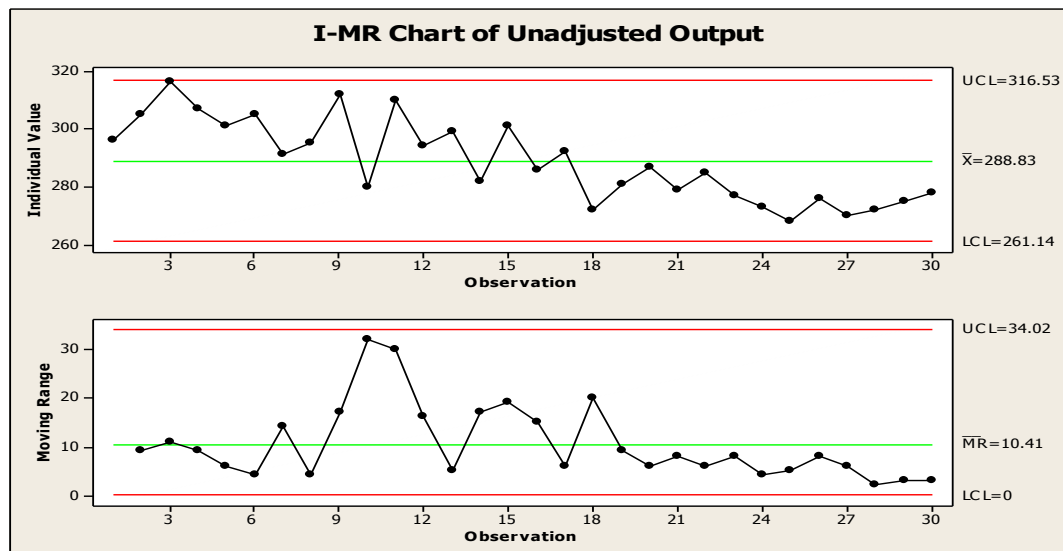
Figure 9. Individual and moving range chart applied to the feed brine
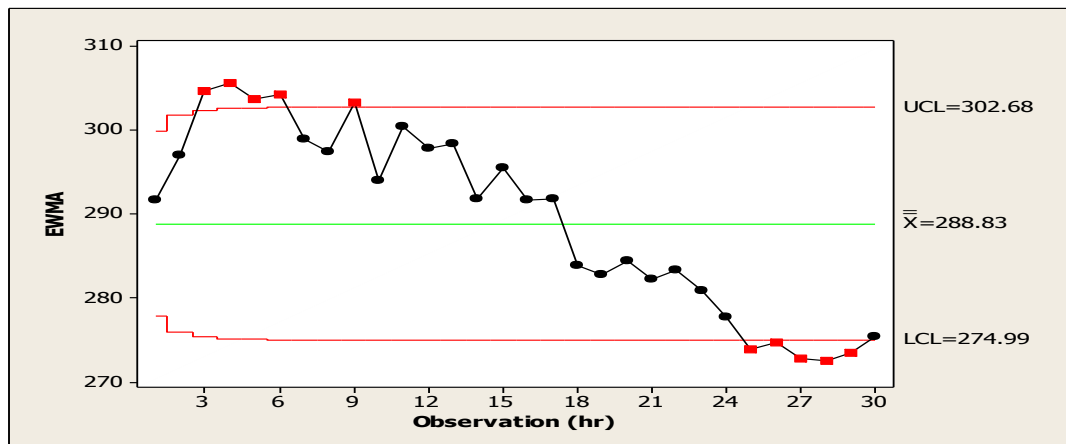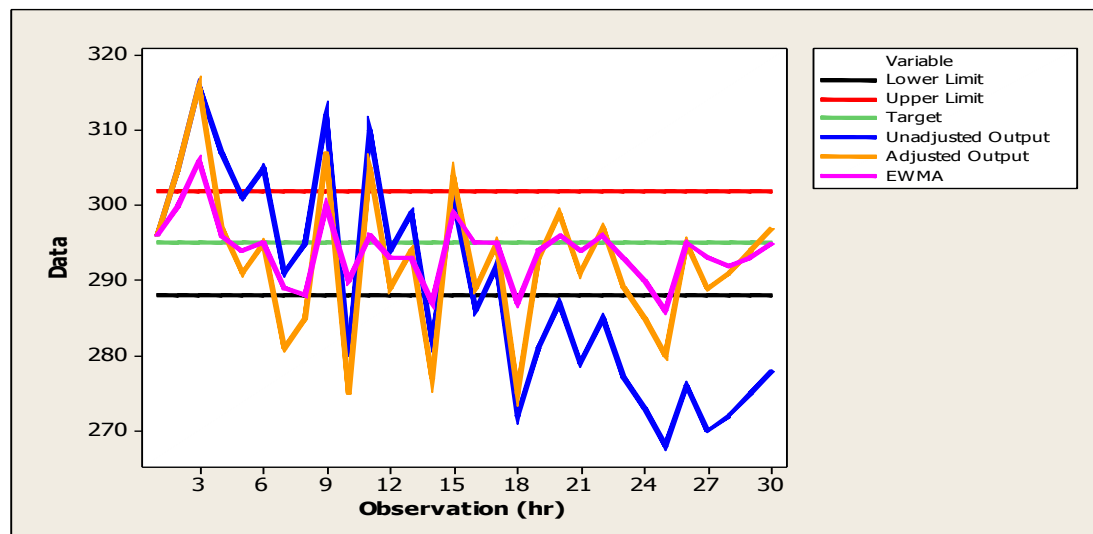

Figure 10. EWMA of Unadjusted output with λ=0.4

Figure 11: Bounded chart showing the output original unadjusted, adjusted and EWM

Table 3. Process Comparison before and after adjustments for different λ

Process	Target g/lit	Variance	Standard Deviation	No. of Adjustments	Performance Measure
Before Adjustment	288.8	194.3	13.94	-	225.8
After Adjustment, λ=0.1	289.5	175.85	13.26	2	200.2
After Adjustment, λ=0.2	290.0	130.9	11.44	4	151.6
After Adjustment, λ=0.3	290.7	98.4	9.92	5	113.9
After Adjustment, λ=0.4	292.7	91.05	9.54	5	93.4
After Adjustment, λ=0.5	293.8	90.1	9.49	4	88.5
After Adjustment, λ=0.6	295.2	122.34	11.06	7	118.3

References

[1] Alwan, L. C. and Roberts, H. V., Time series modeling for statistical process control in Statistical Process Control in Automated Manufacturing. Edited by J. B. Keats and N.F Hubele, 45-65. Marcel Dekker, New York, 1989.

[2] Astrom, K. J. and Wittenmark, B, Computer-Controlled Systems, 3rd ed., Prentice-Hall, Englewood Cliffs, NJ., 1997.

[3] Box, G. E. P., G. M. Jenkins, and G. C. Reinsel), Time Series Analysis, Forecasting, and Control, 3rd ed. Prentice-Hall, Englewood Cliffs, NJ., 1994.

[4] Box, G. E. P and T. Kramer, Statistical process monitoring and feedback adjustment: a discussion, Technometrics, Vol. 34 (1992).

[5] Box, G. E. P. and Luceno, A, Statistical Control by Monitoring and Feedback Adjustment, Wiley, New York, 1997.

[6] Capilla, C., Ferrer, A., Romero, R. and Hualda, A. Integration of statistical and engineering process control in a continuous polymerization process. Technometrics, Vol. 41(1999) 14-28.

[7] G. A. Barnard, "Control Charts and Stochastic Processes", Journal of the Royal Statistical Society, Vol. 21 (1959) No. 2.

[8] Hoerl, R. W., Snee, R. D., "Closing the gap-Statistical engineering links statistical thinking, methods, tools. Quality Progress", Website, May (2010): 52–53.

[9] Hunter, J. S., The exponentially weighted moving average. Journal of Quality Technology18 (1986) 203-210.

[10] Jiang, W. and Tsui, K.-L., An economic model for integrated APC and SPC control charts. IIE Transactions on Quality and Reliability, 32 (2000) 505-513.

[11] MacGregor, J.F., On-Line Statistical Process Control, Chemical Engineering Process, Vol. 84 (1988) No. 10.

[12] MacGregor, J. F., Discussion of Some statistical process control methods for autocorrelated data. Journal of Quality Technology23 (1991) 198-199.

[13] MacGregor, J. F, Discussion of Statistical process monitoring and feedback adjustment-A discussion. Technometrics 34 (1992) 273-275.

[14] Mohammed A. Rahim, Yasir A. Siddiqui, Moustafa Elshafei "Integration of Multivariate Statistical Process Control and Engineering Process Control "Proceedings of the 2014 International Conference on Industrial Engineering and Operations Management Bali, Indonesia, January 7 – 9, 2014

[15] Montgomery, D. C., Keats, J. B., Runger, G. C. and Messina, W. S., Integrating statistical process control and engineering process control. Journal of Quality Technology, 26 (1994) 79-87.

[16] Montgomery, D.C., Statistical Quality Control – A Modern Introduction, 7th ed., New York, NY: John Wiley & Sons Inc., 2013.

[17] Montgomery D. C. and Mastrangelo, C. M., some statistical process control methods for autocorrelated data. Journal of Quality Technology 23 (1991) 179-204.

[18] Nembhard, H.B., and Mastrangelo, C.M., Integrated Process Control for StartupOperations, Journal of Quality Technology, Vol. 30 (1998) No. 3, 201-210.

[19] Page, E. S., Continuous Inspection Schemes, Biometrics, Vol. 41 1954) No. 1, 100–115.

[20] Roberts, S. W., Control Chart Tests Based on Geometric Moving Averages, Technometrics,Vol. 42 (1959) No. 1, 97–102.

[21] Shewhart, W.A., Economic Control of Quality of Manufacturing Product, Princeton, NJ:Van Nostrand Reinhold, 1931.

[22] Sachs, E., Hu, A. and Ingolfsson, A., Run by run process control: combining SPC and feedback control. IEEE Transactions on Semiconductor Manufacturing, 8 (1995), 26-43.

[23] Tsung F. and Shi J.J., Integrated design of run to run PID controllers and SPC monitoring for process disturbance rejection, IIE Trans., 31 (1999) 517-527.

[24] Tucker, W. T., Discussion of Statistical process monitoring and feedback adjustment-A discussion. Technometrics 34 (1992) 275-277.

[25] Vander Wiel, S., Tucker, W. T., Faltin, F. W. and Doganaksoy, N., Algorithmic statistical process control: Concepts and an application. Technometrics 34(1992) 286-297.

[26] Wardell, D.G., Markowitz, H., and Plante, R.D., Run-length distributions of special-cause control charts for correlated observations, Technimetrics, 36 (1994) 3–17.

[27] Wei Jiang and John V. Farr, Integrating SPC and EPC Methods for Quality Improvement, Quality Technology & Quantitative Management Vol. 4 (2007) No. 3, pp. 345-363.

[28] Zhang, N.F., A statistical control chart for stationary process data, Technimetrics, 40(1998) 24–38.

المجلة الأردنية للهندسة الميكانيكية والصناعية

مجلة علمية عالمية محكمة

ترسل البحوث إلى العنوان التالي